CERN-THESIS-2016-068

DOUBLE PARTON INTERACTIONS
WITH A Z + 2 JETS SIGNATURE
IN PROTON-PROTON COLLISIONS AT THE LHC

Pieter Christiaan van der Deijl

MIX
Paper from
responsible sources
FSC® C128610

Double Parton Interactions with a Z+2jet Signature
in Proton-Proton Collisions at the LHC
Thesis, University of Twente, 2016.

Cover design: Matthijs Ariens, www.persoonlijkproefschrift.nl.
Printed by Ipskamp Printing, Enschede, The Netherlands.
ISBN: 978-94-028-0083-8

The author was financially supported by the University of Twente
and by the 'Nationaal instituut voor subatomaire fysica' (Nikhef).

DOUBLE PARTON INTERACTIONS WITH A Z + 2 JETS SIGNATURE IN PROTON-PROTON COLLISIONS AT THE LHC

PROEFSCHRIFT

ter verkrijging van
de graad van doctor aan de Universiteit Twente,
op gezag van de rector magnificus,
prof. dr. H. Brinksma,
volgens besluit van het College voor Promoties
in het openbaar te verdedigen
op woensdag 16 maart 2016 om 14.45 uur

door

Pieter Christiaan van der Deijl
geboren op 12 Juli 1985
te Culemborg

Samenstelling promotiecommissie

Promotor:
Prof. dr. ing. B. van Eijk

Leden:
Prof. dr. ir. H.J.M. ter Brake
Prof. dr. J. Schmitz
Dr. U. Blumenschein
Prof. dr. P.M. Kooijman
Prof. dr. P.J.G. Mulders
Prof. dr. T. Peitzmann
Dr. M. Slawinska

Dit proefschrift is goedgekeurd door de promotor prof. dr. ing. B. van Eijk.

Contents

Introduction

Introduction

Physics research has developed enormously over the last century. Whereas Isaac Newton was able to deduce the classical laws of gravity from a falling apple, today's experiments sometimes involve the collaboration of thousands of physicists. These physicists are members of many different universities from a large group of countries. The most recent project is the Large Hadron Collider (LHC) at CERN in Geneva, Switzerland. In this particle accelerator, protons collide with unprecedented energy. The collisions take place at four interaction points. At each of these four points a detector is measuring fragments of collisions. The four detectors are operated by a large number of physicists, with the smallest collaboration being LHCb ($\approx$ 700 members) and the largest CMS and ATLAS ($\approx$ 3000 members). The LHC is designed as a "discovery machine". The energy at which the protons collide is almost seven times larger than in the collisions produced by the Tevatron collider at Fermilab in Chicago. The rate at which collisions occur, the instantaneous luminosity, is also in the order of twenty to thirty times higher. These exclusive properties give an enormous potential for testing a large range of theories.

Using protons instead of electrons has the disadvantage that protons are composite particles and their collisions produce significant debris. When two protons collide inelastically, usually only two constituent partons participate in the hard interaction. The other partons in the protons give rise to less energetic interactions called Multiple Parton Interactions (MPI). They create a large number of low energy particles and this complicates the analysis of the events. Solid techniques have been developed to mitigate these effects. However, in a fraction of the collisions there will be two pairs of partons having a high energy interaction. These types of events are called Double Parton Interactions (DPI) and are a potential background to rare physics processes. After the discovery of the Higgs boson [1–3], the last unmeasured property of the Standard Model is the shape of the scalar potential. Measuring this parameter requires the selection of events in which a trilinear Higgs coupling occurs [4, 5]. The cross section for these events is extremely small. Estimating all backgrounds, including DPI, with the highest precision becomes crucial. Processes involving multiple bosons will become increasingly important at the LHC and DPI forms an important background to these processes.

In first assumption, the two partonic interactions can be modelled as being independent of each other. However, the theory of Quantum Chromodynamics (QCD) predicts several types of correlations. These correlations can give significant enhancements of DPI in specific regions of phase space. The calculations required to determine the size of these correlations cannot be evaluated computationally. Measuring the size of these correlations experimentally is therefore indispensable. Experimental research on DPI was already initiated in 1987 [6] and considerable progress has been made since then [7–10].

With the high energy and luminosity provided by the LHC, several new DPI processes are within reach for investigation. The subject of this study is the DPI process in which one of the pair of partons creates a Z boson and the other pair creates two jets. The Z boson decays into two leptons (electrons or muons), giving a distinct signal, while the cross section of producing two jets is large. DPI was never studied before in this channel, but it was measured in events with a W boson instead of a Z^0. Reconstruction of a Z boson has an advantage over the reconstruction of a W boson, since there is no neutrino that escapes direct detection.

I will give an overview of the history of particle physics and the current knowledge on the Standard Model (SM) of physics in the first chapter. Chapter 2 introduces DPI and gives a prospect on the analysis approach. In chapter 3 I will explain how proton-proton interactions can be modelled by using Monte Carlo (MC) techniques. In chapter 4, the LHC and the ATLAS detector are introduced. In chapter 5, I explain my contribution to the Trigger/Data Acquisition (TDAQ) system of the ATLAS experiment. In chapter 6, the experimental prerequisites for the analysis are evaluated. This chapter explains the reconstruction of physics objects in de detector, the event selections, the background estimation and the evaluation of systematic uncertainties. Chapter 7 gives a summary of the available Monte Carlo datasets and explains how DPI events can be vetoed from the Z+jets MC dataset to obtain a clean background estimation for this process. Chapter 8 focuses on the actual analysis, the measurement of the cross section for Z + 2 jets DPI events. Finally, a transformation is applied to the distributions that removes the detector effects and returns the distribution as it should look like in reality (the truth distribution). This transformation is called “unfolding” and the details are explained in chapter 9.

1.1 Historical Perspective

Since Galileo’s formulation of mechanics, which was extended by Newton, three centuries full of discoveries in the field of natural sciences have emerged. At the end of the nineteenth century the idea arose that it would only be a matter of time before physics would be completely understood. The description of mechanics, thermodynamics and electrodynamics appeared to be complete. At the start of the twentieth century several physicists however, presented new insights on contemporary experiments. An important starting point was an article by Planck in 1900 [11] in which he defended the idea that light can be described as small energy “packets”. Max Planck is often referred to as the founder of quantum theory. He introduced the word “energy quantum”. In 1905, Einstein published four revolutionary articles:

- A paper in which he describes the photoelectric effect [12] and suggests that light quanta have properties of wave packages.
- In another paper he analysed experimental data on Brownian motion. In his view, the experimental measurements provided definitive evidence

for the existence of atoms, something that was only a theoretical concept until then [13].

- By proposing the idea that the laws of nature are exactly the same in each reference frame, he developed the theory of special relativity. By doing so he concluded a long discussion on how and why the Maxwell equations should transform when changing reference frames [14].
- In the fourth paper he extended his ideas on special relativity and demonstrated that mass and energy are closely related through the famous formula: $E^2 = m_0^2c^4 + p^2c^2$ [15].

The four articles demonstrated that physics research was still far from being complete. Einstein proceeded on generalizing the theory of special relativity to incorporate and unify the theory with Newton's description of gravity. He completed this work in 1916 [16].

The group of physicists that worked on a quantum theory was much larger. In this group were Ernest Rutherford, Erwin Schrödinger, Werner Heisenberg, Wolfgang Pauli, Paul Dirac, Enrico Fermi and many more. They developed a theory that describes the smallest fragments of matter, referred to as elementary particles. It is not possible to explain the complete theory here, but below are a number of important concepts:

- Each particle has wave properties, its wavelength is inversely related to its momentum. This wavelength is called the De Broglie wavelength [17].
- Quantum particles behave according to statistical dynamical laws instead of being rigid, deterministic bodies; they can therefore be described by using wave mechanics.
- Particles have "spin", representing their intrinsic angular momentum. Particles can have a spin with a value that is either a half-integer or an integer multiple of $\hbar = \frac{h}{2\pi}$, the reduced planck constant. In the former case, the particle is called a fermion, while in the latter case it is called a boson. The wave functions of fermions and bosons are described by different wave equations.

Quantum theory initially lead to much controversy as the probabilistic approach of describing nature's most elementary particles was seen as a flaw of science. Einstein could not reconcile himself with the idea of a nondeterministic description of nature and continued to question the theory until the end of his life. Eventually, both the experimental evidence for the premises and the theoretical consistency of the theory became more and more convincing. Eventually, quantum theory and the theory of special relativity were combined in Quantum Field Theory (QFT). Through the use of QFT, more complex systems such as small atoms can be described.

Experimental progress enabled physicists to discover a wide variety of particles, each having different properties. The muon, a heavy brother of the electron, was discovered in 1936 by Anderson and Neddermayer [18, 19]. Pions and kaons were discovered in 1947 by a group of physicists lead by Powell [20]. While accelerator techniques improved, many universities built a particle accelerator. Through the use of these accelerators, there were many resonances discovered such as the Γ, Δ, Ξ and Σ. Murray Gell-Mann was the first to publish a model ("the eightfold way") in which he proposed "partons" as fundamental building blocks [21]. In this model he suggests that many of those resonances are formed by different combinations of groups of two or three "quarks". Quarks are still considered to be elementary particles, and now we know that there are six types. Another group of elementary particles to which the electron and muon belong are the leptons. A more comprehensive model, now including forces, was formulated by Glashow, Weinberg and Salam [22–24]: The Standard Model (SM) of particle physics.

1.2 The Standard Model

1.2.1 Particles & Interactions

The SM describes the weak and electromagnetic interactions between elementary building blocks of matter. At a later stage, also the strong interaction could be integrated. A particle is defined by its quantum numbers and its rest mass. In the following section I will explain how these building blocks can be categorized.

There is a fundamental division in nature between particles with different spin. Bosons have symmetric wave functions and their states are not restricted by the Pauli exclusion principle [25]. They are the force carriers in the SM. Fermions have antisymmetric wave functions and obey the exclusion principle. The exclusion principle states that fermions with identical quantum numbers cannot be at the same location in space-time. It is essential that fermions are restricted by this principle. The structure of atoms would be completely different otherwise.

Fermions can be divided into two categories, quarks and leptons. Only quarks carry color. A striking feature of the SM is that both quarks and leptons have exactly three generations of particle doublets. The difference between the generations is the mass of the particles. For example, the electron has a brother called the muon that has the same properties, but is two hundred times heavier. There is an even heavier charged lepton called the tau, which is ≈ 17 times more heavy than the muon. In the next section I will explain how each of the forces can be described by a continuous symmetry.

One may distinguish three elementary forces in the SM, each of which is mediated by a set of bosons. To which particle each boson couples is determined by the particle properties and is summarised in figure 1.1 and explained in more detail below:

- The electromagnetic force is carried by the photon and couples to all charged particles; this is visualised in figure 1.1 by a line between the photon and the leptons, quarks and W bosons.
- The weak nuclear force is mediated by a triplet of massive weak bosons, the W^+, W^- and the Z. They couple to all left-handed particles, particles of which their momentum vector is oppositely aligned to their spin vector. This property is referred to as “maximum parity violation”. Figure 1.1 shows that the bosons may decay to both leptons and quarks.

- The strong nuclear force is mediated by an octet of massless gluons. They couple via a property that is called color, while they carry both a color and an anti-color themselves.

In addition to the bosons listed above, the Higgs boson is not associated with a particular force, but is essential to the mathematical formulation of the model. Higgs couples to all particles with mass and is the only scalar (spin-0) particle in the model. As figure 1.1 shows, it directly couples to all other particles except photons and gluons.

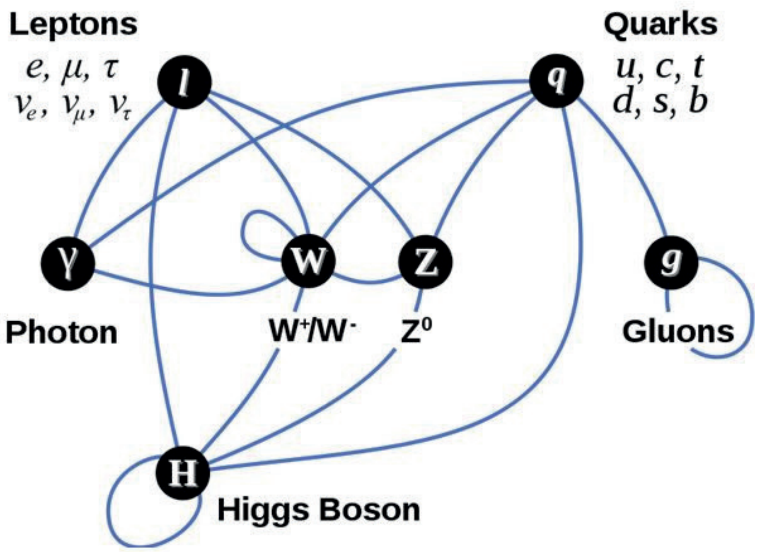

FIGURE 1.1: Standard Model particles and their interactions. Lines between the particles imply an interaction. Leptons can interact through the electromagnetic and the weak forces, while quarks also carry color and can also interact via gluons. Higgs couples to all massive particles.

1.2.2 Symmetries

Knowledge of symmetries can be used for multiple purposes in physics. A theorem that was formulated by Emmy Noether [26] predicts that for each differentiable symmetry, there is a corresponding conserved quantity. For example, if a system is invariant w.r.t. shifts in time ($t \to t + \lambda$), it conserves energy.

Symmetries are mathematically described by the concept of a group. A group is defined as a set of elements together with a group operation that works on any two of the elements of the set and results in a third element that is also a member of the set. The group may consist of a discrete number of elements, but may also describe a continuous operation. If the group operation is also differentiable, the group is called a Lie group [27].

During the development of quantum theory physicists realized that the wave function is also invariant under certain transformations. The invariance of a complex phase transition leads for example to charge conservation. At a later stage, Yang and Mills [28] sought a symmetry that described strong nuclear interactions, especially the transitions between protons and neutrons. They found that non-Abelian groups, symmetries that do not commute, can describe a symmetry between force carriers of elementary interactions. The mathematical generators of a symmetry group correspond to physical fields in these Yang-Mills theories. The hypothesis that a certain interaction is described by a symmetry group gives the theory a predictive power. For each mathematical generator of the group, there is a corresponding particle. To extract a quantitative description of the interactions in a theory, the Euler-Lagrange equation is used in a very similar way as it is used in the Lagrangian description of classical mechanics. The Lagrangian is defined as the difference between the kinetic and the potential energy of a system. According to Hamilton's principle, the Lagrangian contains all physical information of the system [29]. With the help of the Euler-Lagrange equation a kinematic description in terms of space-time coordinates can be formulated:

$$\partial_\mu \left(\frac{\partial \mathcal{L}}{\partial \left(\partial_\mu \psi \right)} \right) - \frac{\partial \mathcal{L}}{\partial \psi} = 0, \tag{1.1}$$

where ψ is a vector field. The Lagrangian for a (spin-half) Dirac field can be derived from the given definition as [30]:

$$\mathcal{L} = i\hbar c\bar{\psi}\partial\!\!\!/\ \psi - mc^2\bar{\psi}\psi. \tag{1.2}$$

One of the simplest symmetries for this Lagrangian is described by the global U(1) (the group of all complex numbers with absolute value 1) transformation: $\psi \mapsto e^{i\theta}\psi$. This is the transformation with which the electromagnetic interactions (the photon field) are described. Expanding this concept eventually leads to a global conservation of charge. Since this case describes the photon, the mass term should be set to zero. If we want this invariance to hold locally, we should consider the transformation $\psi(x) \mapsto e^{i\theta(x)}\psi(x)$. Differentiation of $e^{i\theta(x)}$ introduces a factor $\theta(x)$ that is not cancelled. To sustain the invariance of the transformation, the covariant derivative is introduced by replacing:

$$I\partial_\mu \mapsto D_\mu = I\partial_\mu - i\frac{e}{\hbar}A_\mu, \tag{1.3}$$

$$\tag{1.4}$$

along with the transformation:

$$A_\mu \mapsto A_\mu + \frac{\hbar}{e}\partial\theta(x). \tag{1.5}$$

By substituting this transformation into the Lagrangian 1.2 the interactions between the fermion fields and the vector field A_μ become apparent. From this Lagrangian one can derive the charge current and prove that charge is conserved. Another striking feature of this method is that the Maxwell equations can be rederived by taking the derivative of the field strength.

The weak interaction can be described in a similar way by starting from the SU(2) group, the group of all unitary 2-by-2 matrices with determinant 1. The generators of the group are the three Pauli matrices and the invariant quantity that is conserved under the weak interaction is called weak isospin.

A general SU(2) transformation can be written as: $\psi(x) \mapsto \psi(x)' = e^{i\frac{\vec{\tau}\cdot\vec{\theta}(x)}{2}}\psi(x)$, where $\vec{\tau}$ are the three Pauli matrices:

$$\tau_1 = \begin{pmatrix} 0 & 1 \\ 1 & 0 \end{pmatrix}, \tau_2 = \begin{pmatrix} 0 & -i \\ i & 0 \end{pmatrix}, \tau_3 = \begin{pmatrix} 1 & 0 \\ 0 & -1 \end{pmatrix}. \tag{1.6}$$

When this transformation is applied to the Lagrangian, the same problems with the local invariance are encountered as with U(1) symmetry. Again, a covariant derivative can be constructed to re-establish local invariance:

$$I\partial_\mu \mapsto D_\mu = I\partial_\mu + ig\frac{\vec{\tau}}{2}\vec{B_\mu}. \tag{1.7}$$

The largest difference with the U(1) group is that the covariant derivative and the gauge fields $\vec{B_\mu}$ are now no longer diagonal matrices. The transformation of a SU(2) gauge field is therefore somewhat more complex since the gauge field itself rotates:

$$\vec{B_\mu} \mapsto \vec{B_\mu} - \frac{1}{g}\partial_\mu\vec{\theta} - \vec{\theta} \times \vec{B_\mu} \tag{1.8}$$

It is tempting to take the three B-fields for the three weak gauge bosons, but the representation of the mass eigenstates of the gauge bosons is a rotated version of the basis above. From the Wu-experiment [31], we know that the weak charged current exhibits maximum parity violation:

$$J^{(\mathrm{CC})\mu} = \bar{\psi}_{f'}\gamma^\mu\frac{1}{2}\left(1-\gamma^5\right)\psi_f. \tag{1.9}$$

After some algebra, we can deduce from this equation that the two charged W-bosons are formed by: $W_\mu^\pm = \frac{B_\mu^1 \mp iB_\mu^2}{\sqrt{2}}$. The rotation does not introduce mass terms in the Lagrangian as they would not be gauge invariant. If the electroweak symmetry would hold, both bosons should be massless. Yet the mass of the $W^\pm$ and Z bosons are measured to be substantial: 80.4 and 90.2 GeV [32].

The introduction of a spin-0 particle (the Higgs boson) solves this problem. One of the merits of the Higgs boson is that it breaks the electroweak symmetry by mixing the B^3 and A^0 fields. This opens up the possibility of introducing invariant mass terms into the Lagrangian.

There is a striking resemblance between the Z-boson and the photon; they share the same vertices with left-handed particles. Just as the B_μ^1 and B_μ^2

fields can be combined to form the $W^{\pm}$ bosons, there are also fields that are combined to form the Z-boson and the photon. The first field is B_μ^3 and the second comes from a U(1) group with an invariant scalar that is called the hypercharge (Y). The rotation matrix for the Z/γ bosons can be written as:

$$\begin{pmatrix} \gamma \\ Z^0 \end{pmatrix} = \begin{pmatrix} \cos\theta_W & \sin\theta_W \\ -\sin\theta_W & \cos\theta_W \end{pmatrix} \begin{pmatrix} A_\mu^0 \\ B_\mu^3 \end{pmatrix} \tag{1.10}$$

The angle θ_W was predicted by Steven Weinberg [22] and measured by several experiments to have the value $\sin^2(0.2223)$ [32]. To break the symmetry, a potential should be used that has at least one local minimum. This can be achieved by adding a fourth order term to the quadratic potential:

$$V(\phi) = \mu^2\phi^\dagger\phi + \lambda\left(\phi^\dagger\phi\right)^2 \text{ with: } \left(\mu^2 < 0, \lambda > 0\right). \tag{1.11}$$

Where ϕ is an SU(2) doublet of complex scalar fields:

$$\phi = \frac{1}{\sqrt{2}} \begin{pmatrix} \phi_1 + i\phi_2 \\ \phi_3 + i\phi_4 \end{pmatrix}. \tag{1.12}$$

The global minimum of this potential is found at $\phi^\dagger\phi = -\frac{\mu^2}{2\lambda} \equiv v^2$. There are still three degrees of freedom in choosing a specific point at this minimum. These degrees of freedom lead to three additional massless scalar fields in the Lagrangian and are referred to as Goldstone bosons [33]. However, these bosons can be 'gauged away' by expanding $\phi(x)$ around a specific choice of the minimum:

$$\phi_1 = \phi_2 = \phi_4 = 0,\ \phi_3^2 = v^2. \tag{1.13}$$

The expansion of $\phi(x)$ can be written as:

$$\phi(x) = \frac{1}{\sqrt{2}} \begin{pmatrix} 0 \\ v + H(x) \end{pmatrix}. \tag{1.14}$$

It reflects the idea of a field H that fluctuates around the vacuum expectation value v. When the potential of the field is added to the electroweak Lagrangian with the generators from the pure hypercharge and isospin U(1) and SU(2) groups, the mass terms can be rearranged in such a way that the rotated mixed W- and Z-generators acquire a mass term, while the photon field remains massless. The part of the SM Lagrangian that describes the boson masses can be derived as follows, in which we omit intermediate algebraic steps:

$$\begin{aligned}
\mathcal{L}_H =& \left(D_\mu \phi\right)^\dagger \left(D^\mu \phi\right) - V(\phi) \\
=& [(\partial_\mu - ig\frac{\vec{\tau}}{2}\vec{W}_\mu - ig'\frac{Y}{2}B_\mu)\phi]^2 - \mu^2\phi^\dagger\phi - \lambda\left(\phi^\dagger\phi\right)^2 \\
=& \frac{1}{2}\partial_\mu H \frac{1}{2}\partial^\mu H \\
& -\lambda v^2 H^2 - \lambda v H^3 - \frac{\lambda}{4}H^4 \\
& +\frac{g^2 v^2}{8}\left(|W_\mu^+|^2 + |W_\mu^-|^2\right) \\
& +\frac{g^2 v^2}{8\cos^2(\theta_w)}|Z_\mu|^2 + 0 A_\mu A^\mu \\
& +\text{int. terms} + \text{kin. terms} + \text{h.c.}
\end{aligned} \tag{1.15}$$

Where g and g' are the gauge couplings for the SU(2) and SU(1) groups. They can be related to the electrical charge and the Weinberg angle: $g = \frac{e}{\cos\theta_W}$ and $g' = \frac{e}{\sin\theta_W}$. Mass terms are of the form $\frac{1}{2}M^2$. From equation 1.15, the masses of the Higgs and gauge bosons can be related to the coupling strengths of the isospin and hypercharge groups and the vacuum expectation value:

$$M_W = \frac{|gv|}{2} \tag{1.16}$$

$$M_Z = v\frac{\sqrt{g^2 + g'^2}}{2} \tag{1.17}$$

$$M_H = \sqrt{2\lambda v^2}. \tag{1.18}$$

The weak mixing angle expresses the ratio between the mass of the weak gauge bosons: $\cos(\theta_W) = \frac{M_W}{M_Z}$.

By using the Euler-Lagrange equation (eq. 1.1) a kinematical description of interactions between multiple particles can be derived. However, the resulting equations cannot be solved in an exact way. Instead, perturbation theory can be used to transform a single integral into a sum of recursive integrals [34, 35]. Each next iteration in the series will carry an additional factor equal to the electroweak coupling constant $\alpha_{EM} \approx \frac{1}{137}$. The significance of each next iteration will therefore be less than $\approx 1\%$ and for electroweak interactions it is in most cases sufficient to only calculate the first integral of the series which is referred to as the leading order (LO) approximation. Richard Feynman introduced a notation with which a schematical diagram of a specific interaction (Feynman diagram) can be used to visualise the equation to describe the interaction [36]. To calculate the scattering probability for an initial state going into a final state, all possible Feynman diagrams for this scattering need to be included. However, since usually each additional electroweak interaction will reduce the probability for that process with a factor α_{EM}, we only need to include diagrams with a minimum number of electroweak couplings (LO diagrams). In particle physics, these interaction probabilities are referred to as "cross sections".

The SM of particle physics has proven to provide an extremely good description of nature. However, there are still many open questions that cannot be answered by the SM alone. For example, we know that $\approx 5\%$ [37] of the matter and energy in the universe consists of atoms. The rest of the universe consists of dark matter [38] ($\approx 27\%$) and dark energy [39],[40],[41] ($\approx 68\%$). At the same time, theorists have pointed out the necessity for particles beyond the SM for which supersymmetry [42],[43], [44],[45] or extra dimensions [46] are possible candidates.

Many future analyses at the Large Hadron Collider (LHC) will focus on final states with multiple bosons. For example, the measurement of the scalar potential can be measured through the triple Higgs coupling. This implies processes with a Higgs decaying into two other Higgses, which again will either decay into four W/Z bosons, into four photons, etc. In these multi-boson final states, it becomes increasingly important to very precisely understand contamination by background processes. DPI events are a potential threat as they may easily generate multiboson final states that can mimic the rare multi-Higgs signal.

1.3 The Strong Nuclear Force

As a reference to the word "color", the theory describing the strong interactions is called Quantum Chromodynamics (QCD). Gluons are invariant under the transformations that belong to the SU(3) group. The generators of the group imply the existence of one singlet gluon state and eight doublet states. The singlet state ($(b\bar{b} + r\bar{r} + g\bar{g})/\sqrt{3}$) is therefore color-neutral and does not participate in interactions. Whereas each of the eight doublet states represents a gluon. Since gluons are massless they can very easily be created and annihilated.

While the value of the QED "coupling constant" α_{EM} increases slowly with increasing energy, the QCD coupling constant (α_S) depends heavily on the energy involved in the interaction. α_S is close to unity at low energies ($\Lambda \approx 300$ MeV [32]), while it becomes of order ≈ 0.1 in interactions at the scale of the Z-mass. As a consequence, perturbative QCD is not applicable at low energies ($\mathcal{O}(1$ GeV$)$). Studying DPI events is essential in understanding proton-proton collisions. For interactions at higher energies, higher order calculations are necessary to properly describe interactions correctly since each new order will approximately contribute $\mathcal{O}(10\%)$ to the total probability. Because QCD is very strong at low energies, colored quantum states are strongly suppressed. Colored particles will instantly bind to other colored states or will even create particle/anti-particle pairs to neutralise their own color. This results into a cascade of interactions until only stable color-neutral particles are left. This behaviour results in two interesting phenomena:

- Quantum confinement implies that quarks can not be observed as free particles, but are confined in hadrons.
- Since gluons are massless and carry color, they can be created with a minimal energy. However, when they get very close to each other, color charges will be screened and forces therefore reduce. As a result, partons at short distance behave as if they are almost free. While for increasing distance, the force increases as well. This effect is called asymptotic freedom.

The property of asymptotic freedom can be used to calculate cross sections for processes involving high energy proton-proton collisions.

1.3.1 Factorisation

Hadron-hadron collisions are complex interactions encompassing both perturbative and non-perturbative effects. However, the cross section for hard interactions can be calculated by exploiting the factorisation theorem. Asymptotic freedom implies that partons interacting at high energy (or short distance) can be regarded as free particles. Therefore, one can separate the calculation of the actual large momentum transfer from the calculation of the probability that two partons collide. The probability that the two protons provide the two partons with a specific energy/momentum is given by Parton Distribution Functions (PDFs). PDFs are a function of the energy scale of the scattering and the momentum fraction x of the total proton momentum that is taken by a parton. The energy scale of the scattering process is called the interaction scale and it is typically associated with the momentum transfer Q^2, or centre of mass energy $\hat{s}$.

For each quark flavour and for gluons, there is a separate PDF. The factorisation theorem states that the hard interaction cross section for two colliding protons can be calculated as a convolution of two PDFs and a perturbatively calculable partonic cross section. The theorem can be formulated as:

$$\sigma_X(p_1, p_2) = \sum_{i,j} \int dx_1 \int dx_2 f_P^i(x_1, Q^2) f_P^j(x_2, Q^2) \times \hat{\sigma}_{i,j \to X}(x_1 p_1, x_2 p_2, Q^2). \tag{1.19}$$

The $f_P^i(x, Q^2)$ represent the probabilities for finding a parton i in the proton with energy fraction x of the total proton energy (p_1, p_2 resp.), evaluated at momentum transfer Q^2. Equation 1.19 is exact at leading order (LO) and approximate at higher orders. The factorisation theorem of 1.19 breaks the complex calculation of proton-proton collisions at the LHC into three parts:

- Measuring the PDFs at low Q^2 and extrapolating to high energies with the evolution equations

- Calculating the hard scattering process through perturbation theory
- Combining the results of the two steps above by using the factorisation theorem

Since the 1960s there have been experiments that focussed on probing the structure of the proton with (deep inelastic scattering, DIS) with electrons and positrons. Examples are experiments at SLAC [47] and the ZEUS and H1 experiments at the HERA collider [48]. According to Bjorken scaling [49], the DIS scattering cross section is a function of the structure function $F_2(x)$ that only depends on x and not on Q^2. F_2 can again be related to the parton momentum distributions ($f_i(x)$) by:

$$F_2(x) = e^2 x \sum_i f_i(x). \tag{1.20}$$

By measuring the DIS cross section, the weighted sum over all parton momentum distributions can be calculated. The parton momentum distributions are the probability functions that a parton of type i (all quark flavours and gluons) carries a momentum fraction x. By exploiting our prior knowledge of the proton contents flavour dependent distribution functions can be derived from F_2. First, the total sum over all parton momentum fractions should be one:

$$\sum_i \int dx x f_i(x) = 1. \tag{1.21}$$

Next, the proton has two up valence quarks and one down valence quark. F_2 however, can also be measured in the neutron, in which there are two down and one up valence quark. In addition to the valence quarks, hadrons also carry a large number of sea quarks. Sea quarks are quark-antiquark pairs that are created by gluon annihilation. The momentum distributions of a sea quark pair should cancel, i.e. the momentum carried by sea quarks should exactly be opposite to the momentum carried by anti sea quarks. Since the three lightest quarks (up/down/strange) are much lighter than the typical momentum transfer, it can be assumed that the sea quark distributions are approximately equal:

$$u_s = \bar{u}_s = d_s = \bar{d}_s = s_s = \bar{s}_s = S(x). \tag{1.22}$$

This approach results in a number of sum rules:

$$\int_0^1 [u(x) - \bar{u}(x)]\, dx = N_u \tag{1.23}$$

$$\int_0^1 \left[d(x) - \bar{d}(x)\right] dx = N_d \tag{1.24}$$

$$\int_0^1 \left[S(x) - \bar{S}(x)\right] dx = 0, \tag{1.25}$$

where N_u and N_d are the number of up and down valence quarks in the hadron. By combining equations 1.20 and 1.23, the following equations can be derived:

$$\frac{1}{x}F_2^{ep} = \frac{1}{9}(4u_v + d_v) + \frac{4}{3}S(x)\frac{1}{x}F_2^{en} = \frac{1}{9}(u_v + 4d_v) + \frac{4}{3}S(x). \tag{1.26}$$

From these equations and the measurements of the DIS cross sections of protons and neutrons, the momentum distributions for the up and down valence quarks and for the sea quarks can be derived. The gluon PDFs can be constructed by considering the constraint that they should carry all the remaining proton momentum after subtracting the quark momentum distributions.

The statement that the scattering cross section only depends on $F_2(x)$ relies on the assumption that the photon probes a free parton inside the proton. However, higher order QCD corrections cause a violation of this scaling. For example, a gluon could be emitted just before or after the parton was struck by the photon. The Q^2 dependence of the PDFs can be calculated through the Dokshitzer-Gribov-Lipatov-Altarelli-Parisi (DGLAP) evolution equations [50–52], which can be derived from renormalisation group equations [53, 54]. These integro-differential equations evolve the quark and gluon fractions as a function of Q^2, by assuming that a parton with momentum fraction x was created by another parton with a higher momentum fraction y that splitted into two separate partons with fractions x and y-x. For quark q_i and gluon g, the equations read:

$$\frac{dq_i(x,Q^2)}{dQ^2} = \frac{\alpha_s(Q)}{2\pi}\int_x^1 \frac{dy}{y}\sum_i \left(q_i(y,Q^2)P_{qq}\left(\frac{x}{y}\right)\right) + \frac{\alpha_s(Q)}{2\pi}\int_x^1 \frac{dy}{y}\left(g(y,Q^2)P_{qg}\left(\frac{x}{y}\right)\right) \quad (1.27)$$

$$\frac{dg(x,Q^2)}{dQ^2} = \frac{\alpha_s(Q)}{2\pi}\int_x^1 \frac{dy}{y}\sum_i \left(q_i(y,Q^2)P_{gq}\left(\frac{x}{y}\right)\right) + \frac{\alpha_s(Q)}{2\pi}\int_x^1 \frac{dy}{y}\left(g(y,Q^2)P_{gg}\left(\frac{x}{y}\right)\right). \quad (1.28)$$

The probability of a parton to split into two new partons is given by the splitting functions P. The splitting functions are visualised in figure 1.2:

- A gluon either can be created through the three gluon vertex or by radiation off a quark (P_{gg} and P_{gq})
- A quark can either be created through gluon splitting into a quark-antiquark pair or via a parent quark (P_{qg} and P_{qq})

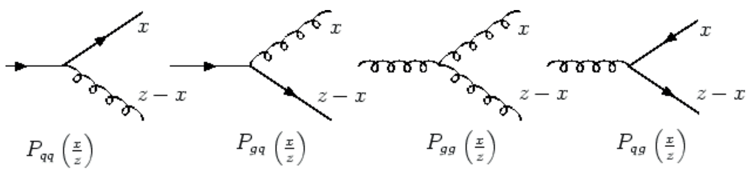

FIGURE 1.2: The four leading order processes that contribute to parton splitting. Each diagram reflects the probability that a parton with momentum x was created from an original parton with momentum z [55].

The probability of splitting is largest when at least one of the emitted partons is soft ($x \ll z$) and collinear (the angle between the split parton and its parent is small). The splitting functions are calculated at (LO), next-to-leading order (NLO) and next-to-next-to-leading order (NNLO) by using perturbation theory [52].

The (Q^2, x)-dependence of the structure functions has been studied extensively and the data are modelled very well by the DGLAP equations. Figure 1.3 shows a summary of data collected by four experiments [56–60].

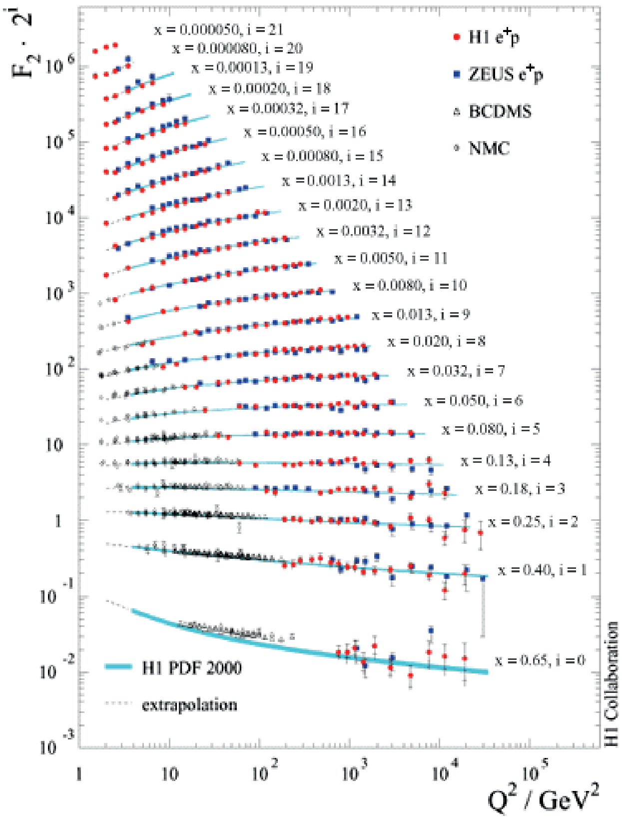

FIGURE 1.3: Collected data on measurements of the structure functions $F_2(x, Q^2)$. The figure shows that at large x, F_2 is independent of Q^2. At low x and low Q^2, a scaling violation occurs. Figure taken from [61].

Two examples of PDFs at a low momentum transfer ($Q^2 = 10$ GeV^2) and at typical LHC momentum transfer ($Q^2 = 10000$ GeV^2) are depicted in figure 1.4. The measured low Q^2 PDFs are used as an input to the DGLAP evolution equations to calculate the PDFs at higher Q^2 (figure 1.4) The high Q^2 PDFs show a few specific features such as that the parton-densities for all parton flavours shift to small momentum fractions. When the proton is probed at higher momentum transfer, partons with smaller momentum fraction become visible. Gluons become increasingly dominant at higher momentum transfer, and sea quarks carry a larger fraction of the momentum in comparison to the low Q^2-PDF.

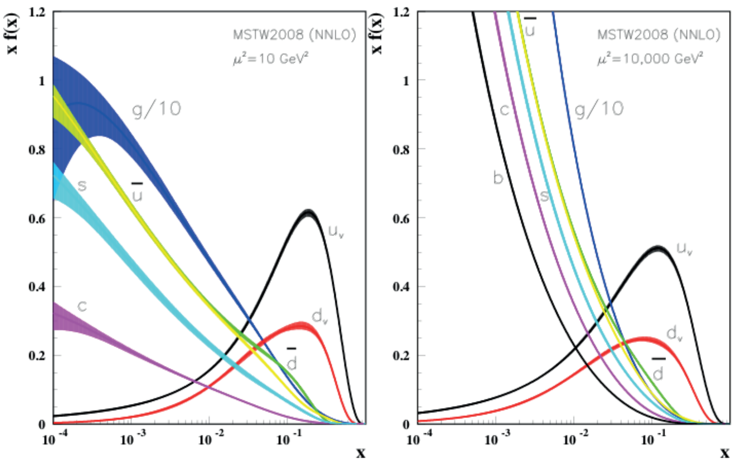

FIGURE 1.4: Parton distribution functions fitted by the MSTW group [62] to data from various experiments, for two different Q^2-values. The width of the lines indicates the total error.

1.3.2 Proton-Proton Collision Cross Section

When two protons collide, two classes of interactions may occur:

- Elastic scattering: the protons remain intact, the p_T transfer is typically small and the protons are scattered in very forward direction.
- Inelastic collisions:
  - Single diffractive (SD). One of the protons breaks up and its quarks and gluons form a jet of particles in the forward direction.
  - Double diffractive (DD). Both protons break up into two forward jets.
  - Non-diffractive (ND). In these collisions the momentum transfer is large enough for the partons from both protons to probe each other. Typically these events are characterised by high-p_T objects.

The total interaction cross section (σ_{tot}) is the sum of the four components:

$$\sigma_{tot} = \sigma_{el} + \sigma_{SD} + \sigma_{DD} + \sigma_{ND}. \tag{1.29}$$

At low p_T transfer, a proton can be described by a single wave function. Therefore the optical theorem, a non-perturbative formula: $\sigma_{tot} = \frac{4\pi}{k} Im(f_h(0))$ [63], can be used to calculate the total cross section. $Im(f_h(0))$ is the imaginary part of the hadronic scattering amplitude with a polar angle of zero and k is the wave vector. At the LHC, the Totem experiment measures charged particles in elastic and inelastic events in the very forward direction ($\theta \approx 0$). Using the Totem measurements as an input to the optical theorem gives a value for the total cross section at 8 TeV; $\sigma_{tot} = 101.7 \pm 2.9$ mb [64].

A method to derive the total non-diffractive cross section is to assume that it is dominated by the gluon $2 \rightarrow 2$ process. The gluon-gluon interaction cross section can be calculated by [65]:

$$\frac{d\hat{\sigma_{int}}}{dp_T^2} = \frac{8\pi\alpha_S^2(p_T^2)}{9p_T^4}. \tag{1.30}$$

This equation can be substituted into equation 1.19 to include the PDFs. In [65], the cross section is calculated as:

$$\sigma_{int} = \int_{p_{Tmin}^2}^{s/4} \frac{d\sigma}{dp_T'^2} dp_T'^2 \propto \frac{1}{p_T^2}. \tag{1.31}$$

The non diffractive cross section is divergent, but more importantly it exceeds the total cross section calculated with the optical theorem. The total cross section and the QCD $2 \rightarrow 2$ interaction cross section (σ_{int}) as a function of the interaction scale are shown in figure 1.5. It is tempting to assume that the discrepancy between σ_{int} and σ_{tot} at small scales is due to the breakdown of perturbation theory. However σ_{int} is already larger than σ_{tot} at $Q^2 = 2.5$ GeV^2, at which the total and interaction cross sections intersect at $\approx 100mb$. Moreover, 2.5 GeV^2 is well above the perturbative QCD scale Λ_{QCD}. Therefore perturbative breakdown cannot be main cause of the difference between the two differential cross sections. Both [66] and [65] mention two effects that could provide an explanation. The first effect is referred to as

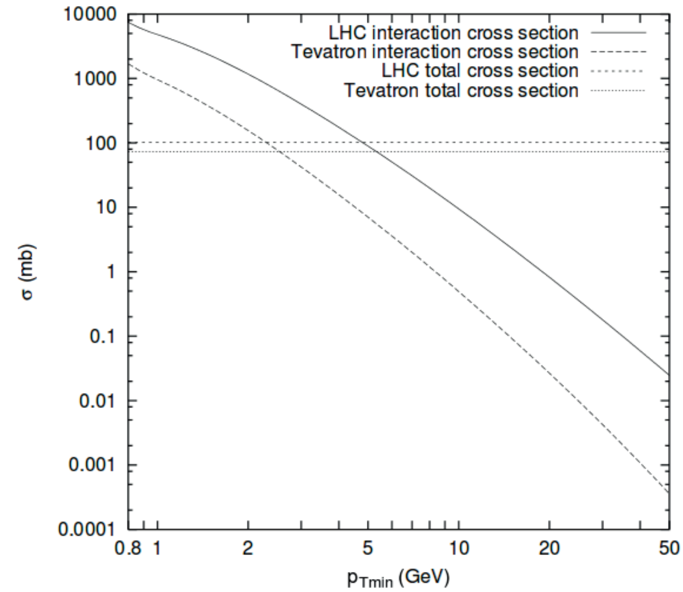

FIGURE 1.5: The total proton-proton and the QCD $2 \rightarrow 2$ interaction cross section for the LHC and Tevatron configurations. Whereas the total cross sections are approximately constant as a function of the centre-of-mass energy, the interaction cross sections rise rapidly for lower energy scales and exceed the total proton-proton cross sections.

"dense packing" [67]. At low energies ($\mathcal{O}(1GeV)$), the wave length of the probing gluons are too large to resolve the partons. The partons are screened due to asymptotic freedom. As the p_T of a parton becomes smaller, the more it gets screened by its neighbouring partons. A correction factor is applied to compensate for this effect. The factor can be derived by evaluating the cross section at a p_T increased by a small value p_{T0} at which the partons can still be regarded as free particles. This results in the following correction:

$$\frac{d\sigma}{dp_T^2} \rightarrow \frac{d\sigma}{dp_T^2} \cdot \frac{\alpha_S^2\left(p_{T_0}^2 + p_T^2\right)}{\alpha_S^2\left(p_T^2\right)} \frac{p_T^4}{\left(p_{T_0}^2 + p_T^2\right)} \alpha_S^2\left(p_T^2\right)^2. \tag{1.32}$$

p_{T_0} is a free parameter in this model and can be extracted from underlying event measurements. A typical value for p_{T_0} is 2 GeV [65]. Dense packing can partly account for the discrepancy that exists between σ_{tot} and σ_{int}. Another cause for the difference is multiple partonic interactions in a single proton-proton collision. They are counted as the same interaction in the total proton-proton cross section. However, each additional partonic interaction in the same proton-proton collision adds to σ_{tot}. To correct σ_{int} for this multiple counting effect, it should be divided by the average number of partonic interactions per proton-proton collision:

$$\frac{\sigma_{partonic}(p_{Tmin})}{\sigma_{tot}} =< n > (p_{Tmin}). \tag{1.33}$$

DPI events are a special type of MPI events in which exactly two pairs of partons form high p_T interactions. Since DPI events can form a sizeable contribution to the background of rare physics processes, it is important to understand how precise the cross section of DPI events can be estimated. In a first approach, the two interactions can be modelled as independent and the cross section of individual partonic interactions factorise. However, there are situations in which an independent modelling is insufficient and kinematical, flavour or spin correlations should be included. These correlations can potentially increase the size of the DPI cross section in specific parts of phase space. The next capter chapter explains how DPI can be modelled by assuming that the interactions are independent and an overview is provided of various models that include correlations.

Double Parton Interactions

Introduction

In the previous chapter the dynamics of proton-proton interactions were discussed. This chapter focuses on the case where two pairs of partons in a single proton-proton collision collide into two separately measurable hard interactions, DPI events. In hadron colliders, DPI processes may suffer from backgrounds where two proton-proton collisions occur at the same bunch crossing and cannot be separated. This phenomenon will be discussed in more detail in chapter 4, whereas this chapter is constrained to discussing phenomenologic aspects of DPI processes.

DPI can be divided into two different types of processes as is illustrated in figure 2.1. In pure DPI processes, two partons from the first proton and two partons from the second proton form two separate interactions (fig. 2.1 a). In "rescattering" processes, a second parton from one of the protons will recombine with either one of the incoming or outgoing particles from the primary scattering. The process visualised in the second type of diagram (2.1 b) is highly suppressed at high transverse momenta [68].

The following sections discuss how the PDFs for single parton interactions can be extended to describe the matter distribution as a function of a spatial parameter. These new PDFs can be used to set up a model to relate the cross section of DPI processes to those of SPI processes. At the low energy-scale that is typical to MPI interactions, the different partonic interactions can be modelled as being independent. There is a strong expectation that at more energetic scatterings the kinematic correlations between the interactions

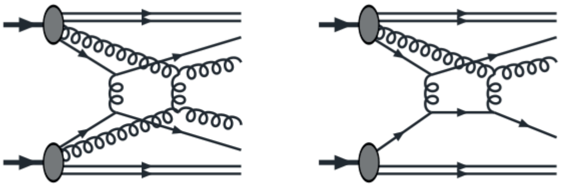

(a) (b)

FIGURE 2.1: Diagrams of a pure double parton interaction (a) and of an interaction where a second parton from the first proton rescatters with a higher order splitting of the outgoing parton from the second proton (b). [68]

will become more important. In the last section two models are introduced describing correlations between the two simultaneous interactions.

2.1 Uncorrelated Parton Interactions

A phenomenological way of formulating DPIs is generalizing Single Parton Density Functions (sPDFs) to incorporate two partons with longitudinal momentum fractions x_1 and x_2, that undergo two separate interactions with momentum transfers Q_1^2 and Q_2^2. In the most general form, an additional parameter is introduced to specify the spatial transverse distance ($\mathbf{b}$) between the partons inside the proton. These PDFs are often referred to as generalized PDFs (gPDFs), e.g. [69], or double PDFS (dPFS), e.g. [70]. In this section I will assume that the dPDFs (F) factorize into two sPDFs (f_1 and f_2) while $\mathbf{b}$ and x are assumed to be uncorrelated:

$$F(x_1, x_2, Q_1^2, Q_2^2, \mathbf{b}) \Rightarrow f(x_1, Q_1^2)G(\mathbf{b_1})f(x_2, Q_2^2)G(\mathbf{b_2}). \tag{2.1}$$

The function G($\mathbf{b}$) is referred to as the matter distribution of the proton.

Assuming that both partonic interactions are uncorrelated, the factorisation satisfies equation 1.19. The next assumption is that the probability of a DPI event is proportional to the partonic overlap of the two protons. This overlap as illustrated by figure 2.2 can be calculated by using the matter distribution functions [65]:

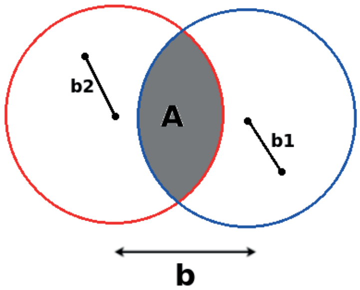

FIGURE 2.2: A schematic overview of the overlap between two colliding protons and the definition of the vectors **b**,**b1**,**b2**. When **b1** + **b2** = **b** the two partons interact.

$$A(\mathbf{b}) = \int d\mathbf{b_1}G(\mathbf{b_1})d\mathbf{b_2}G(\mathbf{b_2})\delta(\mathbf{b}-\mathbf{b_1}-\mathbf{b_2}). \tag{2.2}$$

Since the partons are assumed to be isotropically distributed in the proton, the transverse distance **b** becomes the impact paramater b. Consequently, the overlap function A(**b**) becomes A(b). A partonic interaction implies that the partons are at the same location at the time of collision $\mathbf{b} = (\mathbf{b_1} + \mathbf{b_2})$. Integrating over the product of the matter distribution functions of the the protons in the overlapping region gives the overlap. The factorisation theorem (eq. 1.19) that is used to calculate the cross section of a single parton scattering can be slightly modified, such that the cross section becomes proportional to the overlap, visualised as the shaded area in figure 2.2:

$$\sigma_X = \sum_{i,j} \int d^2b \int dx_1 \int dx_2 \int d\hat{t} f_P^i(x_1,t) f_P^j(x_2,t) A(b) \times \hat{\sigma}^k_{i,j\rightarrow X}. \tag{2.3}$$

Since we should require that the formula reduces to its original form in the case of Single Parton Interaction (SPI), the integral over the overlap function should be normalised to unity:

$$\int d^2bA(b) = 1. \tag{2.4}$$

On the basis of the assumptions above, the cross section for DPI can be calculated. The ingredients to calculate σ_{DPI} are the matrix elements for both interactions and a multiplication of the four PDFs $f_D(x, Q^2)G(b)$. The integrals should be performed over the x-space, p_T and over the spatial parameter **b**. The DPI cross section can then be expressed as a function of the separate SPI cross sections (σ_X, σ_Y).

$$\sigma_{XY} = \frac{1}{1+\delta_{X,Y}} \int d^2b \left(A\left(b\right)\sigma_{SPI}\right)^2 . \tag{2.5}$$

The factor $\frac{1}{1+\delta_{X,Y}}$ corrects for double counting in the case of identical partonic processes X and Y. The expression suggests that a DPI process can be calculated by factorising two SPI processes, and normalizing to a certain value that can be calculated by evaluating the squared overlap of the two protons. This idea is reflected by introducing the effective cross section σ_{eff}.

$$\sigma_{XY} = \frac{1}{1+\delta_{X,Y}} \frac{\sigma_X \cdot \sigma_Y}{\sigma eff}. \tag{2.6}$$

Again, the first factor ensures the correction to double counting. The normalisation factor is called the effective cross section (σ_{eff}) and from 2.5 and 2.6 it can be derived that it is related to the overlap function as:

$$\sigma_{eff} = \frac{1}{\int d^2b(A(b))^2}. \tag{2.7}$$

This formula relates the size of DPI cross sections to the matter distribution in a proton. Unfortunately, the matter distribution cannot be measured directly, but it is possbile to match several functions with measured values of σ_{eff} and other observables (e.g. [68]).

2.2 Estimating σ_{eff}

2.2.1 Theoretical Estimation

The most straightforward way of calculating σ_{eff} is assuming an explicit function for the matter distribution function G(b) and calculating σ_{eff} through equation 2.2. In [71], G(b) is modelled as a Gaussian distribution: $G(b) = \frac{1}{\pi R^2} e^{-\frac{b}{R^2}}$, where R is the proton radius. In [72], G(b) is modelled as the electromagnetic charge distribution: $G(b) = \frac{1}{R} e^{b/R}$. The results for these two implementations are summarised in table 2.1, where the explicit calculation of σ_{eff} is done for three different values of the proton radius.

	R = 0.6 fm	R = 0.7 fm	R = 0.86 fm
$G(b) = \frac{1}{\pi R^2} e^{-\frac{b}{R^2}}$	30 mb	41 mb	62 mb
$G(b) = \frac{1}{R} e^{b/R}$	21 mb	29 mb	44 mb

TABLE 2.1: Values of σ_{eff} for two different types of matter distribution functions, two hypothetical proton radii and the radius measured by elastic electron-proton scattering (0.86 fm). All calculated values for σ_{eff} are above the experimentally determined value.

Experiments point at a value for σ_{eff} between 10 and 20 mb, which is much smaller than the predicted values in table 2.1. An overview of the values that are measured by various experiments is provided in figure 2.3. Since the experimentally determined magnetic radius (r = 0.86 fm) [32] gives a σ_{eff} that is too large in comparison to the experimental measurement, also two other hypothetical radii are tested. Several groups attempted at improving MPI models in such a way that they also describe high transverse momenta scatterings correctly [73, 74], these models typically predict values for σ_{eff} in the order of 30-40 mb.

The discrepancy between the theoretical prediction and the experimental measurement of σ_{eff} points at a correlation between the two partonic interactions.

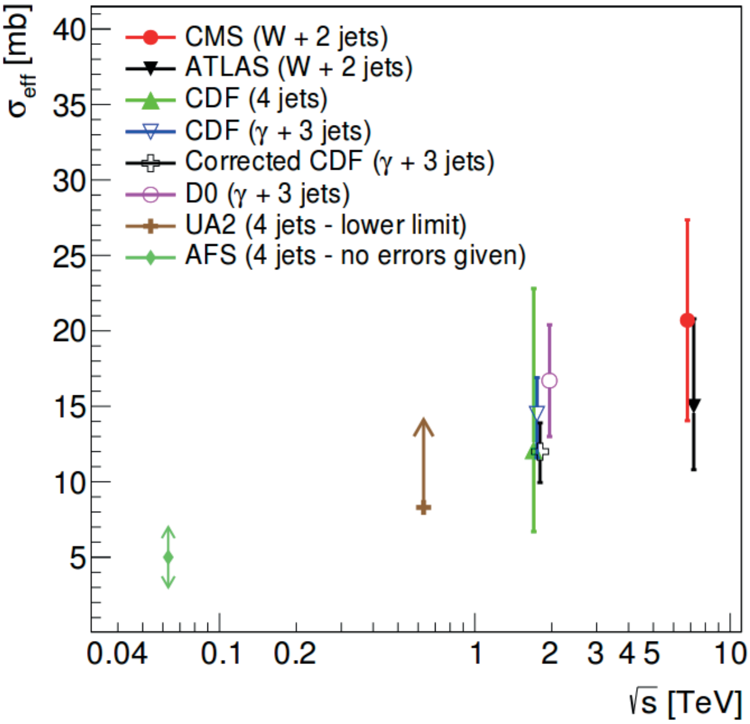

FIGURE 2.3: Summary of measurements of σ_{eff}, an arrow indicates that the error was not calculated (AFS measurement) or a limit (UA2 measurement). Measurements by the UA2,CDF, D0, CMS and ATLAS collaborations gave values between 10 and 20 mb. [6–10, 75–78]. This is significantly smaller than the theoretically predicted value, which is between 30 and 40 mb.

2.3 Correlated Interactions

There are several mechanisms through which two partons in the same proton can be correlated. This section provides an explanation of two models that describe flavour correlations and momentum correlations. There are also models that take spin correlations into account, but these correlations are negligible for DPI in Z + 2 jets events. However, there is a LHCb measurement [79] that provides evidence for spin correlations which I will discuss at the end of this section.

2.3.1 Flavour Correlations

Processes that rely on quarks instead of gluons in the initial state are suppressed by flavour correlations. For example, a W^- boson is predominantly produced by an anti-up quark and a valence down quark. The production of a second W^- is then suppressed because in one of the protons, the valence down quark is no longer available. Flavour correlations can be estimated by redefining the sum rules (eq. 1.23) for the second partonic interaction.

The authors of [73] developed a more sophisticated approach. They assume that the radius of the proton is not fixed, but depends on the distances between the valence quarks. The valence quarks are exponentially distributed as a function of the proton radius. In addition, the gluon and sea quarks should always be inside the sphere that is spun by the three valence quarks. This is achieved by rescaling the gluon and sea quark densities to an area confined by the proton radius.

Next, DPI cross sections may then be calculated by integrating over all possible configurations of valence quarks and accordingly rescaled gluon and sea quark densities. These integrals can be reduced to simple scale factors (Θ^{ij}_{kl}) depending on the number of valence quarks involved in the two hard interactions. The DPI cross section reads:

$$\sigma_{DPS}(A,B) = \frac{1}{1+\delta_{A,B}} \sum_{ijkl} \Theta^{ij}_{kl} \sigma_{ij}(A) \sigma_{kl}(B) \tag{2.8}$$

The scale factors Θ^{ij}_{kl} are then flavour dependent effective scaling factors. They can be calculated [80] and are summarised in table 2.2

Interestingly, the calculated effective cross section for the W+2jets process is much closer to the measured value of $\approx 15mb$ (fig. 2.4, [80])

2.3.1.1 Momentum Correlations

In [70] Gaunt and Stirling present a study in which they do not assume that dPDFs factorise into two sPFDs. Instead, they apply evolution equations that are an extended form of the DGLAP equations: double DGLAP equations (dDGLAP). The evolution equations were already calculated by Snigirev in

Interaction type	Scale factor $1/\Theta^{ij}_{kl}$ (mb)
(ss-ss)	12.4
(vs-ss)	31.9
(vv-ss)	28.3
(vs-vs)	69.4
(vs-sv)	69.4
(vv-sv)	68.3
(vv-vs)	67.4

TABLE 2.2: Scale factors, dependent on the parton-type, that take the role of σ_{eff} in the model of transversely correlated valence/sea-quarks.

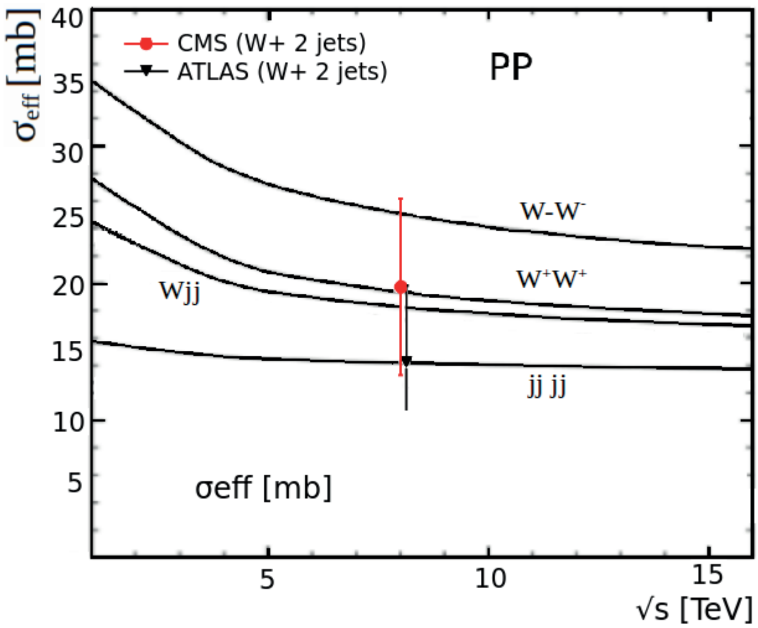

FIGURE 2.4: DPI cross sections for several processes as a function of the centre-of-mass collision energy, calculated by using the scale factors from table 2.2. The CMS and ATLAS σ_{eff} measurements of the W+2jets process are also included in the figure. [80]

[81], but Gaunt and Stirling developed a method to numerically calculate the dPDFs from the dDGLAP equations. In addition to the DGLAP equations, the dDGLAP have non-homogeneous terms that “feed” the dPDF with input from the sPDF equation [82, 83]:

$$
\begin{aligned}
\frac{dD_h^{j1,j2}(x_1,x_2,Q^2)}{dQ^2} &= \\
&\frac{\alpha_s(Q^2)}{2\pi}\Big[\sum_{j_1'}\int_{x_1}^{1-x_2}\frac{dx_1'}{x_1'}D_h^{j_1',j_2}(x_1',x_2,Q^2)P_{j_1'\to j_1}(\frac{x_1}{x_1'}) \\
&\quad+\sum_{j_2'}\int_{x_2}^{1-x_1}\frac{dx_2'}{x_2'}D_h^{j_1,j_2'}(x_1,x_2',Q^2)P_{j_2'\to j_2}(\frac{x_2}{x_2'}) \\
&\quad+\sum_{j'}D_h^{j'}(x_1+x_2);Q^2)\frac{1}{x_1+x_2}P_{j'\to j1,j2}\left(\frac{x_1}{x_1+x_2}\right)\Big].
\end{aligned}
\tag{2.9}
$$

The D_h variables are the generalized PDFs that may either indicate a sPDF or a dPDFs, the j's indicate the type of parton. Implicitly these equations account for all the separate valence, sea quark and the gluon distributions. The first two terms are the same as in equation 1.27 but the upper bounds of the integrals are modified in such a way that they don't violate momentum conservation. They reflect the two upper diagrams in figure 2.5. The two partons described by the dPDFs evolve individually by splitting a parton. As an addition to the regular DGLAP equations, the third term models the process in which a parton from an sPDF splits into *two* separate partons that are both extracted by the hard scattering, which is illustrated by the lower diagram in figure 2.5. As the third term depends on a single input parton, its evolution should be performed from a sPDF.

Notice that in these equations the energy scale Q^2 is set equal for both of the processes. This is a simplification of the full model in which the separate scatterings are allowed have different scales. The authors of e.g. [69] include a difference in the energy scales of the two processes, but they do not apply a numerical evolution of the equations.

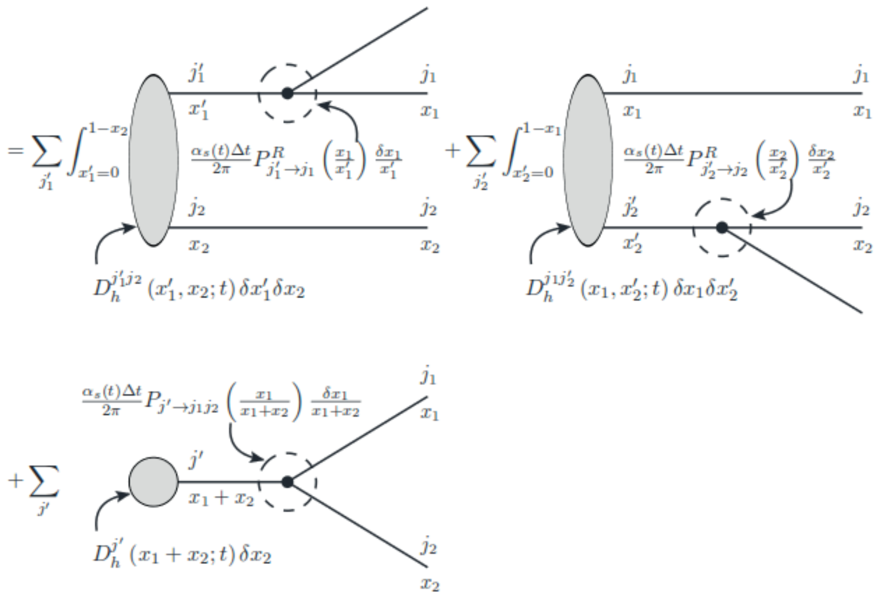

FIGURE 2.5: Diagrams that contribute to the evolution in the dDGLAP evolution equation. Each diagram indicates how an initial state with either two separate or one single parton can contribute to states with two partons having longitudinal momentum fractions x_1 and x_2

The input PDFs to the dDGLAP equations are constructed by using the assumption that at low energy scale Q^2 the sPDFs factorise. Additional boundary conditions are applied to the total momentum and to the number of quarks in these sPDFs as indicated below.

The momentum and number sum rules for dPDFs is similar to the sum rules for sPDFs(eq. 1.23), but should be slightly modified. The PDF for the first parton depends on the momentum fraction that is taken by the second parton and vice-versa. The integral over all momentum fractions x_1 between zero and $1 - x_2$, summed over all parton flavours j1, should be equal to the

PDF of x_2, rescaled by $1 - x_2$: T The momentum rule is formulated as:

$$\sum_{j1} \int_0^{1-x_2} dx_1 x_1 D_h^{j1j2}(x_1, x_2, Q^2) = (1 - x_2) D_h^{j2}(x_2, Q^2). \tag{2.10}$$

The left hand side of the equation calculates the expectation (the first moment in x_1 of the dPDF) for the PDF of the first parton, for all parton types. The right hand side of the equation gives the rescaled PDF for the second parton. If for example x_2 is very small, the equation tells that the PDF for the first parton reduces to a sPDF and the momentum rule reduces to the sPDF momentum rule (eq. 1.21).

The number sum rules refer to the fact that the sum over the full phase space should result in the correct number of quark types. By pursuing this logic, the following number sum rules can be derived. The index j_{v_1} indicates that the first parton is a valence quark:

$$\int_0^{1-x_2} dx_1 D_h^{j_{1_v} j_2}(x_1, x_2, t) = \begin{cases} N_{jv_1} D_h^{j2}(x_2, t) & \text{when } j_2 \neq j_1 \text{ or } \hat{j}_1 \\ (N_{jv_1} - 1) \, D_h^{j2}(x_2, t) & \text{when } j_2 = j_1 \\ (N_{jv_1} + 1) \, D_h^{j2}(x_2, t) & \text{when } j_2 = \hat{j}_1 \end{cases} \tag{2.11}$$

From this model one can calculate the dPDFs by numerically integrating the dDGLAP equations (eq. 2.9), imposing the boundary conditions given by the sum and momentum rules and using factorised sPDFs at low Q^2 as an input. The correlations between the two momenta of the partons can be tested by dividing the dPDFs by the factorised ansatz as a function of $x = x_1 = x_2$. The graphs in figure 2.6 provide a reflection of these ratios. Especially in the case where two up quarks are extracted from the proton, the corrections are considerable. But also for the other scenarios, the correlations are already clearly visible at the scale of $x \approx 0.1$.

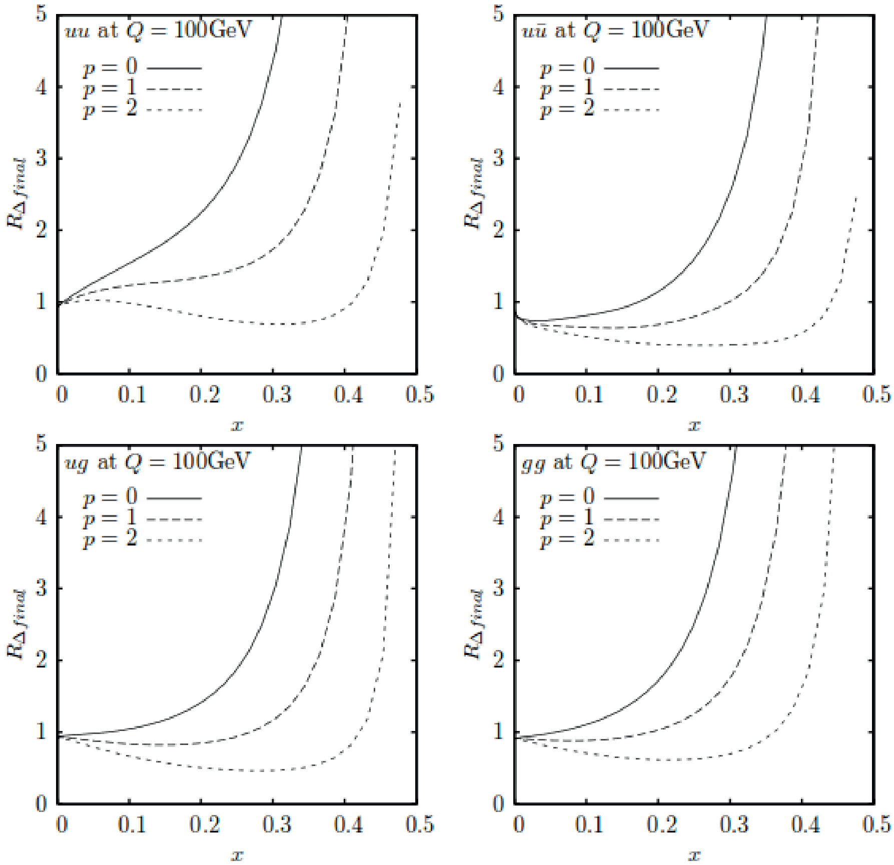

FIGURE 2.6: Ratios of the factorized sPDFs, multiplied by $(1 - x_1 - x_2)^p$ and the GS09 dPDFs for $x_1 = x_2 = x$ and four different parton-type combinations as a function of x.

2.3.1.2 Problems in the dPDF Framework

The GS09 dPDFs are the first set of dPDFs for which the numerical calculations have been implemented at large range of values for Q^2, x_1 and x_2. The calculations opened up the opportunity of phenomenological studies to DPI-processes, see for example: [84],[85]. Nonetheless, some theoretical flaws in the framework were discovered by Diehl and Schafer [86] and were also comprehensively described by Gaunt and Stirling [87]. The conclusion of this paper is that factorisation of longitudinal and transverse components of the dPDF is not correct. The necessity of including a transverse component in the definition of the dPDF arises from the interference between SPI and DPI processes in the diagrams where two partons are created from parton splitting, as described by the third term in equation 2.9. Especially in the case where in both protons the partons are the result of parton splitting, there is a large interference with SPI loop diagrams. An example of such a diagram for W-pair production is depicted in figure 2.7.

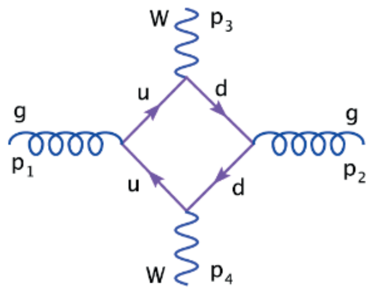

FIGURE 2.7: The diagram in which two W-bosons are created in a loop diagram. This process can both be regarded as a SPI gluon-gluon diagram and as a DPI-diagram with two pairs of quarks. It is not clear how this interference between SPI and DPI should be handled.

These diagrams have singularities of the order $1/\mathbf{b}^2$, which implies that the closer the two initial partons are in coordinate space, the larger their contribution. This seems natural, the distinction between a DPI and SPI process becomes ambiguous and one should take double-counting effects into account. The problem is that at LO the diagram has a divergence in DPI processes, but at NLO the diagram is a SM-loop diagram which should cancel the DPI-divergence. There is still an active debate on when this diagram should be calculated as a LO DPI and when as a NLO SPI process.

One suggestion is to use a cutoff scale $Q^2 = \mu^2$, above which one counts the diagram as an SPI process and below which it should be considered as a DPI process. The objection against this approach is that there is no natural choice for the value of the scale and the value would therefore be arbitrary.

Another approach was chosen in [69], in which they argue that the DPI part of the ambiguous diagram has a back-to-back enhancement of the size $\frac{Q^2}{\Lambda^2}$ which does not occur in the SPI part. With this knowledge one can define a part of phase-space in which the process is calculated as DPI and another part in which the SPI-loop calculation is applied.

A last option that is advocated in [87] is to completely omit the process in which all four partons are created by the inhomogeneous dDGLAP-term. Instead, the two scenarios in which two partons are created from the inhomogeneous dDGLAP term and two partons from the homogeneous terms should be fully incorporated into the dPDF framework.

2.3.1.3 Spin Correlations

Two additional types of correlations occur due to spin and color. The first theoretical evidence that these correlations could play an (important) role in DPI processes was already shown in [88]. In recent work [89–93] evolution equations for spin-states of partons are formulated and upper limits for angular correlations between partons are calculated. These correlations are not verified by experiments as the experimental precision is not sufficient yet. Either the systematic uncertainties are too large (processes involving jets) or the backgrounds are too high (processes with either jets or vector bosons). However, recently the LHCb collaboration published a measurement [79] of pairs of open-charm production (D^0D^0 and D^0D^+). According to phenomenological studies [94] DPI is the dominant production mechanism for these final states. Interestingly, the $\Delta\phi$ measurement between the two charm hadrons showed a sinusoidal shape as shown in figure 2.8. This shape points at a correlation between the two partonic interactions and it was argued [95] that this shape is likely to be the result of spin correlations. However, higher order calculations are required to reproduce the large $\cos 2\phi$ shape that is shown in the data.

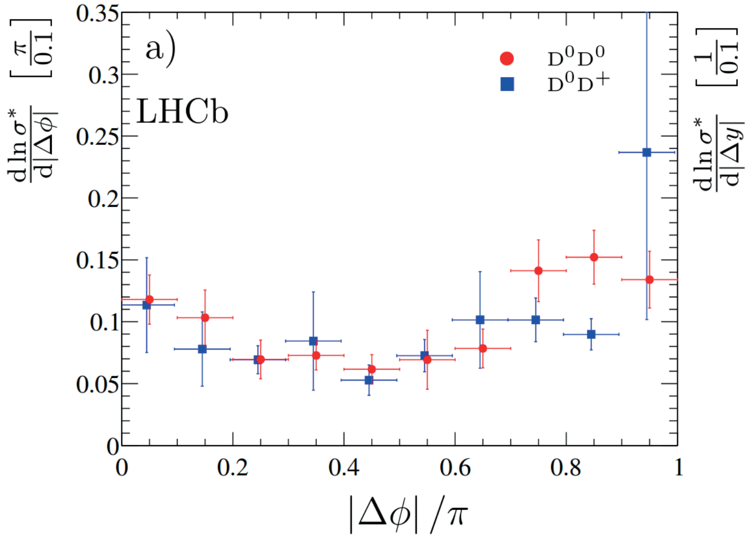

FIGURE 2.8: $\Delta\phi$ between the two charmed-hadrons $(D_0, D_0)/(D_0, D^+)$ The significance of this result is the fluctuation in the form of $\cos 2\phi$ that points at a correlation between the two separate processes in the DPI.

2.4 Conclusions

Whereas theory predicts non-negligible correlations between the two partonic interactions in DPI, it is still very difficult to verify this experimentally. The DPI measurements that are published until now, are restricted to measuring the size of the total cross section. The LHCb detector is designed to measure separate hadrons and is therefore very suitable for measuring DPI in open charm production. The estimation of the SPI background requires higher order precision calculations and therefore it is difficult to predict its contribution. The ATLAS and CMS detectors are dedicated to measuring objects with high p_T. Involving electroweak bosons in a DPI measurement has the advantage that they are relatively easy to reconstruct. The current dataset provides too little statistics to measure the DPI production of two electroweak bosons. Consequently, a logical choice is to measure one electroweak boson in association with two jets. CMS and ATLAS already published studies on W+2jet DPI production [9, 10]. The next step is to measure DPI in in a Z +

2 jets final state. Since the cross section of Z-production is approximately ten times smaller than the cross section of W-production, this process could not be measured in earlier datasets. A clear advantage of the Z + 2 jets final state over the W+2jet final state is the absence of missing energy, which carries a large systematic uncertainty.

The fraction of DPI events in the Z + 2 jets final state is expected to be of the order 3-4 %. The large background to this channel renders a measurement of correlations very difficult. Spin correlations require a precise measurement of the azimuthal angle between the Z boson and the 2-jet system. This variable ($\Delta\phi(Z, jj)$) is difficult to model in the simulation of Z + 2 jets SPI events and therefore the background estimation cannot be performed with sufficient precision. In addition, the region between $\pi/2 < |\Delta\phi(Z, jj)| < \pi$ will have a signal-to-background ratio smaller than 1 %, which further complicates the DPI measurement in that region. Correlations between the longitudinal momenta of the incoming partons are difficult to measure in the Z + 2 jets final state since the correlations are small for low values of x that are expected in Z + 2 jets events.

Consequently, I will neglect correlations between the two partonic interactions and focus on the measurement of σ_{Eff} as given in equation 2.6.

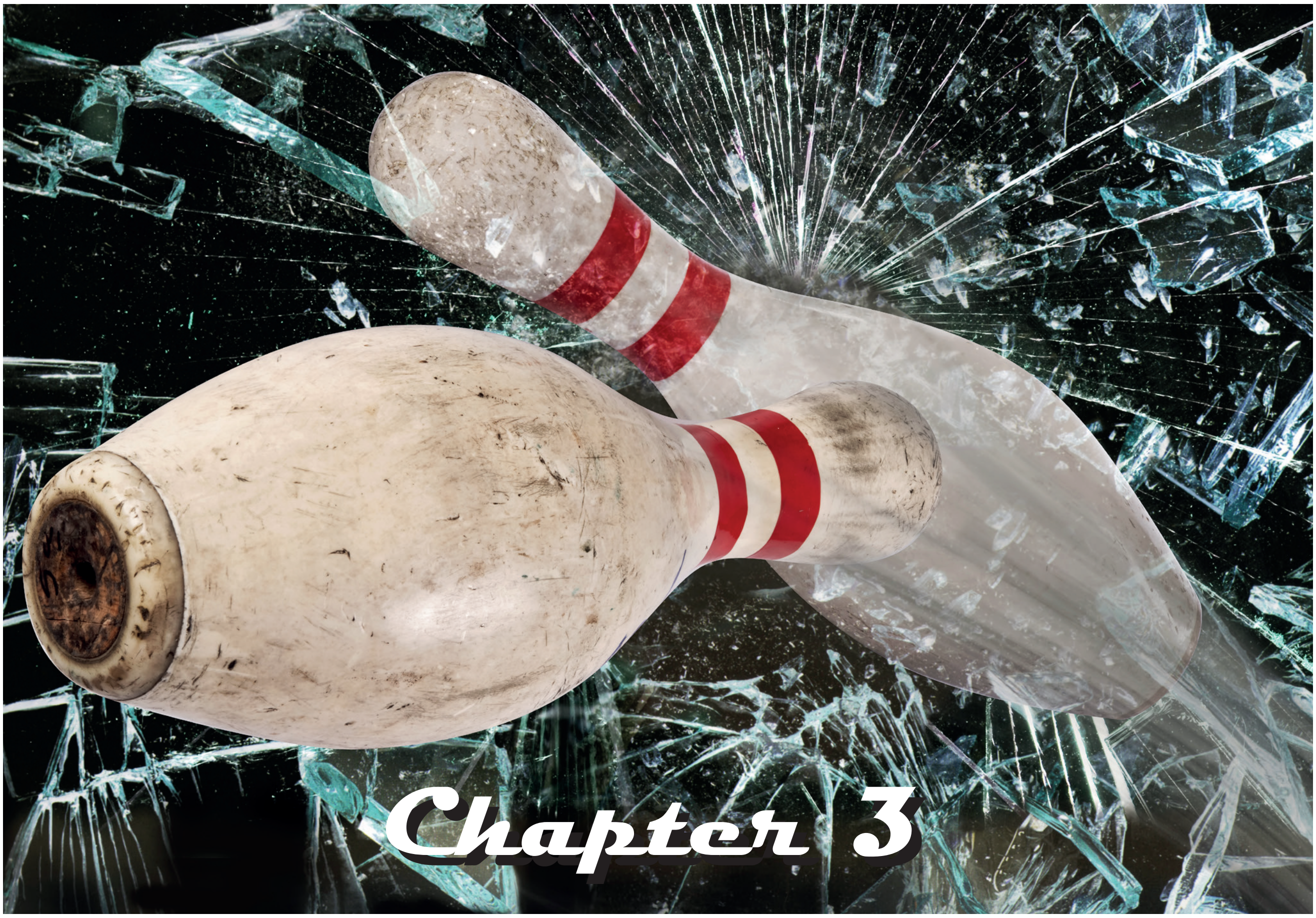

Event Modelling

Introduction

To measure the Z + 2 jets DPI signal, it is necessary to know how the backgrounds to this process look. The largest background is the SPI Z + 2 jets process, while the production of top quarks processes with two electroweak bosons in the final state form minor backgrounds. The contribution of these backgrounds are estimated by simulating proton collisions. These simulations involve a translation from the theoretical concepts explained in chapter one to a set of algorithms that can practically be implemented in computer programs. Monte Carlo techniques are the main ingredient in these algorithms and therefore the computer programs used to simulate high energy processes are called Monte Carlo (MC) generators. In the first section of this chapter I will explain how proton collisions are simulated in MC generators. In the second section, I will focus on how MPI processes are modelled in a selection of MC generators. As DPI events are modelled as an extrapolation of MPI events into the larger p_T region, this section also addresses the modelling of DPI events.

3.1 Modelling the Z + 2 jets Process in Proton Collisions

Mismodelling the SPI jets effectively results in an error on the signal (DPI) measurement. A careful modelling of the background from Z+jets from SPI is therefore equally important as the modelling of the DPI jets. In this section I will explain how the Matrix Element (ME) and Parton shower (PS) methods are used to optimize the description of the SPI jet kinematics.

Calculating Z + 2 jets events can be done by using several methods:

- To calculate all the Z+jet amplitudes at tree-level/leading order (LO) and include the additional splittings that produce additional jets at LO. These calculations do not include virtual corrections to the additional splittings and therefore they will have divergences in the infrared/collinear regions.

- Another method is approximating the splittings in the soft and collinear limits in a similar way as was done in section 1.3.1. An advantage is that an implementation of this approximation can easily be implemented using MC techniques that are called Parton Showers (PS). A parton shower also allows for multiple emissions by the same parton. A disadvantage is that it is not accurate for high transverse momenta and wide-angle splittings.

- Alternatively, higher order calculations can be included. At Next-to-Leading-Order (NLO) this implies that all diagrams, including virtual corrections, with one additional parton-splitting are precisely calculated. At Next-to-Next-to-Leading Order (NNLO), all (real and virtual) diagrams for two additional splittings are included.

While the first two methods described above are accurate in disjoint regions in phase space (wide-angle, high p_T splittings for matrix element calculations and collinear, soft p_T splittings for parton shower calculations). Matrix element and parton shower calculations should be combined to optimally describe the jet kinematics. However, if the two regions of phase space are not matched carefully, a double-counting of diagrams with at least one jet might occur. The third method provides a good description of the full phase space, but is both theoretically and computationally very challenging. In general, ME-calculations cannot calculate parton-splittings that are either collinear or very soft since the calculations diverge if not all virtual corrections are taken into account. At the same time, Parton Showers are specialized in exactly this area. To prevent double-counting a matching scheme is employed that handles the intersection between PS and ME-calculations. Depending on how many parton emissions are calculated by including virtual emissions (NLO), a different type of matching scheme should be employed. The list below summarizes the possible combinations and references to the theoretical explanations. The possible combinations are also visualised in figure 3.1.

- ME calculation including all one-loop diagrams for Z+1jet processes, while further splittings calculated by a parton shower. Two programs that exploit this technique are MC@NLO [96] and POWHEG [97]. This example is illustrated in the top-left part of figure 3.1.
- MEPS (Matrix Element+Parton Shower): Tree-level ME calculations for each process involving zero or more splittings. These diagrams can be calculated up to five additional splittings. To calculate the soft and collinear splittings, a parton shower is used. Popular matching schemes are MLM [98, 99] (Alpgen) and CKKW [100, 101] (Sherpa). This is illustrated in the bottom left part of figure 3.1.
- MENLOPS (Matrix Element at Next-to-Leading Order + Partons Shower): ME calculations are used for processes Z+1 additional parton, in which one-loop virtual corrections are included. Tree level ME calculations are used to calculate the kinematics of higher order splittings. Finally a parton shower that showers all the additional splittings is also employed [102],[103]. This matching scheme is visualised in the top right corner of figure 3.1.
- In the last type of combination, ME calculations including one-loop virtual corrections are used to calculate processes up a number of 4 partons, interfaced with a parton shower. This is visualised in the bottom right corner of figure 3.1. This scheme is for example implemented in the Sherpa 2.0 program [104].

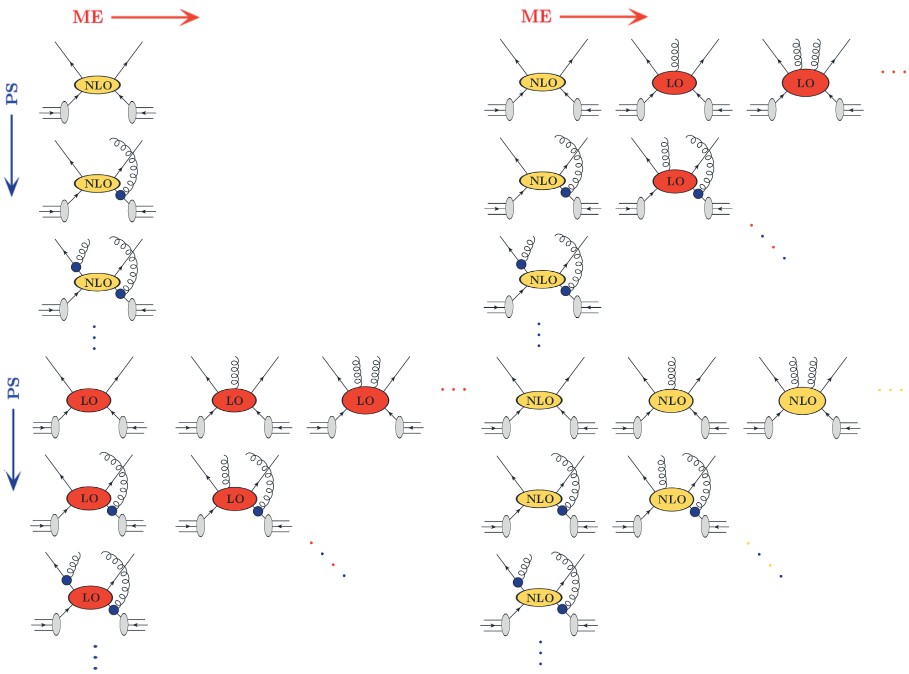

FIGURE 3.1: Four different approaches to calculate kinematics of higher order QCD emissions [96, 97]; Top left: only 1-jet events include one-loop virtual corrections; other jets are generated with a parton shower algorithm. Top right: 1-jet diagrams events include one-loop virtual correction, while the diagrams contributing to more splittings are calculated at tree-level (MENLOPS) [102, 103]. Bottom left: All diagrams are calculated at leading order and are interfaced with a parton-shower[98–101]. Bottom right: all diagrams are calculated including one-loop virtual corrections and are interfaced with a parton-shower [104]. (Figure taken from [105])

3.1.1 Matrix Element Calculations

At this moment, the most advanced ME calculations for the Z + 2 jets final state include all diagrams up to NNLO. At LO, the number of real diagrams already rises rapidly with the number of outgoing particles. For the Z + 2 jets process, there are there are already 762 different diagrams. As an example, all the eight leading order diagrams for the sub-process $gg \to Zu\hat{u} \to e^+e^-u\hat{u}$ are shown in figure 3.2.

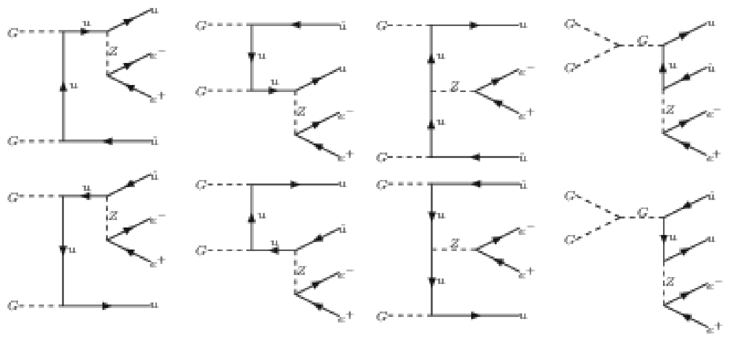

FIGURE 3.2: The eight LO diagrams that correspond to the sub-process $g, g \rightarrow e^+e^-u\hat{u}$ in the calculation of Z-production associated with two jets.

By applying recursive techniques, the relevant Feynman diagrams can be selected and calculated through automated algorithms. a few examples of implementations of these algorithms are Alpgen [106], CalcHEP [107] and MadGraph [108].

3.1.2 Parton Showers

In chapter 1, the DGLAP equations were used to model partons that split into two partons in the approximation that all splittings are either collinear or soft. The same technique is used to iteratively calculate splittings for the initial and final state quarks and gluons that are generated by the hard scattering. How Q^2 is defined in PS calculations, is somewhat arbitrary. Pythia [109] uses a p_T-ordered shower ($Q^2 \propto p_T^2$), while Herwig uses an angular-ordered shower algorithm: ($Q^2 \propto 2E_{ij}^2(1 - cos(\theta_{ij}))$). The probability that a parton splits into two parton with momentum fraction z and $(1 - z)$, can be sampled from probability distributions by using Monte Carlo techniques. Integration over the splitting functions $P_{a\rightarrow bc}(z)$, shown in figure 1.2, for all allowed values of z gives the splitting probability at certain value of $t = ln(Q^2)$:

$$\mathcal{I}(t) = \sum_{b,c} \frac{\alpha_s}{2\pi} \int_{z_-(t)}^{z_+(t)} P_{a\rightarrow bc}(z)dz. \tag{3.1}$$

The probability ($\mathcal{P}$) that there is no splitting between $(t_0, t_0 + \delta t)$ is given by $(1 - \mathcal{I}(t_0)\delta t)$. To calculate the total probability that there is no splitting between two arbitrary values for t, (t_0, t) all these infinitesimal probability densities need to be factorised. As a consequence, formula 3.1 should be exponentiated to obtain the total probability that there is no splitting between t_0 and t:

$$\mathcal{P}_{no-branching} = e^{-\int_{t_0}^{t} \mathcal{I}(t')} dt'. \tag{3.2}$$

This function is called the Sudakov form factor. As $\mathcal{P} = 1 - \mathcal{P}_{no-branching}$, the probability density function $\mathcal{P}(t)$ that can be used in Monte Carlo techniques is given by differentiating $1 - \mathcal{P}_{no-branching}$:

$$\frac{d\mathcal{P}_a}{dt} = \mathcal{I}(t)e^{\left(-\int_{t_0}^{t} \mathcal{I}(t')dt'\right)}. \tag{3.3}$$

This function gives the probability distribution of a parton “a” at energy scale t_0 that absorbs another parton, after which it will be at energy scale t. This process should be iterated for all partons up to a certain cut-off scale t_{cut} at which perturbative calculations are no longer valid.

When final state branchings no longer occur, quarks and gluons hadronise. The hadronisation is a non-perturbative QCD process and cannot be calculated by using PS techniques. The Pythia and Herwig MC generators use string [109] and cluster [72] hadronisation models respectively.

3.2 MPI in MC generators

MPI are modelled in MC programs as a part of the underlying event. In the following I will explain how I am going to extract Z + 2 jets DPI events from the UE. In particular I will explain how the fraction of DPI events (f_{DPI}) in the total Z + 2 jets sample can be extracted. I will measure f_{DPI} in the MC sample, so that we can later compare it to the value measured in the data.

In section 2.3 that the experimental determination of σ_{eff}, a measure of the size of the cross-section of DPI-processes, does not correspond to the theoretical prediction. The same holds for extrapolations of MPI-tunes into the hard-scattering regime. For theoretical explanations of this phenomenon I refer to Chapter 2, however it is important to notice that DPI processes are not described correctly by current MC-generators. In general, if a generator is tuned to fit low energetic tracks, scatterings with a higher p_T are underestimated. Still the MPI-frameworks of the generators can proof useful to construct a template for DPI events in cases where it is not possible to extract the template from the data. In the following I will first briefly explain how Pythia, Herwig and Sherpa model MPI and therefore DPI. The next section will show more on how these templates can be constructed.

3.2.1 Pythia

Pythia currently has the most advanced MPI model of all general purpose MC generators. It uses a so-called interleaved evolution [65], which means that the additional parton interactions compete with ISR for beam-momentum. Opposed to Pythia 6, version 8 also incorporates FSR in the interleaving. Interleaving is formulated by substituting $\mathcal{I}(t) = \frac{d\mathcal{P}_{MPI}}{dp'_T} + \sum \frac{d\mathcal{P}_{ISR}}{dp'_T} + \sum \frac{d\mathcal{P}_{FSR}}{dp'_T}$ into equation 3.3, where the summations run over all ISR and FSR partons.

$$\begin{aligned}\frac{d\mathcal{P}}{dp_T} = &\left(\frac{d\mathcal{P}_{MPI}}{dp_T} + \sum \frac{d\mathcal{P}_{ISR}}{dp_T} + \sum \frac{d\mathcal{P}_{FSR}}{dp_T}\right) \\ &\times e^{-\int_{p_T}^{p_T^{Max}} \left(\frac{d\mathcal{P}_{MPI}}{dp'_T} + \sum \frac{d\mathcal{P}_{ISR}}{dp'_T} + \sum \frac{d\mathcal{P}_{FSR}}{dp'_T}\right) dp'_T}.\end{aligned} \tag{3.4}$$

p_T^{Max} is the p_T of the previous step [68]. The advantage of interleaving is that the three (two for Pythia 6) different mechanisms are connected. If the ISR uses a large fraction of the proton momentum, the probabilities that the MPI and FSR mechanisms will also use a large fraction of the proton momentum will be proportionally be smaller.

Pythia also includes the rescattering process. In this process a secondary parton removed from one of the protons recoils with an outgoing particle of the hard process, as was shown in figure 2.1.

The MPI interactions are modelled mainly as QCD $2 \to 2$ processes with a certain p_T-cut-off. Even processes such as J/Ψ and W production, with relatively low cross sections, are also incorporated into the probability model.

To calculate the probability of additional secondary parton interactions, the overlap function 2.3 is used. Pythia applies a double-Gaussian matter distribution [66]. This distribution reflects the idea that a proton consists of a core with highly energetic partons, surrounded by a cloud of softer partons. The variables a_1,a_2 and β are tuned to fit underlying event data.

$$\rho(r) = (1-\beta)\,\frac{1}{a_1^3} e^{-r^2/a_1^2} + \beta \frac{1}{a_2^3} e^{-r^2/a_2^2}. \tag{3.5}$$

Multiplying two matter distribution functions and integrating over the radius as given by equation 2.2, results in a complex overlap function A(b). Pythia8 also provides the option of using a simple overlap function with a single free parameter (p):

$$A(b) \propto e^{-b^p} \tag{3.6}$$

Additionally, a tune was developed in which an Bjorken x-dependent matter overlap was proposed [68], following experimental evidence for such an ansatz in [110, 111]. Since this tune is not yet validated, it is not used for the MC samples in this thesis. It is however interesting to present the matter distribution function:

$$\rho(\mathbf{b}) \propto \frac{1}{a^3(x)} e^{-\frac{r^2}{a^2(x)}} \tag{3.7}$$
$$a(x) = a_0\,(1+a_1)\ln\frac{1}{x}.$$

a_1 and a_2 are again tuning parameters that are fitted to underlying event measurements. All of the given matter distributions try to model experimental evidence for what is called the “pedestal effect”, which means that there is more UE activity in the central region in the case of a hard scattering. The reason for this seems to be that a proton is formed of a core of particles that carry a larger fraction of the momentum and a softer cloud.

A final part in the model is the rescaling of the PDF that compensates for the extraction of a parton. Momentum conservation is modelled by evaluating the extracted parton at a higher x, dependent on the previously extracted partons:

$$x'_i = \frac{x_i}{1 - \sum_{j=1}^{j=i-1} x_j}. \tag{3.8}$$

The extraction of a valence quark rescales the valence quark PDF in such a way that the sum rules are obeyed. The sum rules also apply to sea quark PDFS. If a sea quark is extracted from the proton, a anti sea quark is left behind in the proton.

3.2.2 Herwig

In Herwig, the MPI model is based on the assumption that the total inelastic proton-proton cross section should resemble the sum of the parton-parton cross sections in each collision, (1.3.2) [72]. The result is that Herwig uses two independent Poisson distributions to sample the number of semi-hard parton MPI interactions and soft non-perturbative interactions. The matter distribution is assumed to be proportional to the Fourier transform of the electromagnetic form factor:

$$G(\mathbf{b}) = \int \frac{d^2k}{(2\pi)^2} \frac{e^{i\mathbf{k}\cdot\mathbf{b}}}{(1 + k^2/\mu^2)^2}. \tag{3.9}$$

Where μ^2 is the proton-radius. The resulting overlap function, which is the convolution of the matter distribution, is:

$$A(b;\mu) = \frac{\mu^2}{96\pi}(\mu b)^2 K_3(\mu b). \tag{3.10}$$

where K_3 is a Bessel-function of the third kind. μ is tuned for two different p_T-regions, with two separate parameters the semi-hard scatterings μ_h, and the soft scatterings μ_s. In the Z+jets samples that were used in this thesis, the two parameters were set to same value (2.386).

At the start of the event generation, the number of semi-hard scatterings n_{sh} to be produced is sampled as a Poisson distribution, with its mean proportional to the overlap of the protons. All the n_{sh} interactions are produced according to the hard QCD $2 \to 2$ cross section. The conservation of momentum is protected by verifying that the sum of the longitudinal momenta of the extracted partons does not exceed the total proton momentum. If a new interaction violates energy-momentum conservation, it is vetoed and new parton interactions will be sampled until n_{sh} is reached. The proton sum rules are protected by verifying that valence quarks can only be extracted once. When a sea quark is extracted, the number of anti sea quarks is not increased. Each of the additional interactions is showered independently.

3.2.3 Sherpa

Sherpa applies the same (simplified) model as used by Pythia. In short, the model assumes a double Gaussian matter distribution just as in equation 3.5. It diverges from Pythia as it comes to the showering, where each MPI interaction is showered independently as opposed to the interleaved evolution used by Pythia.

The ATLAS Experiment

Introduction

The ATLAS (A Toroidal LHC ApparatuS) [112] is one of the two general purpose detectors at the Large Hadron Collider (LHC), the largest and most powerful particle collider in the world. ATLAS was designed to fully exploit the potential of the proton-proton collisions delivered by the LHC, i.e. cover the range of physics in the fields of the Standard Model, Higgs boson, SUSY and searches for exotic particles and models. In addition to these topics, ATLAS also has B-physics and heavy ion programs, although it is not as specialised in these topics as respectively the LHC-B [113] and ALICE [114] experiments. The LHC collides protons with an unprecedented energy (8 TeV in 2012) and luminosity ($\mathcal{L} \approx 5{\cdot}10^{33} cm^{-2}s^{-1}$). The luminosity is a measure of the rate at which particles are collided and depends on the beam parameters. As the probability of a certain physical interaction between two protons is expressed as a cross section with unit cm^2, the number of events is calculated as: $N = \sigma \int \mathcal{L}dt$. In the formula, the luminosity is integrated over the time to calculate the integrated luminosity ($\mathcal{L}_{int} = \int \mathcal{L}dt$). The high luminosity provided by the LHC provides great opportunities in testing new theories, but also introduces experimental challenges. Each proton beam is divided in a large number of bunches. In 2012, the bunches were separated by 50 ns, which results in around 1400 bunches per beam. Due to the short separation between each bunch crossing, the electronics will not be read out before the next event occurs. This effect is called out of time pileup. Moreover, during each bunch crossing there will be many different pairs of protons interacting.

Usually only one proton-proton interaction will create an interesting physics event. However, the other proton-proton interactions will create tracks in the inner detector and deposit energy in the calorimeter. This effect is called in-time pileup and figure 4.1 (a) shows the distribution of the number of interactions per bunch crossing in 2012 data. The 2012 data had an average of approximately 20 interactions per bunch crossing, which especially causes large challenges in the reconstruction of tracks and primary vertices. This aspect will be discussed in more detail in section 6.2.1, but figure 4.1 (b) shows a glimpse of the complexity when there are 20 primary vertices reconstructed in ATLAS.

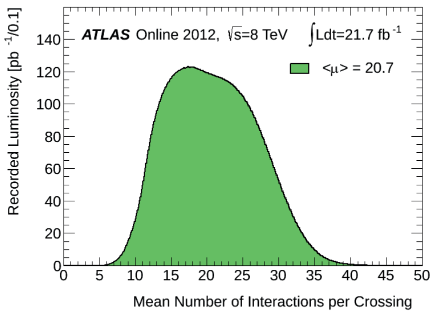

(A) Number of interactions per bunch crossing in ATLAS 2012 Data.

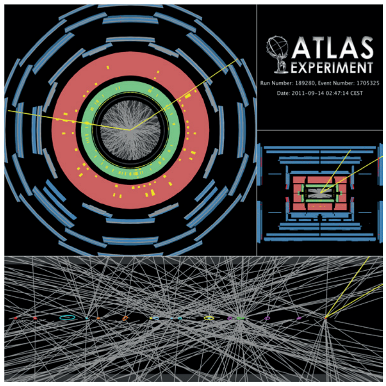

(B) ATLAS event display for an event with 20 reconstructed primary vertices.

FIGURE 4.1: The pileup distribution in the ATLAS 2012 data and a figure showing the influence of pileup on especially the track reconstruction in the inner detector.

Pileup introduces challenges in the analysis of physics events, but also in the design of the detector set up. In this chapter I will explain the design and functioning of the ATLAS detector and address the various challenges created by pileup.

4.1 ATLAS

Figure 4.2 shows a schematic view of the detector, the small picture of two people standing on top of the forward shielding structure gives an idea of the scale of the detector. The 44 meter long and 20 meter high detector is the largest one built at the LHC. Its three main parts, as regarded in order from the inside towards the outside, are the inner detector, the calorimeters and the muon spectrometer. All three consist again of smaller subdetectors. In support of accurately measuring the momentum and charge-sign of the charged particles, ATLAS uses an impressive magnetic system, consisting of a solenoid around the inner detector and three toroids that together provide the field for the muon spectrometer.

Directions and positions in the ATLAS detector are denoted in two different coordinate systems, (x,y,z) and (r,ϕ,η). The Cartesian coordinates are measured in a right-handed system. The polar coordinate-system is more commonly used when it comes to track directions in the detector. The angle ϕ is defined in the x-y plane and is zero when pointing in the direction of the positive x-axis, it runs from $-\pi$ to π. The polar angle θ runs from 0 to π from the left to the right side of the detector. A Lorentz-invariant transformation of the polar angle is called the rapidity, which is equal to the pseudorapidity in case of massless particles:

$$\eta = -\ln\left(\tan\left(\frac{\theta}{2}\right)\right). \tag{4.1}$$

The left and right side of the detector are referred to as the A- and the C-sides. Both sides of the detector consist again of two parts, the barrel and the end-cap. The barrel detectors are composed of sensors that are directed radially towards the interaction point, whereas the end-cap detectors are directed horizontally in the z-direction.

In addition to the three subdetectors, ATLAS posesses an impressive magnet system to support the momentum measurements of the inner detector and the muon spectrometer. The magnet system will not be evaluated in detail in this chapter, but is worth summarising its components. The tracks in the inner detector are bent by a surrounding solenoid magnet that produces a magnetic field of 2T. ATLAS is named after the large barrel toroid that induces the magnetic field for the muon spectrometer. This toroid consists of 8 superconducting coils, each of 25 metres long and five metres wide. The end-cap muon spectrometers are supported by two end-cap toroids and are positioned at both sides of the inner detector. Figure 4.2 shows how the three types of magnets are positioned in the detector.

In the following sections I will describe each subdetector in the same order as particles traverse through the detector.

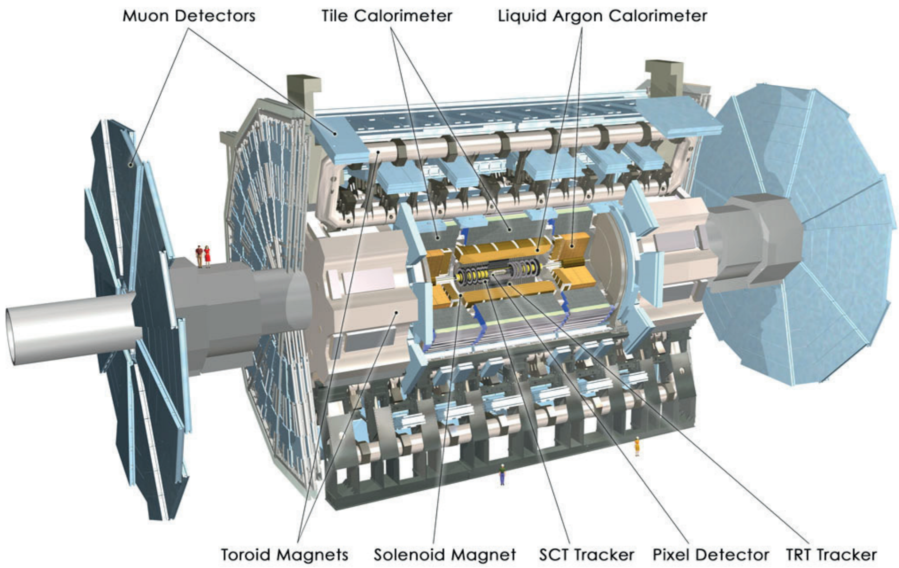

FIGURE 4.2: A schematic overview of the ATLAS detector. The size of the detector is 44m in length and 25m in height.

4.2 Inner Detector

The inner detector is the part that is built the closest around the interaction point. It is designed to measure the charge and momentum of the all charged particles with a momentum above 0.1 GeV and pseudorapidity below 2.5. A good resolution is achieved by a combination of high resolution track measurements and the stable 2T magnetic field. Apart from a good momentum resolution and charge-identification it should also determine the primary and secondary vertices. The discriminating parameters between vertices are the d_0 and z_0 displacements, respectively the transverse and longitudinal displacements of a vertex from the interaction point and are determined by extrapolating tracks back to the interaction point. The inner detector is built from three subsystems, two precision trackers (the Pixel Detector and the SemiConductor Tracker (SCT)) and the Transition Radiation Tracker that provides a large set of track hits as well as an extra separating power between electrons and charged pions. Figure 4.3 shows a schematic overview of the inner detector geometry. On average a track has three hits in the pixel detector, eight hits in four layers of the SCT and thirty-six hits in the TRT.

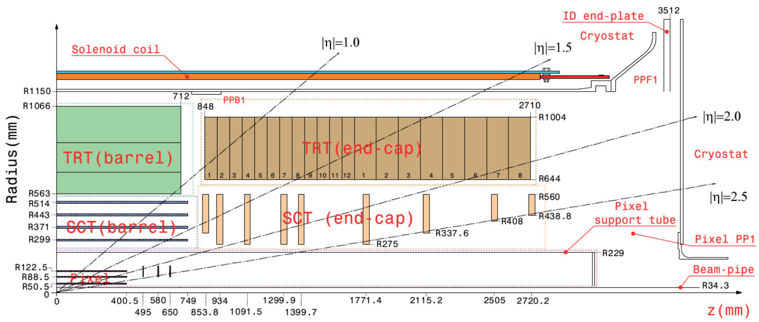

FIGURE 4.3: A schematic overview of the ATLAS detector Inner Detector. Four examples for tracks at different pseudorapidities show which detector parts should fire.

4.2.1 Pixel Detector

The first component of the precision tracker provides three track measurement in layers at 50.5, 88.5 and 122.5 mm from the interaction point in the barrel and in disks at 495, 580 and 650 mm in the end-cap. It is designed in such a way that all tracks will traverse through three layers as can be seen in figure

4.3. As its position is the closest to the beam pipe, an important requirement is that it should have a high granularity to distinguish between the charged particles and be very radiation hard at the same time. One pixel is 400 μm by 50 μm in local x-y space and has a thickness of about 250 μm. This fine granularity causes the detector to have large number of read-out channels. It has 1744 modules that each hosts 46080 pixels. A pixels is made of n+-in-n doped silicon and the sensors are fully depleted at an inverse-voltage over the p-n junction of 20V. This voltage will be increased in order to compensate for radiation damage effects that will occur.

To even further improve the hit resolution the Time over Threshold (ToT) information can be used. A charged particle almost never causes a hit in a single pixel but usually induces a signal in a larger cluster. The ToT is related to the charge induced in one pixel and a more precise measurement of the particle hit can be achieved by comparing the ratios of charge induced in each of the pixels. A hit resolution of 10 μm by 115 μma particle can be achieved by using this information. The hit efficiency and random noise ratios have been studied in depth per pixel detector layer. The seven central layers are found to have an efficiency of around 99 %, which means that 99 % of the hits can be associated to a reconstructed track. The two most outward disks in the end-caps show an efficiency that is around 1 or 2 percent lower, this is due to known issues with these two disks. Another important operational parameter is the noise occupancy of the pixels. This can be measured by using random triggers and identify which pixels have a significantly higher occupancy and are determined to be ḧot ̈. This is only a small fraction of the total pixels in the detector (300-1500 pixels out of 80 million). In further track reconstruction hot pixels are excluded by using this correction, the noise occupancy of the detector is below 10^{-9} hits per pixel per bunch crossing.

4.2.2 SemiConductor Tracker

The second layer of the precision tracker, the SCT, is required to provide at least four additional tracking points. The SCT has four layers in the barrel between 29.9 cm and 51.4 cm of radial distance to the interaction point. In the end-caps, the SCT has nine disks between 85.3 cm and 2.72 m distance in the z-direction. As the track density is already somewhat lower at these distances, the necessity of the high granularity becomes lower. The SCT uses the same silicon semiconducting technology as the pixel detector but instead of using rectangular pixels, strips of 12 cm in length are used. The width of the strips are 80 μm on average and vary between 54 and 94 μm. One sensor consists of 768 of those strips and two of these sensors are glued together back-to-back under a small stereo angle of 40 mrad to form a detector module. This stereo measurement is used to obtain a resolution of 580 μm in the non-bending plane. The size of this angle was carefully chosen in order to keep the occupancy of the strips as low as possible while obtaining a satisfying resolution. The resolution in the R-ϕ plane is comparable to that of the pixel-detector with 17 μm.

4.2.3 Transition Radiation Tracker

The third layer of the inner detector has two functions: it provides a large number (> 30) of additional tracking hits with measurements in the x-y plane and it is used in the electron identification measuring the transition radiation from traversing particles. The detector provides coverage in the region $\eta < 2$. It is filled with straw tubes of 4 mm in diameter, filled with a gas mixture ($70\% Xe + 20\% CF_4 + 10\% CO_2$) and a thin anode wire. These straw tubes are of 144 cm in length and stacked in 73 layers in the barrel section. In the end-cap the straw tubes have a length of 39 cm and are radially stacked in 160 layers. With the use of these tubes a hit resolution in the radial direction is achieved of 118 μm in the barrel section and of 132 μm in the end-caps.

In between of the straw tubes, radiator foils are placed made of Polypropylene and Polyethylene. When particles traverse through these foils they will radiate photons due to the difference in the dielectric constants of the foils which will subsequently be detected in the xenon gas. As the emitted radiation is proportional to the relativistic gamma factor of the particles: $\gamma = \frac{E}{m}$, the TRT can be used as an excellent discriminator between particles with a large mass difference. Electrons are the only particles that travel fast enough to produce significant transition radiation. Using this technique, electrons and pions can efficiently be distinguished between 1 and 150 GeV, which is reflected in figure 4.4.

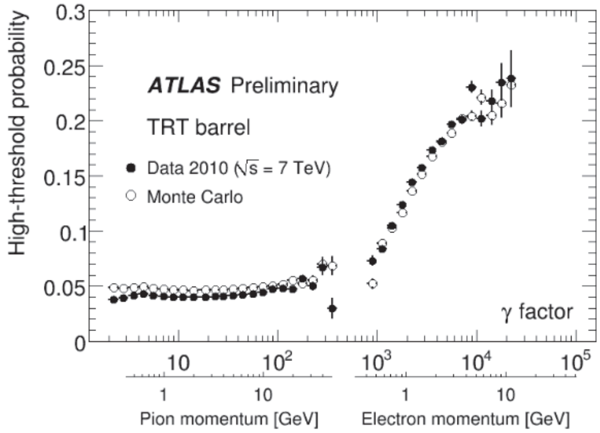

FIGURE 4.4: Probability of a TRT high-threshold hit as a function of the particleś γ-factor as measured in 7 TeV collision events.

The high number of measuring points inside the TRT comes at the price of the long tubes that do not provide information in the z-direction. This is necessary to ensure that the total number of read-out channels does not become too large. Another disadvantage of long straws is the high occupancy, which is in the order of a 1000 times higher than that of the pixel detector. The danger from a high occupancy is that multiple particles traverse through one straw and together produce the same hit. From simulation studies it was established that at a 20% detector occupancy, 10 % of all hits are expected to be due to these overlapping particles. The effect of pileup and increasing occupancy in the TRT is studied extensively and one of the aspects is the average number of robust tracks in an event as a function of the number of hits inside the detector. This function was measured for three different numbers of average proton-proton interactions in the TRT, the result is shown in figure 4.5. As this function is stable for the different data runs with different pileup, it can be concluded that the track efficiency and the fake track rate is stable.

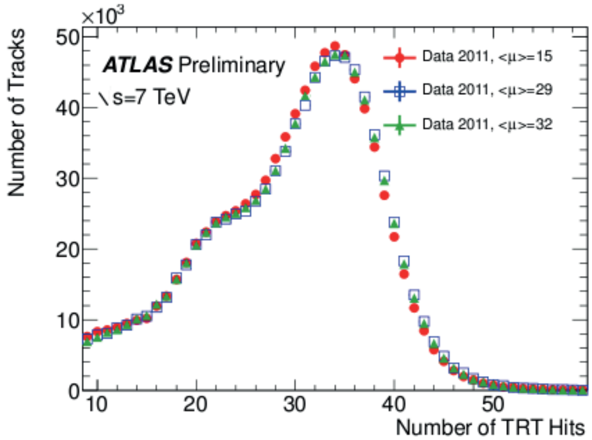

FIGURE 4.5: The average number of tracks in an event as a function of the number of hits inside the TRT.

4.3 Calorimetry

ATLAS uses sampling calorimeters that cover a large η-space ($|\eta| < 4.9$). This high hermiticity ensures that a minimum of particles escape detection and optimize the missing E_T resolution. The calorimetric system can be divided in four different parts, an overview of the lay-out is presented in figure 4.6. The EM calorimeter and the Hadronic calorimeter have a separate specialised section as well as a combined component in the most forward direction. The EM calorimeter is a LAr-lead detector, while the hadronic calorimeter uses a combination of scintillators and steel tiles. The hadronic calorimeter has an extra component in the end-cap (HEC) based on copper as the passive material and LAr as the active material. For the most forward region ($3.2 < |\eta| < 4.9$), a combined hadronic-electromagnetic calorimeter is used in order to achieve the 4π closure of the detector.

4.3.1 Electromagnetic Calorimetry

The electromagnetic calorimeter has a barrel part ($|\eta| < 1.475$) and an end-cap part ($1.35 < |\eta| < 3.2$). The section in between of the barrel and end-cap

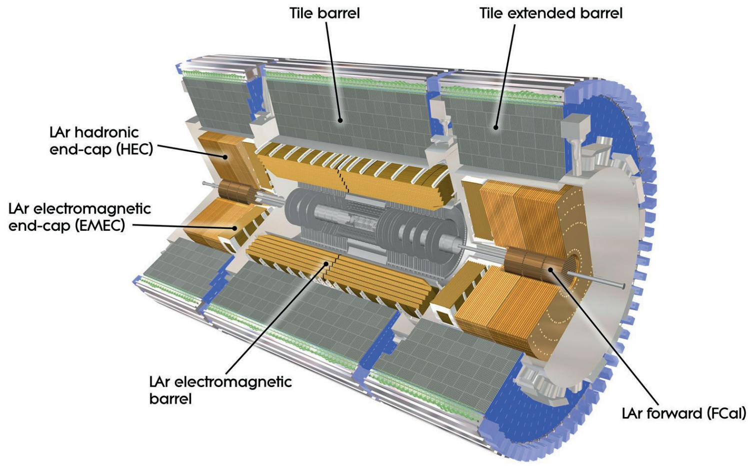

FIGURE 4.6: An overview of the calorimeter section lay-out in the ATLAS detector.

parts are called the crack regions and suffer from a degraded resolution due to the cabling and the support structures in these sections. Photons detected in these sections are never used in physics analyses, while the use of electrons from this region is avoided. The calorimeter uses lead as the passive material and cryogenically cooled liquid Argon (LAr) as the sampling material. Typical to the detector is the accordion shape that ensures full coverage and that the detector is hermetically sealed. The barrel section has more than 24 radiation lengths of material for every direction, while the end-cap even uses more than 26 radiation lengths of material. In the most central region ($|\eta| < 1.8$) a presampler is installed to correct for energy loss in inactive material in front of the calorimeter. The granularity is defined by three sampling layers. The first layer has a very fine granularity in the η-direction (0.003), but is courser in ϕ-direction (0.1). This layer is used in distinguishing between prompt photons and neutral pions that decayed to two photons. The other two layers still ensure excellent directional measurement with cells of 0.025 x 0.025 and 0.05 x 0.025. The energy resolution of electrons has been studied in detail and can be described using the standard parametrisation of a sampling term, a constant term and a noise term: $\frac{\sigma}{E} = \frac{a}{\sqrt{E}} + \frac{b}{E} + c$. The sampling term depends on the number of connections between the passive and active layer and can be extracted from Monte Carlo simulation, it was determined to be between 8 and 11 %, depending on the $\eta - \phi$-region. The constant term was measured to stay below 3 %, but in most regions around 0.7 %. The noise term is only significant in measuring the softest electrons as this term was estimated to be around 400 MeV.

4.3.2 Hadronic Calorimetry

The hadronic calorimeter consists of three main components. Up to a range of $|\eta| < 1.7$, particles are detected by the tile calorimeter. For the more forward region up to $|\eta| < 3.2$ a LAr-copper detector is used for the Hadronic End Cap (HEC). In the most forward region the LAr Forward Calorimeter (FCAL) is used as a combined electromagnetic-hadronic calorimeter between the region of $3.2 < |\eta| < 4.9$, this component will be discussed in the next section.

The tile-calorimeter is segmented in 64 wedges over the whole ϕ-region, which corresponds to a granularity of $\Delta\phi \quad 0.1$. Each wedge consists of three layers in the radial direction, the first two have a granularity in the η-region of approximately 0.1, the third layer around 0.2. Figure 4.7 shows how the passive and active materials are interconnected. At both sides of each module, wavelength shifting fibers are used to transport the signals from the scintillators to the PMTs, this double sided read-out is important to minimize the response non-uniformity.

The tile calorimeter can also be used to add measurement points to the muon trajectory. The signal-to-noise ratio was measured for connecting cells with a threshold of 250 MeV and found to be around 29. A typical muon loses between 1 and 3 GeV in the calorimeter, while a noisy tower has a maximum measured energy of a few hundred MeV.

The HEC covers precision energy measurements of hadronic particles at higher pseudorapidities ($1.5 < |\eta| < 3.2$). In each end-cap two wheels are installed that consist of 32 modules that are connected in ϕ-direction. The radially outward sections of each module are again divided in two sections, so that a granularity of 0.1 x 0.1 can be maintained up to pseudorapidities

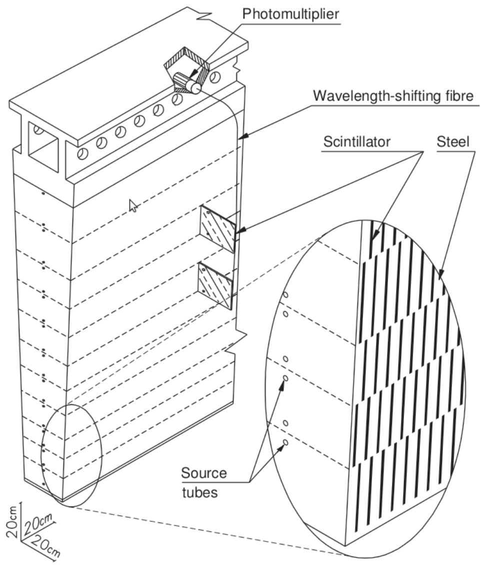

FIGURE 4.7: Schematic view of a tile calorimeter module. It is shown how the different calorimeter components are oriented, how the scintillators are read out by the optical fibers and where the PMTs are positioned.

of $|\eta| < 2.5$. Above these pseudorapidities the granularity becomes 0.2 x 0.2. Figure 4.8 shows the schematic build-up of a HEC module and of the granularity in the two HEC-wheels.

The performance of the HEC was already tested in 2002 [115]. It was established that its performance fitted the expectancy from GEANT simulation studies very closely. While the good performance of the tile calorimeter cannot be matched, the calorimeter still functions outstandingly as a forward detector. Muons can be measured with a S/B ration of 5.9 while the energy resolution of measuring jets is $\frac{\sigma}{E} = \frac{(54.2\pm)2\%}{\sqrt{E}} + (2.6 \pm 0.2)\%$.

The jet energy resolution was required to be in the order of [112] $\frac{\sigma}{E} = \frac{50\%}{\sqrt{E}} + 3\% \pm 0.1\%$. In practice, the precise jet energy resolution depends on the reconstruction algorithm and method and cannot easily be expressed in a general parameterisation of three variables. The total uncertainty was however measured [116] for various p_T- and η-bins for two different jet reconstruction algorithms (anti-k_T with R-parameters of 0.4 and 0.6). The total resolution

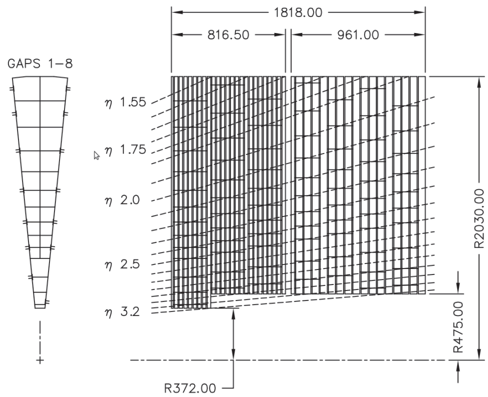

FIGURE 4.8: Schematic view of a HEC module and of the R-z view of the two wheels of the HEC. It shows how the cells are positioned inside the module and which cells are traversed through by particles at a certain pseudorapidity.

remained below 20 % for all low-p_T jets and below 10 % for jets with a higher p_T (¿ 200 GeV). These resolutions can still be improved significantly by using the transverse momenta of the tracks obtained by the inner detector, This reconstruction method is especially beneficial in the reconstruction of low p_T jets.

4.3.3 Forward Calorimeters

The most forward calorimeters ensure the full hermiticity of the detector. They consist of a electromagnetic part made of copper in the front section and two hadronic parts behind it that use tungsten as its passive material. Behind the FCAL, a shielding layer is added to the detector to protect the forward muon detectors from the high forward fluxes. A detailed overview of the different detector components is shown in figure 4.9.

The largest challenge for this part of the detector is the high particle flux that arises from the beam remnants, resulting in a high pileup of signals in the detector, but also in the build-up of ionized Argon particles. To minimize this effect, the LAr gaps were decreased by almost a factor ten in comparison to the gaps in the EMEC. These smaller gaps give a shorter peak current, but

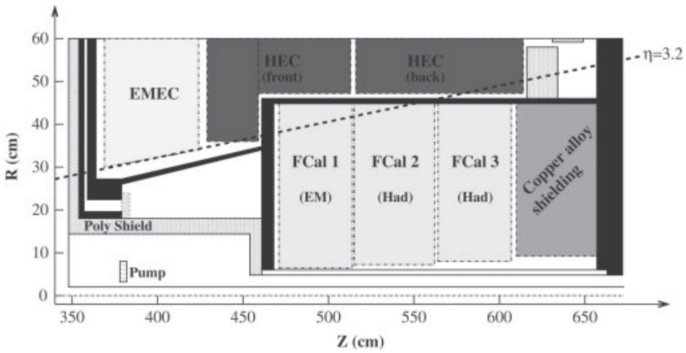

FIGURE 4.9: A schematic overview of the position of the forward calorimeters and the shielding structure.

with the same instantaneous current size. The drift time is around 60 ns in the first, electromagnetic, section of the FCAL and are somewhat larger, up to 115 ns, in the hadronic sections. The resolution of the detector is given by $\frac{\sigma}{E} = \frac{100\%}{\sqrt{E}} + 10\%$.

4.4 The Muon Spectrometer

High energetic muons are the only detectable particles that traverse through the calorimeter. By installing a specialized muon detector around the calorimeters, this property can be used to improve the momentum measurement and the determination of the charge sign. In addition, these detectors ensure that muons do not suffer much from misidentification backgrounds. Muon tracks can either be reconstructed by solely using the track points from the muon spectrometer or by a combination of points from the spectrometer and the inner detector. These muons are then respectively referred to as standalone and combined. One of the requirements that were set during the design phase of ATLAS was that the muon momentum resolution should not surpass 10% at 1 TeV. To achieve this, a combination of a high magnetic field, a good understanding of this field and a track-measurement with better precision than 60 μm are necessary.

The magnetic field is created by a large barrel toroid and two smaller end-cap toroids. The overall magnetic field is not completely uniform in η-direction, arising from the fact that three different toroid magnets are used to create the field. Different regions can be identified however. As where the barrel toroid dominates the field in the region $|\eta| < 1.4$ and the end-cap magnets dominate the regions $1.6 < |\eta| < 2.7$, the region in between is called the transition region. The field is created by a combination of two magnets in this region, but the strength cannot entirely match the other two regions. This dip in the magnetic field results in a degredation of the resolution of the muons that are reconstructed standalone by the muon spectrometer. However, figure 4.10 shows that the reconstruction efficiency of combined tracks hardly suffers from this gap in the field.

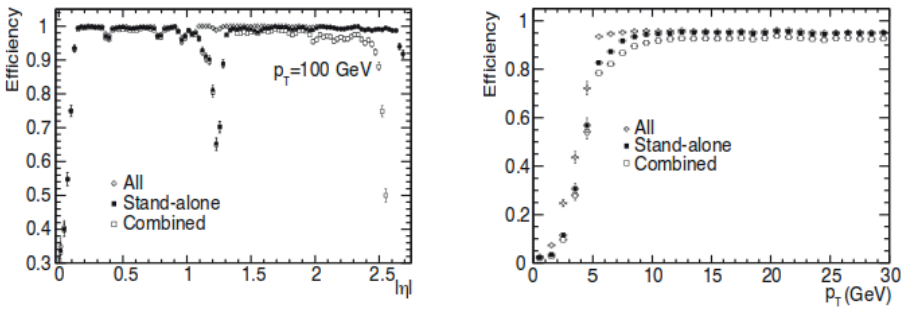

FIGURE 4.10: The efficiency for reconstructed muon tracks ($p_T = 100$ GeV, $\phi = 0$ and $\phi = \frac{\pi}{8}$) as a function of the pseudorapidity. It shows that the transition region degrades the efficiency of standalone tracks, while the efficiency of the combined tracks remains stable.

The ATLAS muon spectrometer consists of four different subdetectors, two for the precision measurements and two different triggering detectors are used. Figure 4.11 shows where the components of these detectors are installed.

The spectrometer should record at least three track points for all track directions in order to reconstruct the sagitta of the curvature. This requirement holds for both the precision chambers and the triggering chambers, figure 4.11 shows how these requirements are fulfilled. The main tracking devices are the Monitored Drift Tube chambers (MDTs). They are complemented by the

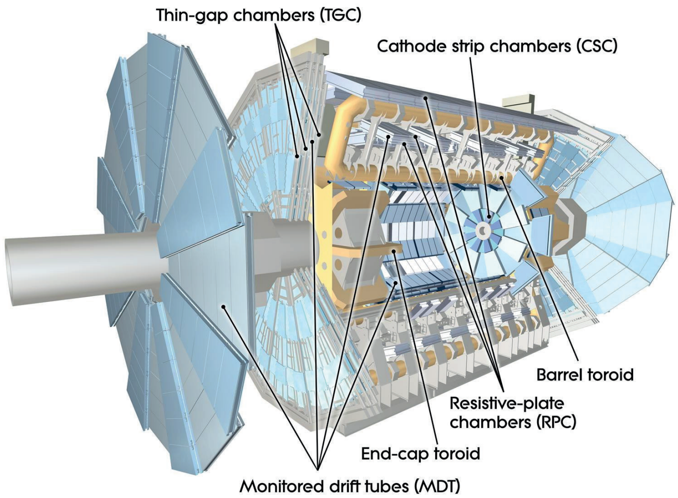

FIGURE 4.11: Positions of the different spectrometer components. Two different precision measurement techniques are used, the Monitored Drift Tubes and the Cathode Strip Chambers. The triggering is performed by separate chambers. Resistive Plate Chambers are used in the barrel, whereas Thin Gap Chambers provide finer granularity in the end-caps to avoid high occupancies.

Cathode Strip Chambers (CSCs) in the most forward region to avoid problems with high occupancies in the MDTs. In the barrel section Resistive Plate Chambers (RPCs) are used for the triggering, whereas Thin Gap Chambers (TGCs) are used for this purpose in the end-caps.

MDT chambers are composed of long tubes with a diameter of 3 cm and are filled with a gas mixture composing of Ar-CO_2 (93% - 7%). Inside the tubes a very thin anode wire is spun, while the tube itself is grounded. A charged particle that traverses through the tube will ionize the gas and the electrons and ions will respectively drift towards the walls of the tube and the central wire. In one MDT chamber there are two multilayers of tubes, which each consist of three or four layers of MDTs. In between the layers a monitoring system is installed that measures the absolute position of the chambers as well as the relative displacements with a intrinsic precision of 1 μm. The drift time of the ions in the tubes can be as large as 700 ns, which makes the chambers susceptible to high occupancies. But by measuring the drift times, a better reconstruction of the muon trajectory through the multilayers can be achieved. Combining the signals from all tubes in the chamber and by using the alignment system, the resolution in the direction of the bending plane is around 35 μm.

In the region ($2.0 < |\eta| < 2.7$), where the highest muon and background rates are expected, the use of the MDT chambers is not suitable anymore. In this region, multiwire proportional chambers, called Cathode Strip Chambers (CSCs), are installed. These chambers consist of grids of anode wires in the R-direction and cathode strips perpendicular to them. The grid structure enables the measurement of the direction in the non-bending plane and improves the granularity. This is important as the high density of particle could cause ambiguities between particles with the same η-direction. Each muon traverses through four layers of such grids. In addition to this extra measurement, the different gas mixture (Ar-CO_2, 80% - 20%) is less susceptible to neutrons and causes smaller drift times. By combining all measurements in the CSCs, the time resolution becomes 7 ns and the spatial resolution 30 μm by 115 mrad.

The drift times inside the MDTs are much larger than the time between each bunch-crossing. For this reason, MDTs cannot be used for triggering purposes and the signals cannot unambiguously be matched to a particular bunch-crossing. Another shortcoming of the MDTs is the lack of measurement in the ϕ-direction. All these deficiencies can be solved by combining the precision information from the MDTs with the excellent timing information and the ϕ-measurement that are provided by the trigger chambers. An additional requirement to the trigger chambers is that they should do an independent measurement of the p_T in order to check the momentum-threshold of the trigger.

Triggering relies on Resistive Plate Chambers (RPCs) in the barrel. These chambers use a high voltage between two plates in the saturated regime to cause an avalanche after a charged particles ionizes electrons in the gas. The read-out of these plates are aligned perpendicular in respect to each other and provide independent measurements in the η- and ϕ-directions. Two of these RPCs are attached to the middle MDT layer, one to the bottom and one on top of the chambers. The third RPC is attached to the outward side of the outer MDT layer. For muon triggers with a low-p_T threshold (6 to 9 GeV), only the two inward RPCs are used. In this case the sagitta can be reconstructed by using the primary vertex as the third measurement point. The information from the third RPC becomes necessary when the p_T threshold is larger than 9 GeV. The end-caps are equipped with Thin Gap Chambers (TGCs). These multiwire proportional chambers are made of graphite strips with thin gaps filled with anode wires that are spun perpendicular to the strips. The combination of the gas in the chambers ($CO_2 : n - C_5H_12 = 55 : 45$) and the high voltage between the strips and the wires is in saturated mode to ensure a quick avalanche. Instead of attaching the TGCs to the MDT and CSC chambers, they are positioned separately in four radial layers around the beam axis. The first chamber is mounted on the barrel toroid support structure at a distance of around 7 meters from the interaction point. The other three layers are placed at a distance of around 14 meters from the interaction point and add a total of seven measurement points to the forward muon triggering system.

Dominant effects that determine the combined resolution of the muon measurement can be divided in three different regions:

- $p_T < 30$ GeV. The energy loss in the calorimeter is the largest uncertainty.
- $30GeV < p_T < 200$ GeV. Multiple scattering effects cause the muon to change its trajectory slightly and produces the largest uncertainty in this region.
- Above 200 GeV the curvature of the muon trajectory becomes so small that the sagitta measurement is the limiting factor in the precision measurement.

The effects of these three regions are also reflected in the relation between the resolution and the p_T of the muon, which is shown in figure 4.12. The resolution drops steeply in the low-p_T region as the energy loss in the calorimeter becomes less significant. Between 30 and 200 GeV the resolution does not improve due to multiple scattering effects and remains constant. Above 200 GeV the resolution start to degrade again, this is where the muons are less curved and the sagitta can be determined less precisely. The figure also shows that the extra inner detector information improves the resolution significantly, especially in the low-p_T regime.

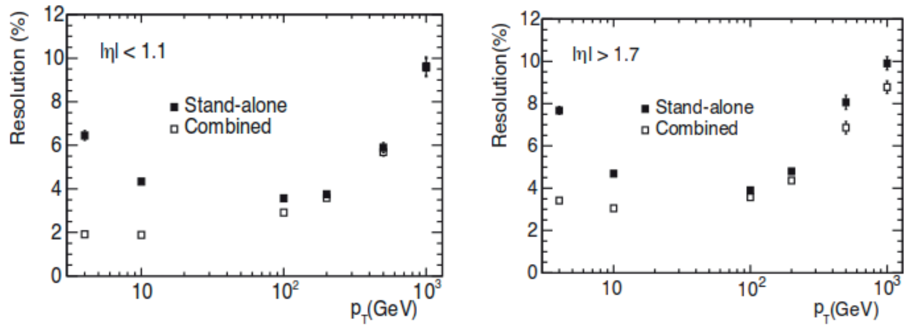

FIGURE 4.12: Resolution for combined and standalone muons in the barrel (left) and in the end-cap (right). The figure illustrates the limiting effects for the muon momentum measurement.

4.5 Conclusion

The ATLAS detector has been collecting data for five years. This period includes service and upgrade breaks. In 2011 and 2012, ATLAS recorded approximately 93 % of the luminosity that was delivered by the LHC as is shown in figure 4.13. Over its full data-taking period ATLAS published more than 400 papers (452 at the time of writing). The Higgs discovery was most certainly the pinnacle until now, but there are many more years ahead in which the LHC will deliver collisions with a higher energy and a higher luminosity.

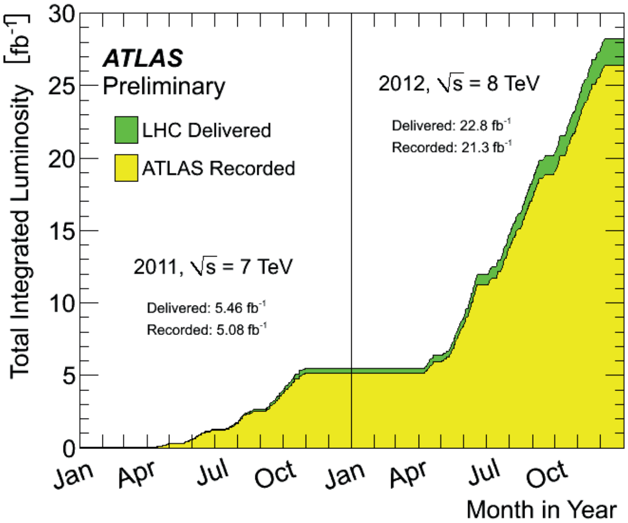

FIGURE 4.13: Integrated luminosity as delivered by the LHC and recorded by the ATLAS detector in 2011 and 2012 [117].

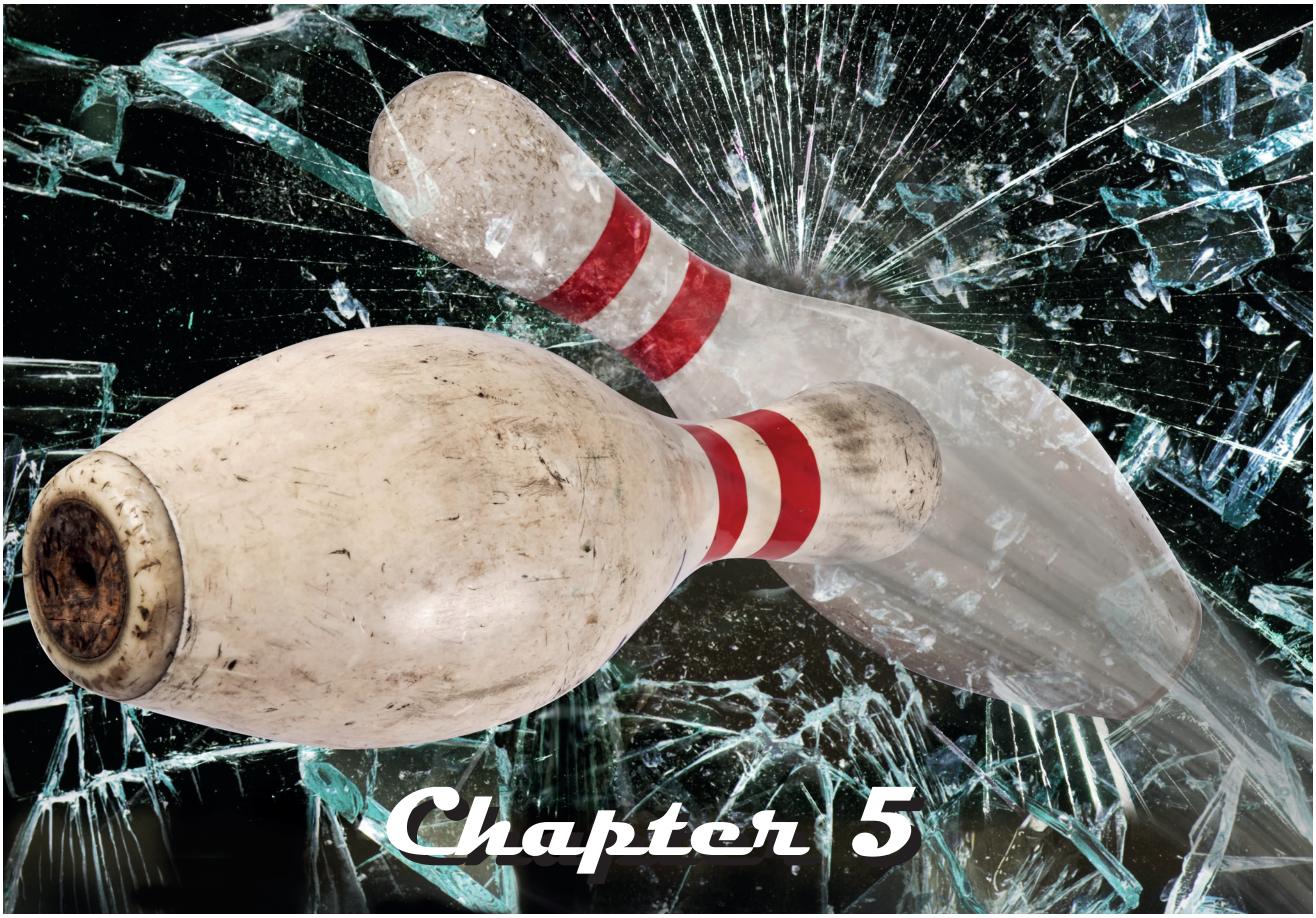

The TDAQ System

Introduction

With bunch crossings at 40 MHz and approximately 1.6 MB of data per recording, a fast functioning triggering/data acquisition system (TDAQ) is required. The ATLAS trigger system has one hardware-based level (level 1) and two software levels (level 2, event filter). The latter two together form the High Level Trigger (HLT). The trigger can be configured by using dedicated trigger items that represent physical objects such as muons or electrons with a certain threshold momentum. For each level a trigger menu can be set up that consists of a list of such items. Each item can be prescaled, which refers to a certain additional rejection factor to reduce the trigger rate of an individual item. A prescale of 10 means that only once in ten times that the item fires, it will be accepted.

The level 1 trigger (L1) only uses calorimeter and muon trigger chamber information to identify thresholds. The tasks of L1 is to reduce the event rate to a maximum of 75 kHz and identify Regions of Interest (RoI), geometrical regions in the detector defined by their angular directions. Upon an L1 accept, these RoI are passed to the level 2 (L2) trigger that uses RoI information as a seed of its calculations. After a decision is made by the L2, a signal is sent to the Read Out Drivers (RODs) attached to the detector electronics that send the detector signals to the Read Out Buffers (ROBs). In the case of a rejection at L1, the signal is issued that enables the deletion of the event in the RODs. Figure 5.1 shows a scheme of the L1 trigger. Each ROB has a memory of 64 MB and three ROBs are placed on one ROBIN, each is attached to a ROD by a Read Out Link (ROL). These ROBINs are PCI-cards that are attached to a high-end commercial server that is called the Read Out System (ROS) or ROS-PC. The function of these ROS-PCs is to answer data requests from the L2 Processing Units (L2PU) and the Event Builder (EB), delete retrieved data on the ROBINs and control the configuration of the ROBINs. In total, there are 151 ROS-PCs attached to 1583 RODs.

In case of an acceptance by the L1, RoI information is sent to the L2 Supervisor (L2SV). This application assigns the processing of the event to an L2PU on which the HLT algorithms are run. This L2PU then requests the necessary data from the ROS-PCs, based on the RoI information available. If necessary, the L2PU can also request additional information from outside the defined RoIs. The data is only retrieved from the ROS-PCs upon request of the algorithms to minimize the required bandwidth and computing power. The L2 output event rate should be reduced to a few kHz. Once an event is accepted by the L2, it is completely retrieved from the detector, built at the Event Builder and sent to the Event Filter (EF). Since this third level trigger has access to the full event and can use more processing time, it can run more sophisticated reconstruction algorithms to reduce the rate to a few hundred Hz. Figure 5.2 shows a schematic overview of the event flow in the trigger system.

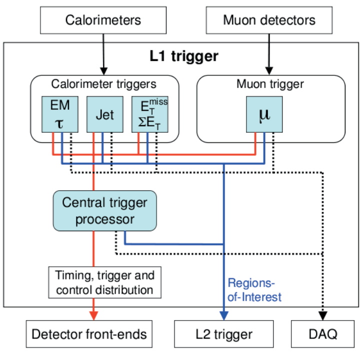

FIGURE 5.1: L1 overview

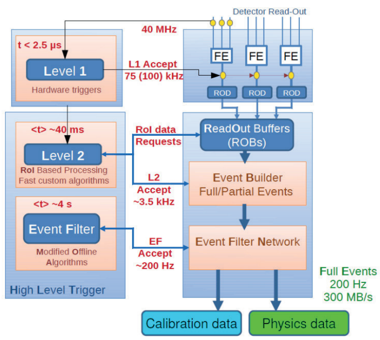

FIGURE 5.2: Overview of the ATLAS triggering system.

It is important to make efficient use of the available resources to cover the widest possible range of physics analysis with the luminosity at hand. To achieve this, it is necessary to know what the restrictions of the system are. By design, the following bottle-necks were identified:

- The maximum L1 output rate is restricted by the readout electronics to 75 kHz and will possibly be upgraded to 100 kHz,
- The CPU power and network bandwidth of the ROS-PCs restricts the maximum number of requests given to a single ROS-PC,
- The computing power of the L2 and EF processing units (L2PU and EFPU) restrict L2 and EF work load,
- Long-term restrictions to the storage and analysis capacity.

If any of the first three limits is exceeded there will be a certain "dead time" and a resulting a loss of luminosity. The dead time is defined as the time in which events cannot be recorded, even if the triggers are fired. For example, if the L1 rate exceeds the 100 kHz, the buffers of the readout electronics will get filled up and new events will be prevented from recording. Similar situations occur if the available resources in either the ROS-PCs, the L2 or the EF systems get overloaded.

An example of what happened in an actual situation is shown in figure 5.3. The figure shows the L1_EM2 rates of a ATLAS run at the 25th of May in 2010. At that time the luminosity of the LHC was still as low that the there was no HLT rejection required. The output of the L1 trigger was low enough to be passed to the event builder directly. However, at a certain point the L1 output became too high to be handled by the event building and storage facilities. The red line in figure 5.3 shows the rate at which the L1 trigger fires. The green line shows the rate after the veto that was applied to match the maximum L2 input rate. The difference between the red and the green line gives the loss of luminosity. At 4:05 the L2 started to reject all of these triggers and the dead time smoothly decreased and disappeared around 4:40. As the luminosity slowly decreases during a run, the L1_EM2 trigger rate decreases accordingly. When the trigger rate dropped below 200 Hz at around 6:20, the L2 was set to accepting this triggers again and the L2 input closely followed the L1 output.

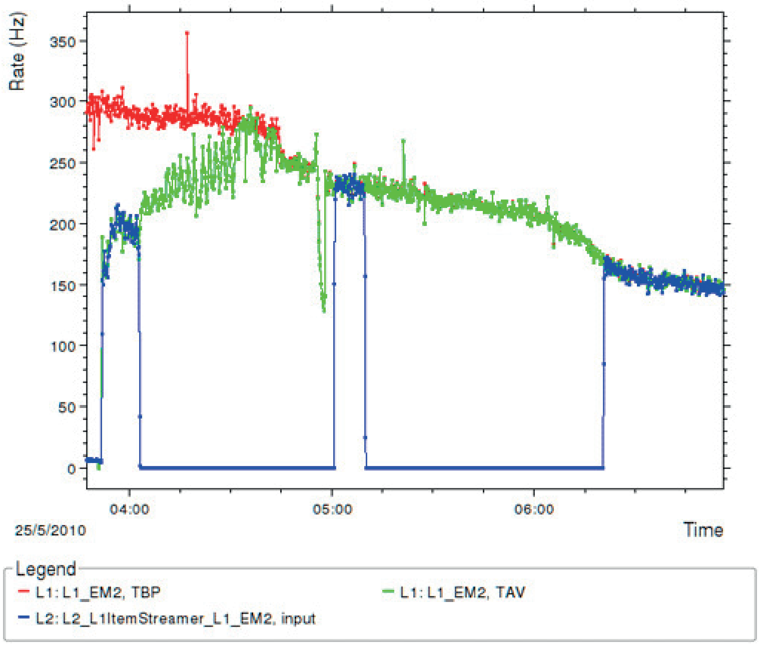

FIGURE 5.3: Example of a dead-time that occurred in an ATLAS run at May 25th, 2010. [118]

A monitoring framework was set up that measures the required computing resources of individual triggers and of complete trigger menus. These measurements can also be used to extrapolate the costs and the trigger rates to higher luminosities. With the use of this framework, the steering of the trigger can be optimized by testing different configurations. A detailed description of the trigger steering and the cost monitoring software is provided in the sections below.

5.1 HLT Steering

Each trigger item consists of a chain of algorithms in the steering software. A chain consists of sequences or steps, which again are formed by one or more

Feature Extraction (FEX) algorithms and one Hypothesis (hypo) algorithm. The former are used to extract complex information from the event, such as a track reconstruction, or the combining of an inner detector and a muon chamber track. FEX algorithms usually consume much more time than hypos, which are used to make relatively simple and quick decisions such as whether a certain p_T threshold is exceeded. The name of a hypo is referred to as a signature and always describes the level and the object that was found at that point, for example L2_e5_medium or L2_muon_standalone. An example of how the complete execution of the mu6 chain evolves is shown in figure 5.4. Because different chains may use the same algorithms, execution time can be reduced by using algorithm results multiple times. Another time reduction is achieved by executing the trigger step by step. If one step leads to the rejection of a chain, the further execution of all chains that rely on this step can then be omitted. Following the same reasoning, prescales are also applied at the beginning of the chain evaluation to avoid redundant calculations.

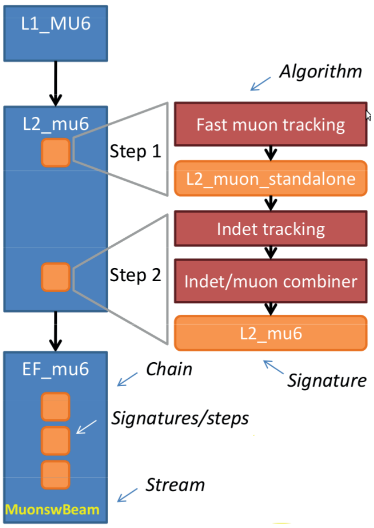

FIGURE 5.4: An example of how the mu6 chain is handled by the trigger. Each step consists of one or more FEX algorithms (e.g. Fast muon tracking) and one hypo (L2_muon_standalone). The name of the established object is referred to as a signature.

The organisation of memory objects in the HLT is called the navigation and can be seen as a tree with nodes and connections between those nodes. The nodes are formed by objects that are called Trigger Elements (TEs). Each TE can be seeded by one or multiple other TEs and seeds one or more TEs itself. Several types of features can be attached to the TEs. Usually, one sequence of algorithms is attached to each TE and determines whether the TE should be activated. Inactive TEs are not taken into further account as the chains with corresponding sequences cannot pass on that specific RoI. A detailed example of how the navigation works is displayed in figure 5.5. The first TE at the top of the tree (not displayed in the figure) has always the operational information of the event attached to itself, such as the number of RoI, the activated chains and the timing. This initial TE seeds the TEs that have RoI descriptors attached. RoI descriptors contain information about the L1 thresholds and the type of the RoI that was provided to the HLT. From this information it can be determined which L2 algorithms should be run on the data coming from the corresponding RoI. In the software this is established by creating a threshold TE that has a sequence of algorithms attached. In figure 5.5 red blocks show the active TEs and violet blocks show the inactive blocks, for which no further calculations should be performed. The colored/dark bands show which FEX algorithms are used multiple times by different chains. The first time the L2PU needs to retrieve the detector data from the ROS-PC, the necessary calculations are done and the result is saved in the cache. Succeeding chains that use the same FEX can then just use the result that was calculated the first time.

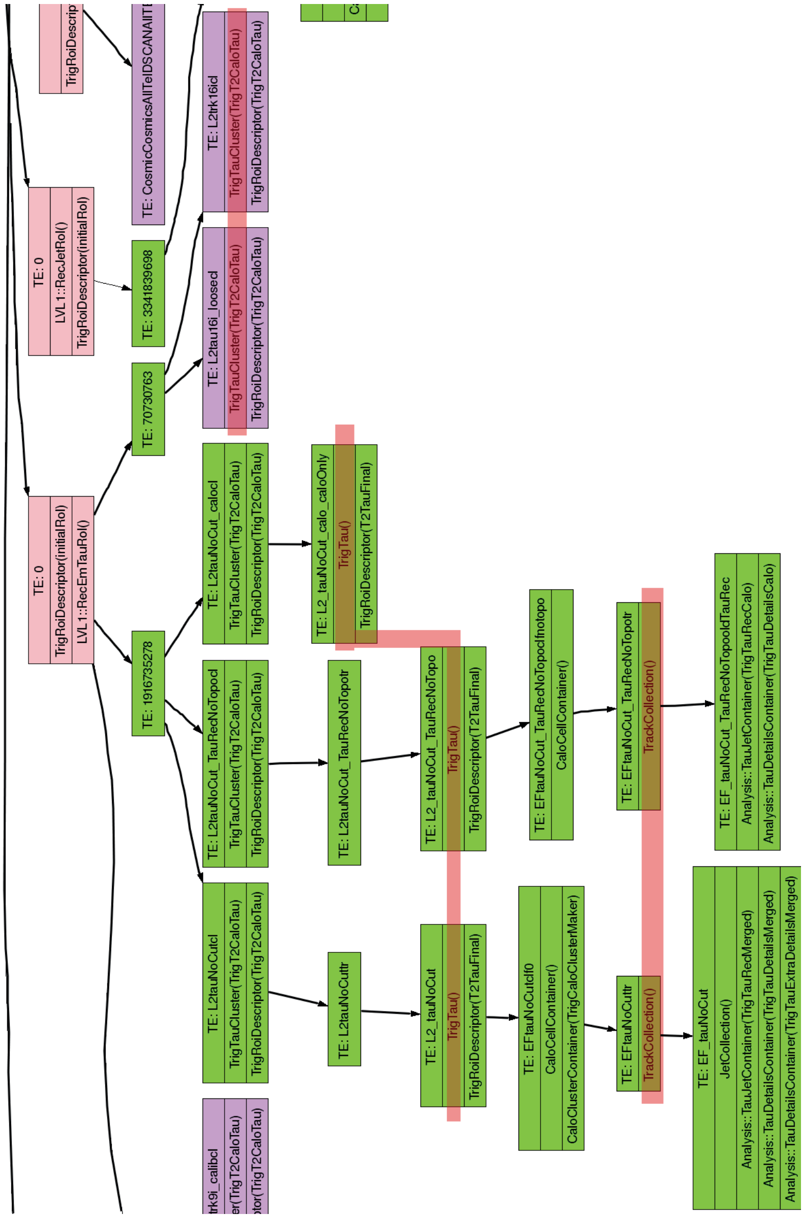

FIGURE 5.5: A graphical display of the HLT navigation. The marked bands indicate that an algorithm was performed multiple times on the same RoI and can therefore be retrieved from the cache.

5.2 Cost Monitoring

To achieve an optimal allocation of the available resources for the trigger system it is necessary to identify the bottlenecks. Once the bottlenecks are identified, it is equally important to monitor the online pressure on the resources. A trigger menu contains hundreds of signatures, and different items may use the same algorithms as explained in the section above. To predict the necessary computing a detailed monitoring framework was developed. The L1, L2 and EF trigger decisions are stored for each event. Once in every ten events, the cost data is extracted from the HLT software and stored on disk. The cost data include the timing of individual algorithms and the retrieval times for the requests from the L2PU to the ROS-PC. A detailed list of the stored information is given below.

- Executed algorithms.
  - Algorithm Id.
  - start and stop time.
  - RoI index.
- Executed sequences.
  - Instances of the algorithms belonging to this sequence as described above.
  - Id of the chain of which this sequence is part of.
  - Information about the the type of sequence. E.g. Was the result retrieved from the cache, was it an initial sequence or was it initiated by another sequence?
- Executed chains.
  - Chain Id
  - Level of the trigger
  - Decision that was established for this chain

- RoI in the event.
  - RoI Id
  - RoI Type (EM, Tau, Muon, Jet, Total energy)
  - Number of L1 thresholds exceeded, this corresponds to an energy level estimated by the CTP.
- Data requests to the ROS-PCs.
  - Time of the request, time of the retrieval.
  - List of ids of the ROBs from which the data was requested, with for each ROB:
    * State of the data request, was it retrieved from the cache or from the ROB itself? Other possibilities are that the ROB was disabled, that it was ignored or the state is unknown.
    * History of the data request, was it retrieved by prefetching (see further on), was the retrieval successful or is the history unknown?
- L1 Items.
  - Identifier of the Item.
  - Information about the L1 decision.
- Trigger Elements, only the output elements for each chain are saved. These contain information about.
  - Id of the corresponding sequence.
  - RoI-id on which the sequence ran.
  - The state and the type, was it active? (was the hypo true?) Was it a L1 threshold? Was it a topological TE?

Four examples of applications of this cost data information are presented in the next section.

5.2.1 Online Cost Monitoring

The results of the cost data analysis from ATLAS runs are automatically published on a website. Average computing time per event, algorithm or signature can easily be monitored from these websites. If one specific trigger item or algorithm uses a disproportionally high share of the cost resources this can easily be identified. Additionally, these online data can also be used to study specific trigger properties. Two examples are the unequal distribution of data requests for different Pixel Detector ROS-PCs and the optimization of the trigger chain performance.

The former example was an issue that discovered by Jos Vermeulen at the end of 2010 and could have lead to problems at higher luminosities because of the overload of one of the ROS-PCs. The reason was that the cabling between the different detector parts and the ROS-PCs was not optimal. The two different cabling schemes are illustrated in figures 5.6 and 5.6.

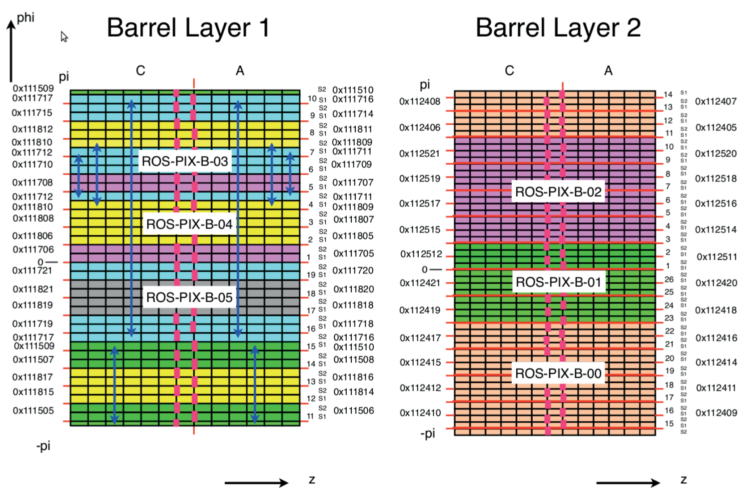

FIGURE 5.6: The original, non-optimal, cabling of the ROS-PCs to the pixel detector. Figure provided by Jos Vermeulen.

The problem with the original lay-out was that the probability was very high that the reconstruction of a single track needs data from two ROS-PCs. Two smaller requests to separate ROS-PCs is more costly than one larger

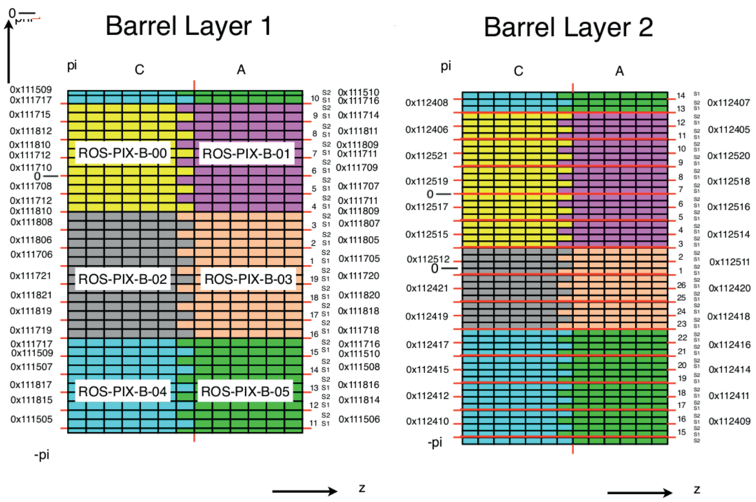

FIGURE 5.7: The improved cabling of the ROS-PCs to the pixel detector. Figure provided by Jos Vermeulen.

request to a single ROS-PC. In addition, the loads of the ROS-PCs was more asymmetric than necessary since ROS-PC-B-05 was hardly ever used in the original lay-out. The latter is a problem as dead time arises whenever one of the ROS-PCs gets overloaded, therefore the distributions of the requests should be as equal as possible. The rate request to the different ROS-PCs for two different lay-outs different is plotted in figure 5.8. The two bands in red and blue correspond to the two layouts that are displayed in figures 5.6 and 5.7. The graph shows that almost all ROS-PCs receive a lower request rate, and the requests are much more evenly distributed.

5.2.2 Rate Predictions

The testing of new trigger menus is done offline. This can be done by using so called Enhanced Bias samples of data, for which only a small selection of prescaled L1 and minimum bias triggers are used for its collection. Each enhanced bias dataset contains around 2 million events and has an advantage that it is still unbiased by the HLT. Enhanced bias triggers include all triggers that seed primary HLT triggers and therefore offers a reliable source of

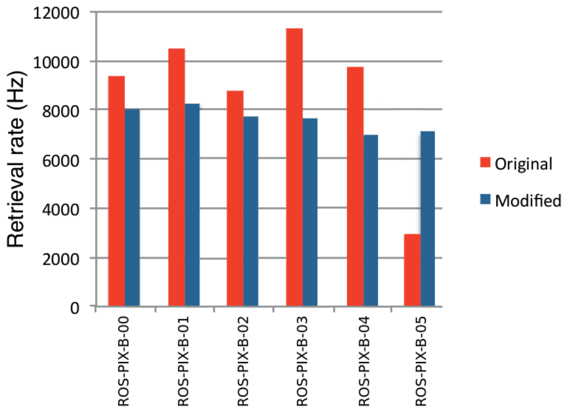

FIGURE 5.8: The request rate to the different pixel detector ROS-PCs, shown for two different lay-outs of the cabling.

L1 input events for the testing of the HLT system. The HLT software can therefore be run offline and new trigger algorithms and combinations of new triggers (trigger menus) can safely be tested and scaled up to expected LHC luminosity. The cost data obtained by the offline running of the HLT can be used to simulate specific parameters such as the data retrievals from the ROS-PCs, the required bandwidth in the network and the processing time per event by the L2PU and the EFPU. By using this method the trigger rates can be predicted within a precision of 1 Hz at a luminosity that is a factor of ten compared to the original enhanced bias sample [119]. The scaling of the rates is performed by applying a linear factor to the rates, obtained by normalising the trigger counts to the integrated luminosity during the enhanced bias run. Linear scaling is considered to be justified for triggers with a high p_T threshold. Meanwhile, the overall trigger rates are dominated by these high p_T triggers and an overall linear scaling factor is considered to be justified. That this presumption is ineed correct can be checked by comparing a set of online trigger rates to the rates that are predicted for that specific luminosity and trigger menu. The results of this check are presented in figure 5.9.

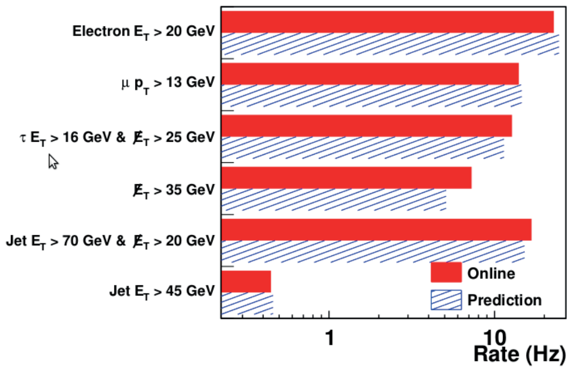

FIGURE 5.9: Comparison of the online EF trigger rates after prescale to those that are predicted offline by using the cost monitoring data [119].

5.2.3 Testing Prefetching

In 2011 a new procedure was proposed to retrieve the data from the ROS-PCs. The default procedure is that each algorithm can make a request for data from a ROB inside one of the ROS-PCs. This request is answered immediately by returning the requested data of that specific ROB. The problem with this procedure is that there can be multiple data requests issued to the same ROS-PC in the case an algorithm needs additional information about an RoI that wasn't requested before. The aim in the new procedure is a decrease in the number of data retrievals by requesting all the ROB data from one ROS-PC for the whole event in one data request. To determine which specific ROBs should be in the request, an inventarisation is taken of all the algorithms that will run in the event and which data they will require. This procedure is called pre-fetching. The advantage of this method will be that less computing power will be required from the ROS-PCs, as the number of requests go down. A disadvantage could be a higher pressure on the bandwidth. Since all data requests by the algorithms are recorded in the cost data, the implications of this new procedure can be simulated offline. The procedure to get this done is the following. First a HLT reprocessing was requested for the enhanced bias run 189421, which was the latest at that point. In this reprocessing (AtlasCAFHLT,16.1.3.14.1, Physics_pp_v3, 3e33 menu), an extra algorithm was used that lists all ROBs that might be requested in that event before all other algorithms run. This list can then later be used to simulate the prefetching as it is explained above. The algorithm to perform this can be summarised as:

- Run over all algorithms in the event.
- Check for all requests done by this algorithm whether there are ROS-PCs that were already in the list made by the Prefetch algorithm.
- If the latter is the case, add the ROBs from the list to the request to this ROS-PC. The history of this request is set to "retrieved", to denote that the data was really retrieved from the ROS-PC.
- If another algorithm, later in time, requests ROBs that are already in this inventorised list, their history should be set to "cached", to denote that the data was already stored in the system.

This is sufficient to simulate the number of requests, as well as the bandwidth used by the data requests. That the number of requests goes down significantly is shown in figure 5.10. The bandwidth that is used is increased by less than 5 %, which is shown in figure 5.11. This means that only a tiny number of ROB requests is done redundantly. The overall result is a decrease in the total retrieval time as this is dominated by the number of requests.

At the moment this study was performed, the request rate per ROS-PC was still well below its limit and it was decided to wait with the actual implementation of the prefetching. The implementation is however still possible in the future.

5.2.4 Predicting Combined Triggers

The cost monitoring software can also be used to calculate the rates of combined triggers using parts that were already in the existing menu. The advantage of using the cost monitoring data for this is that it has all trigger decisions saved in one root-file, separated from the real data. Triggers of different types can be checked by just looking at the chain results. For example,

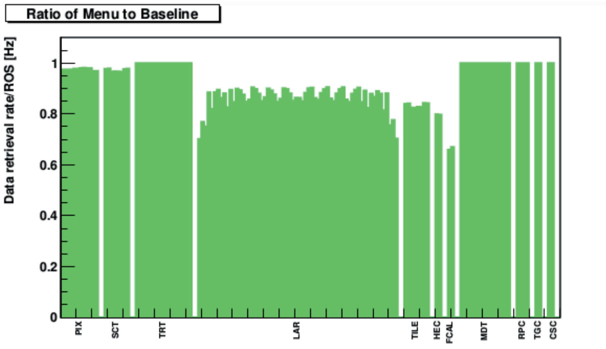

FIGURE 5.10: The ratio between the data requests done to the various ROS-PCs when the new prefetching scheme is used and when the default procedure is used.

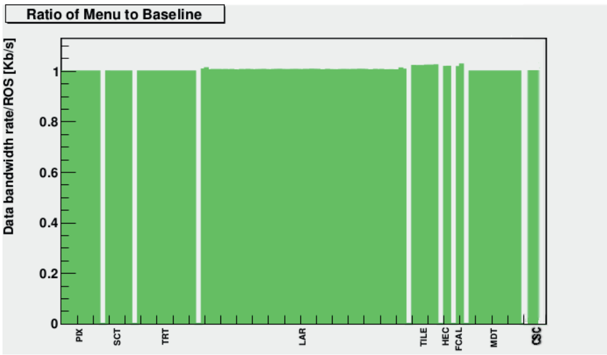

FIGURE 5.11: The ratio of the used bandwidth when using prefetching and without prefetching. The figure shows that the bandwidth is only increased by several percent when requesting data recorded by the TILE, HEC and FCAL subdetectors

when calculating how often the combined item EF_e10 AND EF_xe20 fires, one can just loop over all events and check for each event whether there is a passed chain of both types present. This is not possible for triggers of the same type, for example with EF_e10 AND EF_e10. In this case it is necessary to include the RoI information and this can only be obtained from the TEs. As the TEs are by default not saved into the cost ntuples, it is necessary to save the right information in an efficient way. It was decided that the L1 thresholds, and the output TEs to the L2 and EF are only saved by the offline cost monitoring software. This means that combined trigger calculations with TEs can be performed on all the analyses that are run on the enhanced bias data. In principle, all trigger items can be simulated by using the TEs. From the configuration one can retrieve the output TEs of a certain chain and check whether those output TEs with the same RoI are indeed present in the event. To calculate the rate of a combined trigger with overlap such as EF_e10 AND EF_e10, it is necessary that there are two trigger elements with different RoI present for each of the required sequences: EF_e10_calo, EF_e10_id and EF_e10. Where the latter is the sequence that checks whether the combination of the calorimeter and the inner detector matches.

To check whether the algorithm was implemented correctly, combined triggers that are already implemented in the menu can be compared to the calculated rate of the combination of the two single chains. For example, EF_e5_tight and EF_2e5_tight are both in the trigger menu Physics_pp_v3. For this menu it was checked and confirmed to correspond exactly to the rates of the combined triggers that were calculated in the HLT itself.

Event Reconstruction

Introduction

This chapter focuses on all prerequisites for the actual physics analysis. These prerequisites include the object selection, event selection, background estimation and the evaluation of systematic uncertainties. The first section explains the object and event selection. In this section the algorithms and selection cuts to reconstruct muons, electrons and jets are evaluated. An important part of the event selection is the primary vertex selection, since proton-proton collisions are a potential background to DPI analyses. In the second section I will explain how the size of various backgrounds (Z + 2 jets from SPI, $t\bar{t}$, fake QCD backgrounds, diboson, single top, $Z \rightarrow \tau\tau$) are estimated. In the third section I will summarise all systematic uncertainties and event yields including all uncertainties. An important convention that is used throughout the following chapters is that a lepton is defined as the common denominator for electrons and muons, while τ-leptons are excluded from this definition.

6.1 Object Reconstruction

6.1.1 Electrons

Electrons are reconstructed by an algorithm that matches high energetic clusters in the electromagnetic calorimeter to tracks in the inner detector. The pseudorapidity region is constrained to $|\eta| < 2.46$, while excluding the "crack" regions in $1.37 < |\eta| < 1.52$, where the cables for the inner detector pass through the calorimeter.

Electrons can be identified with three different levels of tightness (loose/medium/tight) based on a large range of variable that can be categorised as following:

- The shape of the electromagnetic shower, combined with information on the energy deposit in the hadronic calorimeter.
- Information on the track-quality, based on the number of pixel,SCT and TRT hits on the track together with the transverse impact parameter d_0.
- Matching between the identified track and the calorimeter deposit.

Z bosons are reconstructed by applying the medium prescription. The advantage of the medium prescription is that it efficiently removes fake leptons from QCD and heavy flavour backgrounds, while retaining a large number of electron candidates. A precise definition and study on the efficiency modelling of electrons, is documented in [120].

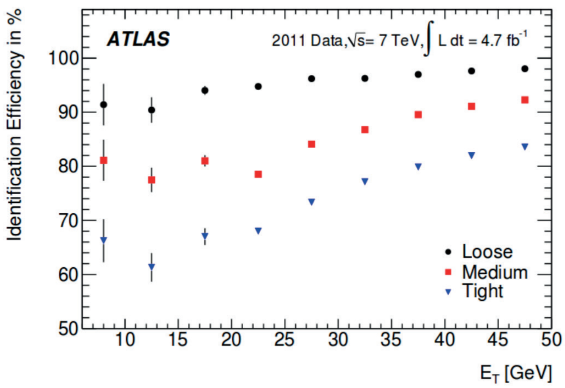

FIGURE 6.1: Electron identification efficiency for three prescriptions of identification criteria as a function of the transverse energy of the electrons. [120].

The p_T of the electron is calculated by using the energy measurement of the calorimeter and the polar angle measured by the ID : $E(calo)/\cosh(\eta(ID))$.

A minimum p_T of the electrons is set to 20 GeV/c^2 in accordance with the cut on the p_T of the muons which is constrained by the trigger threshold of 18 GeV.

6.1.2 Muon Definition

In ATLAS there are three different algorithms that combine the hits in the inner detector and muon spectrometer to reconstruct the muon tracks. These algorithms are referred to as chains. The first chain combines tracks in the muons spectrometer with tracks in the ID, while the second chain performs a complete refit of all the tracks in both the subdetectors. The third chain was developed to combine the best features of both older chains and will be used to reconstruct tracks in this analysis. The reconstruction efficiency of the third chain muons is significantly higher than for the other two chains as was presented in [121]. Only combined muons are used in this analysis, muons that have a track in both the inner detector and the spectrometer. An indication of the reconstruction efficiency of muons was already provided in figure 4.10.

In addition to the default third chain prescription, a set of additional inner detector requirements on muons are applied: The track in the inner detector should have at least:

- 1 pixel hit, or an expected hit in a dead pixel.
- 5 SCT hits, or expected hits in dead sensors.
- A successful TRT extension if the track is in the range of $0.1 < |\eta| < 1.9$).

To reduce the selection of muons originating from hadronic decays and long living particle decays, the transverse impact parameter significance ($\frac{d_0}{\sigma_{d0}}$), defined in chapter 4, is required to be smaller than three. Another requirement to reduce the background from hadronic activity is the muon isolation. The summed p_T of all particles in a cone of $\Delta R < 0.2$ (ΔR as in eq. 7.7) around the muon should be less than 10 % of its own p_T. Muons can be measured in the pseudorapdity region up to 2.4 and their p_T is required to be larger than 20 GeV, which is well above the trigger threshold of 18 GeV.

6.1.3 Jet Reconstruction

6.1.3.1 Jet Algorithm

Jets are clustered according to a sequential recombination algorithm, which means they are reconstructed by iteratively recombining individual final state particles (or calorimeter cells) based on a certain measurement of the kinematic distance between the the particles. The recombined particles are then called pseudo jets and will be used as an input to the next step of the algorithm. The algorithm is iterated until there are no pseudo jets in the vicinity of each other closer than a certain value R. All sequential recombination algorithms in general are stable w.r.t. infrared and collinear emissions. The difference between the algorithms are how the distance between the pseudo jets is measured. In the Anti-k_t [122] algorithm as used in ATLAS, the distance between particles is defined as:

$$d_{i,j} = min(1/k_{Ti}^2, 1/k_{Tj}^2)\Delta R(i,j), \tag{6.1}$$

where $\Delta R(i,j)$ is defined by equation 7.7. Iterative recombination algorithms function in such a way that in each step the two closest particles (according to formula 6.1) are combined. Once the smallest $d_{i,j}$ between a pseudo jet and any other particle j is larger than a parameter R, this pseudo jet is upgraded to a jet. In this analysis the parameter R is set to 0.4.

In the case that both particles i and j are soft, the momentum factor ($min(1/k_{Ti}^2, 1/k_{Tj}^2)$ in eq. 6.1) will be large. If either one of the particles i or j is hard and the other is soft, the distance will on the other hand be small and they will form a pseudo jet, depending on their separation $\Delta R(i,j)$.

The advantage of this definition is that the 2D-shape of a jet is very close to a circle in $\eta - \phi$-space, while the 2D-shape is very insensitive to additional soft particles. This means that if a new soft particle is added to the event, it is predictable to which jet it will be added. Because the jet surface is well defined, the estimation of pile up contribution has a smaller uncertainty w.r.t. other jet definitions [123].

6.1.3.2 Jet Calibration

In theory, the inputs to the jet algorithm are hadronic particles. However, in a detector one cannot always distinguish individual particles. Instead the most precise input that is available are the energy deposits in calorimeter cells. In ATLAS, these cells are called topological clusters. Figure 6.2 shows a schematic overview of the reconstruction and calibration procedure of jets in ATLAS.

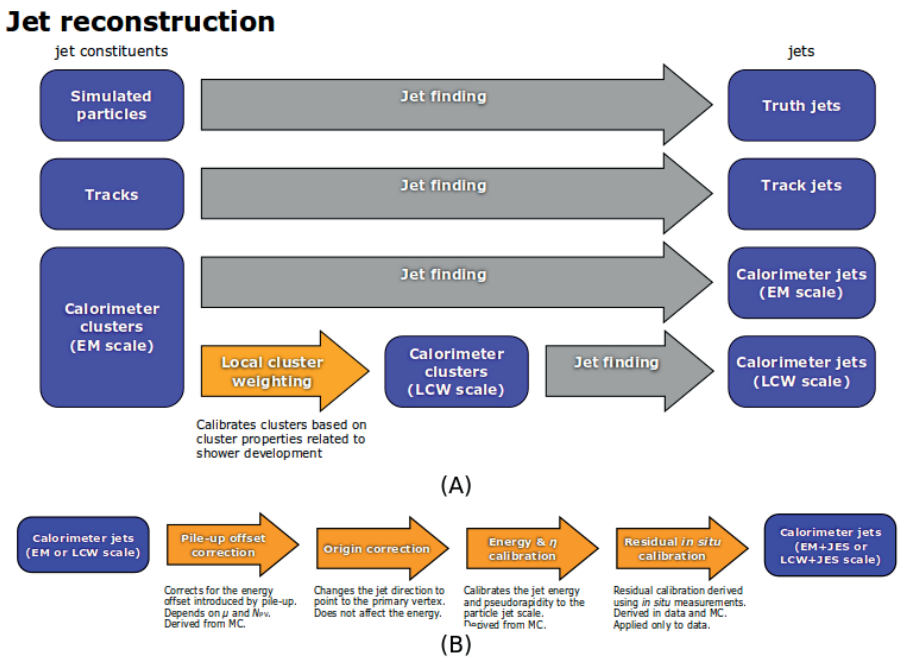

FIGURE 6.2: Schematical overview of the jet reconstruction and calibration procedure in the ATLAS detector [124]. (A) The different inputs to the jet algorithm are truth particles, tracks or calorimeter clusters. Calorimeter clusters can either be calibrated before (LCW) or after the jet finding (EM). (B) After the (EM/LCW) calorimeter clusters are recombined to form jets, a Jet Energy Scale (JES) adjustment is applied to further apply a calibration to the jets.

Part 6.2 (A) shows the different types of input to a jet finding algorithm: Tracks and calorimeter clusters in case of detector reconstruction result in track jets and calorimeter jets, respectively. The calorimeter jets used in this analysis use Local Calibration Weights (LCW). This means that calorimeter clusters are first calibrated before they are provided to the jet algorithm (lowest line in figure 6.2 (A)).

After the jet algorithm provides its jet definitions, an additional Jet Energy Scale (JES) correction is applied as is shown in figure 6.2. This correction includes pile up subtraction, an origin correction that forces the jet to point at the reconstructed primary vertex, a MC-dependent calibration and an in situ calibration applied. All are applied to each jet individually. The MC calibrations are derived from comparing MC truth jets to fully simulated jets and deriving correction factors as a function of the p_T and the pseudorapidity of the jets. In situ calibrations are derived from measuring the momentum balance in events where a jet recoils against a Z boson or a photon, which both can be measured with high precision.

The uncertainty on measured jet properties are especially high in the regions of low p_T and large pseudorapidity as is shown later in this chapter in figure 6.10. The DPI/SPI ratio, however, drops for higher transverse momenta since DPI jets do not recoil against a heavy object such as the Z-boson. At the same time, the ratio does not depend on the pseudorapidity. The pseudorapidity of the jets is therefore restricted to $|\eta| < 2.4$. At the same time, the threshold on the p_T of the jets is lowered to 25 GeV, which does not significantly increase the systematic uncertainty in the central region. The choice for these kinematic jet cuts is supported at the end of this chapter, in tables 6.6 and 6.7, where the uncertainties are summarised for different cuts.

6.1.3.3 JVF Cut

At the high luminosity of the 2012 LHC dataset ($\approx 6 - 8 \cdot 10^{33}$ cm^{-2}s^{-2}), the possibility arises that there is so much pileup in the event that a jet can be reconstructed by only pileup contribution. To reduce the probability that clusters with high pileup activity are selected as real jets, a Jet Vertex Fraction (JVF) cut is be applied. The JVF is computed centrally and is defined as the scalar sum of the p_T of the tracks in the jet area coming from the same primary vertex, divided by the scalar p_T sum of all tracks in the jet area.

$$JVF(jet_i, vtx_j) = \frac{\sum_k |p_T|(trk_k^{jet_i}, vtx_j)}{\sum_n \sum_p |p_T|(trk_p^{jet_i}, vtx_n)}. \tag{6.2}$$

The JVF should be higher than 50 % for jets with a p_T lower than 50 GeV. This cut was studied by the Jet-Etmiss group in ATLAS and figure 6.3 shows that it very effectively rejects jets from pileup.

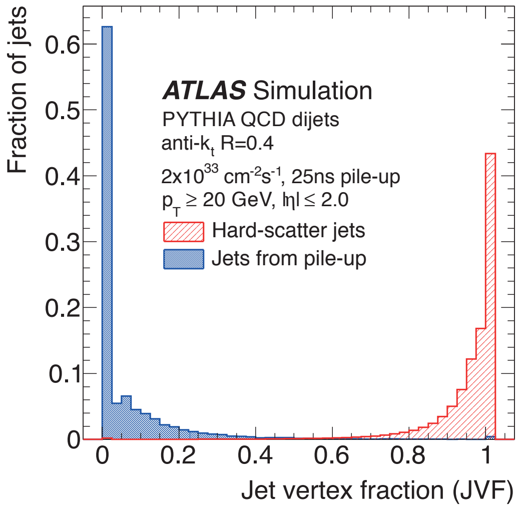

Figure 6.3: The effectivity of the JVF cut for the reduction of pileup jets.

6.1.3.4 Overlap Removal

An additional requirement that is applied to the jets in the Z selection, is that they should not overlap with the leptons. If there is an accepted lepton in the vicinity of $\Delta R(l, j) < 0.4$, the jet is removed from the list of jet candidates.

The cut on $\Delta R(l, j)$ is specific to the Z + 2 jets event category and cannot be applied directly to the 2jets event category. However an additional correction is applied to to ensure that the same efficiency in both event categories is achieved. For this purpose, a 2 dimensional histogram of the leading and sub leading lepton pseudorapidity and azimuthal angle (η, ϕ) is measured from the Z + 2 jets data. In the 2 jets selection the directions of the leptons are sampled from this histogram and if a jet overlaps with one of these sampled lepton directions, it is removed from the list of jet candidates.

6.1.4 Summary

In this chapter I described all the reconstruction methods for the three important types of physics objects: electrons, muons and jets. In the next section the definitions of the full event reconstruction for three different categories will be explained. Table 6.1 summarises the selection requirements for the three different physics objects.

Electrons	Muons	Jets
Medium identification	3^{rd} chain muons	LCW+JES calibration
	$\frac{\sum_{\Delta R<0.2} p_T(track)}{p_T(Muon)} < 0.1$	Anti-k_T algorithm
	$\frac{d_0}{\sigma_{d0}} < 3$	$JVF > 0.5$
	ID hit requirements	$\Delta R(l, j) > 0.4$
$p_T > 20$ GeV	$p_T > 20$ GeV	$p_T > 25$ GeV
$1.37 < \lvert\eta\rvert < 1.52$ or	$\lvert\eta\rvert < 2.4$	$\lvert\eta\rvert < 2.4$
$\lvert\eta\rvert < 2.47$		

Table 6.1: Object selection summary.

6.2 Event Selection

The calculation of σ_{eff} depends on three separate cross section as is indicated by equation 2.6. In the case of a DPI measurement in Z + 2 jets events, the three cross sections are for the σ_{Z+0jet}, σ_{2jets} and $\sigma^{DPI}_{Z+2jets}$ (Z + 2 jets events solely from the DPI process). The measurements of these three input cross sections is done by defining three categories of different event selections as indicated in table 6.2. The object selection for three categories is the same and summarised in table 6.1. A minor difference between the jet selections in the Z + 2 jets and the 2jet categories is in the lepton overlap removal that is applied artificially to the jets in the 2 jets category as described in section 6.1.3.4.

Selection category	Pre-selection	Trigger	N-leptons	N-jets
Z + 2 jets	✓	Lepton	2	2
Z + 0 jet	✓	Lepton	2	0
2 jets	✓	Jet (prescaled)	0	2

Table 6.2: Summary of event selections for the three different categories.

A Z boson is selected by requiring two oppositely charged, equally flavored leptons to have an invariant mass between 71 and 101 GeV/c^2. In addition to selecting a specific number of objects in each event category, events should also pass vertex reconstruction, trigger and data quality requirements. These will be described in the following sections.

6.2.1 Vertex Reconstruction

In the context of the high pileup conditions in the 2012 dataset, it is crucial to identify each proton-proton collision as precisely as possible. A precise vertex reconstruction is especially important for DPI analyses, since additional proton-proton collisions are a potential background to these processes. A comprehensive explanation on how vertices are reconstructed in ATLAS can be found in for example [125]. In this section, primarily the performance and its influence on vertex merging will be evaluated. The performance of the vertex reconstruction in ATLAS was addressed in [126]. The vertex resolution can be extracted from the data by measuring the distance between two vertices in a large dataset. The result is shown in figure 6.4. With a perfect vertex reconstruction, the distribution of the distance between two vertices would be a Gaussian with a width of $\sqrt{2}$ times the length of the beam spot. However, the figure shows a drop around $\Delta Z = 0$, which indicates that vertices are very likely to merge if they are closer than ≈ 5 mm.

Next to the possibility of two vertices merging, a single vertex could also be misreconstructed as two separate vertices. This phenomenon is called a

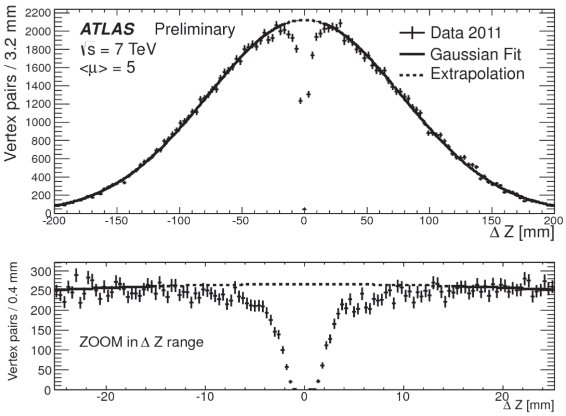

FIGURE 6.4: Distance between two reconstructed vertices. The drop at $\Delta Z = 0$ shows that vertices are likely to merge when they are closer than ≈ 5 mm. [126]

split vertex. Even though ATLAS has a very precise vertex reconstruction, there will be primary vertices with contamination of pileup vertices. Figure 6.5 shows the fraction of vertices with low pileup contribution ($> 30\%$, blue line), high pileup contribution ($> 50\%$, red line) and split vertices (green) as a function of the number of proton-proton interactions per bunch crossing (μ). The figure indicates that for a number of interactions per bunch crossing of 20, approximately 5% of the vertices have a low contamination from pileup and even less have a high contamination. For a very large number of interactions per bunch crossing (40), these values are approximately twice as high.

A merged vertex causes a potential background to DPI events. If for example a Z boson was created in a vertex and the pileup influence causes a high deposition of energy in the calorimeter, a jet could be mimicked that is not vetoed by the JVF cut. Another case is that two real hard jets are produced in the second vertex. However, we can assume that these two cases form only a small fraction of the cases in which two vertices merge since the di-jet cross section decreases exponentially as a function of the p_T and the majority of vertices are dominated by low-p_T QCD interactions. Therefore we can safely assume that merged vertices are only a very small background to

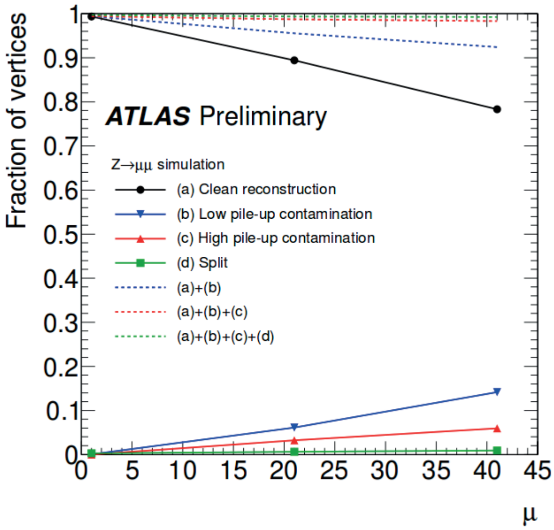

FIGURE 6.5: Different scenarios in pileup reconstruction as a function of the interactions per bunch crossing: clean reconstruction (black line), merged vertices with low pileup contribution (blue line) or high pileup contribution (red line), and split vertices (green line). [126]

DPI processes. Nonetheless, the influence of pileup on the vertex reconstruction should still be incorporated in the detector simulation of events. This can be achieved by adding "minimum bias" events to the event record before applying GEANT simulation of the ATLAS detector. A minimum bias event is defined as all types of inelastic non-diffractive proton-proton collisions and includes soft QCD, hard QCD and electroweak processes. If the distribution of the number of added minimum bias events is matched to the distribution of the interactions per bunch crossing in the event selection, this method should very reliably include the influence from proton-proton collisions. In figure 6.6 the number of primary vertices per bunch crossing is measured as a function of the number of interactions per bunch crossings in 2011 data. The figure shows a very good agreement between simulation and data and therefore indicates that the simulation of the vertex reconstruction is very well modelled.

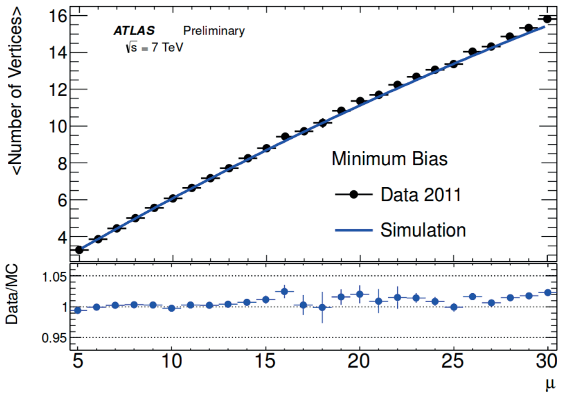

FIGURE 6.6: Comparison between data and simulation of the number of primary vertices as a function of the number interactions per bunch crossings. The figure shows a very good agreement between data and Monte Carlo and therefore indicates a very good modelling of the vertex reconstruction. [126]

6.2.2 Data Quality Requirements

Before selecting the event, it should fulfill a number of data quality conditions, usually referred to as the pre-selection criteria. The primary vertex of the event should at least have three assigned inner detector tracks. Events in which there are indicated errors in the LAr calorimeter and the Tile calorimeter are vetoed. An event is also vetoed if a jet is likely to originate from either electronic noise in the calorimeters or from non-collision background. The presence of such a "bad" jet indicates that other parts of the detector are likely to be influenced by electronic noise or non-collision background and it is safer to veto the complete event.

6.2.3 Event Triggering

Events in the Z+ 0,2 jet categories are selected by applying di-lepton triggers. The muon trigger is EF_mu18_tight_mu8_EFFS. The two electron triggers, of which either one is required to be fired, are: EF_2e12Tvh_loose1 and EF_2e12Tvh_loose1_L2StarB.

The triggering for the 2 jets selection is a somewhat more complex procedure, as there are twelve different triggers with each different prescales and momentum thresholds. An event is only accepted if the jet p_T is above the 99.5 % efficiency threshold of the trigger. A summary of which prescales are applied and which jet momentum thresholds are required for each jet trigger is presented in table 6.3.

Leading jet p_T	Fired trigger	Luminosity weight
25 GeV $< p_T <$ 50 GeV	EF_j15_a4tchad	8/0.014734
50 GeV $< p_T <$ 100 GeV	EF_j25_a4tchad	8/0.014734
100 GeV $< p_T <$ 136 GeV	EF_j55_a4tchad	1/0.441786
136 GeV $< p_T <$ 190 GeV	EF_j80_a4tchad	1/2.3164
190 GeV $< p_T <$ 204 GeV	EF_j110_a4tchad	1/9.81141
204 GeV $< p_T <$ 252 GeV	EF_j145_a4tchad	1/36.2647
252 GeV $< p_T <$ 304 GeV	EF_j180_a4tchad	1/78.7753
304 GeV $< p_T <$ 404 GeV	EF_j220_a4tchad	1/261.379
404 GeV $< p_T <$ 522 GeV	EF_j280_a4tchad	1/1164.69
$p_T >$ 522 GeV	EF_j360_a4tchad	1./20277.1

TABLE 6.3: Applied luminosity weights as a function of the leading jet p_T and the fired trigger for the 2 jets event selection.

6.3 Background Estimation

The largest background to Z + 2 jets production from DPI is Z + 2 jets from SPI. Chapter 3 explains how this background can be estimated by using MC techniques. Other backgrounds to Z production are the dileptonic decay channel of $t\bar{t}$, diboson processes WW,WZ,ZZ, single top and QCD multijet events in which leptons are produced in the jet formation, or jets are misreconstructed as leptons. Finally, events where a Z-boson decays into two τ-leptons, which both decay into either two electrons or muons are also regarded as background. The QCD background is estimated by exploiting a data-driven method. This cannot be estimated by using simulation, since the effect that a jet fakes an isolated lepton only occurs very rarely ($\approx 0.001\%$ of the jets fake a lepton [127]) and would therefore require a very large set of detector-simulated events. For the $t\bar{t}$ and single top backgrounds, three combined control regions are defined in which the estimations of MC generators are verified. The other backgrounds are estimated purely by the use of MC generators. In the next two sections I will explain how the control regions for the top and QCD processes are constructed.

6.3.1 Top Control Regions

The basic selection for the top control regions is the same as for the $Z \to ll$ selection, but requiring an electron together with a muon, instead of two same-flavour leptons. At least two jets should be reconstructed. To reduce the remaining backgrounds, there are three separate requirements applied for the three Control Regions (CR):

- CR 1: $p_T(jet_1) > 80$ GeV
- CR 2: $ET_{Miss} > 60$ GeV
- CR 3: At least one b-tagged jet

Figure 6.7 shows the number of jets for the three control regions in comparison to the prediction given by the POWHEG+Pythia generator combination. They show that the number of jets is very well modelled by this generator up to a number of 6 jets. The modelling of the number of jets in an event is sensitive to higher order effects. Showing that this distribution is well modelled for more than two jets is an indication of a good modelling of the overall event topology.

In addition to the number of jets, also other variables are tested. For example, the p_T of the jets and the azimuthal angle between the jets are described very well by the MC. The conclusion of this study is that it is justified to estimate the top-related backgrounds by using the POWHEG+Pythia MC sample.

6.3.2 Fake Backgrounds

QCD-processes can produce a background to Z + jets events in two ways: either real leptons are created in the formation of jets and pass the isolation and

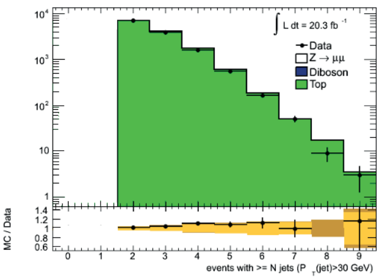

(A)

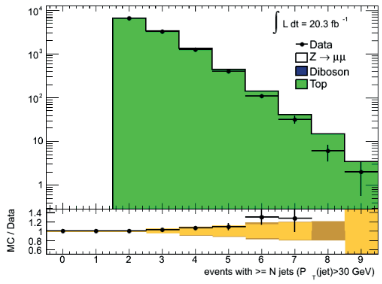

(B)

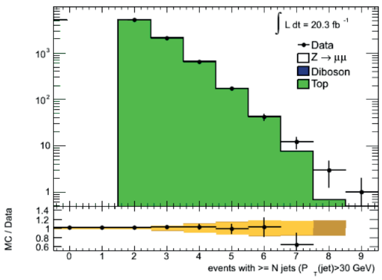

(C)

FIGURE 6.7: Number of jets for the three $t\bar{t}$ control regions: requiring of a high-p_T jet (A), a large E_{TMiss} (B) or at least one b-tagged jet (C). These plots are produced by Ulrike Blumenschein in an unpublished private study.

vertex requirements or hadrons in the jets cause signals in the EM-calorimeter or muon spectrometer which mimic real leptons. To assess these backgrounds a data driven technique is used, which is explained below.

A control region for the fake QCD background can be constructed by only selecting leptons that are very likely originating from jets. In selecting signal events in the muon channel, the isolation and the d_0 requirements are primarily used to reduce the selection of muons faked by jets. For the electron channel the Medium++ prescription already includes requirements that reduce the influence of QCD pollution. Those requirements, as listed in table 6.1, can be inverted to select a pure sample of QCD-events. For electrons, we will create a template by using same-sign Loose++ electrons that do not pass the Medium++ requirements. For muons, the d_0-significance cut is inverted, while the isolation requirement of the muons is dropped. A systematic uncertainty on the shape of the template is derived by using two different sets of cuts. The first is created from inverting the isolation, while keeping the d_0 significance cut. The second is created by inverting the isolation, while dropping the d_0 significance cut.

Because this control region is kinematically very close to the signal region, the events can be used to estimate the shapes of the background in the signal region. To determine the size or the normalisation of the QCD background, we are fitting the QCD template together with all the electroweak backgrounds to the measured data of the reconstructed Z-mass in a large mass-window (50-150 GeV). The uncertainties on the normalization include:

- The statistical uncertainty on the fit
- The systematic uncertainties on the electroweak template, including the JES,JER,lepton scale/ID, trigger efficiency and pileup uncertainties.
- A variation in the fitted mass range
- A variation on the QCD-template (only in the muon-channel)
- A variation in the MC-prediction for the $Z \rightarrow ll$ template, where the alternative template is taken from the Sherpa (MENLOPS) generator.

Figures 6.8 and 6.9 show the resulting templates in the full Z-mass region for the 0 jet and 2 jets selections. Table 6.4 shows the resulting fraction of QCD events in the full mass region and all its errors. The fraction of events under the Z-peak (71-111 GeV) is in the order of three times smaller than the fraction in the full mass range.

6.4 Uncertainties

Each item in the event selection incurs a corresponding uncertainty. The dominating uncertainties originate from the measurements of the jet energy, although we are also including the uncertainties on the muon energy, the trigger efficiency and the pileup reweighting procedure. Below I will explain how

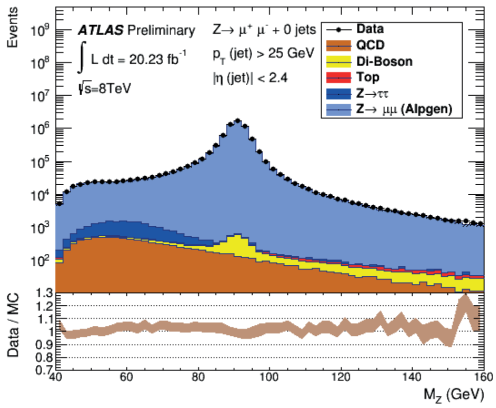

FIGURE 6.8: Overview of all processes contributing to events with 2 muons + 0 jets in the extended M(Z) (=M_{ll}) spectrum.

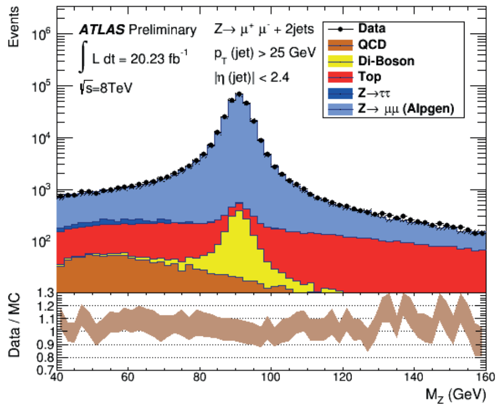

FIGURE 6.9: Overview of all processes contributing to events with 2 muons + 2 jets in the extended M(Z) (=M_{ll}) spectrum.

	Muon channel		Electron channel	
	Njet = 0	Njet = 2	Njet = 0	Njet = 2
Estimated event yield:	3.8e+03	6.5e+02	2.5e+04	2.0e+03
Statistical error:	7.7 %	12 %	1.3 %	4.4 %
Experimental uncertainty:	23 %	21 %	18 %	12 %
Fit range variation:	47 %	30 %	9.4 %	7.3 %
Model uncertainty:	46 %	49 %	5.7 %	6.8 %
Template variation:	12	3	X	X
Total uncertainty:	69 %	54 %	20 %	15 %

TABLE 6.4: QCD fractions in Z $\rightarrow l\hat{l}$+jets events in the Z-mass range 50-150 GeV

the various uncertainties are estimated and summarise the different components.

6.4.1 Jet Energy Scale

The calibration of the calorimeters that is used is referred to as Local Cell Weighting (LCW) [124]. In this scheme, the calorimeter clusters are calibrated by using properties determined prior to the jet finding algorithm. The calibration weights are determined from a GEANT simulation of the energy measurement of charged and neutral pions in the calorimeter. The uncertainty on the calibration is measured in [124] and is broken down into sets of separate components. For this analysis we are using a set of 15 independent nuisance parameters:

- six parameters as measured from in-situ analyses
- two parameters from the eta-intercalibration uncertainty
- four parameters that model the uncertainty on the pileup correction
- one parameter that models the uncertainty on the flavour composition of the jet
- one parameter that models the uncertainty on the flavour response

The uncertainties are propagated by re-running the analysis twice for each parameter and scale the jet energy up/down according to the uncertainty. A summary of these parameters as a function of the pseudorapidity and the p_T of the jet is shown in figure 6.10

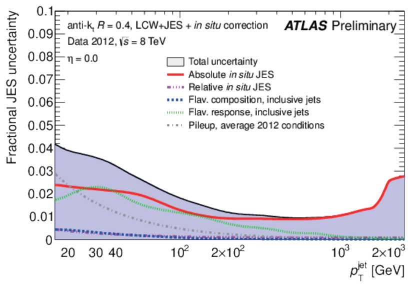

(A) Uncertainty on the Jet Energy Scale as a function of the p_T of central jets.

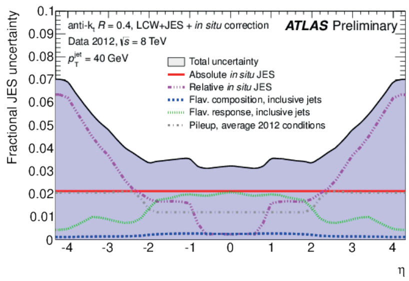

(B) Uncertainty on the Jet Energy Scale as a function of the pseudorapidity of jets with a $p_T \approx 40$ GeV.

FIGURE 6.10: Uncertainty on the Jet Energy Scale as a function of the p_T and the pseudorapidity.

6.4.2 Jet Energy Resolution

Next to an uncertainty on the jet calibrations, calorimeters also have a finite jet energy resolution. The modelling of the energy resolution of the jet measurements is done by the GEANT simulation and was tested in [128]. A result from this study is shown in figure 6.11, in which the jet resolution is compared between data and simulated events as a function of the jet balance of the leading two jets in an event. The graph shows that for central jets the detector simulation is describing the resolution within the uncertainty interval for central jets ($|y| < 0.8$). In this study the uncertainty on the resolution was summarised, of which the relevant information can be found in table 6.5.

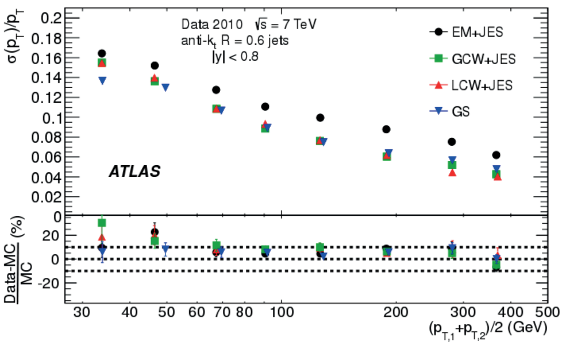

FIGURE 6.11: Resolution on the jet energy as measured in the data, for four different calibration schemes. The measured resolution is compared to the resolution obtained from the GEANT model in the lower plot.

TABLE 6.5: Uncertainty on the jet energy resolution as a function of three p_T bins and four rapidity bins.

Rapidity range	$p_T < 100$ GeV	100 GeV $< p_T <$ 250 GeV	$p_T > 250$ GeV
$0 < \|y\| < 0.8$	17%	15%	11%
$0.8 < \|y\| < 1.2$	20%	17%	14%
$1.2 < \|y\| < 2.1$	20%	17%	18%
$2.1 < \|y\| < 2.8$	20%	17%	18%

The uncertainty on the jet energy resolution in the event selections can be modelled by applying an additional smearing on the jets after the GEANT simulation. However, additional smearing only models the upward variation. Since it is not possible to undo the smearing due to the GEANT simulation if the original jet momentum is not known, the downward variation is calculated by symmetrising the final distribution.

6.4.3 Jet Vertex Fraction

A well tested variable that discriminates between real jets and pileup jets is the JVF as was shown in [129]. The fraction of tracks associated to a jet from the same primary vertex carries an uncertainty due to track reconstruction inefficiencies. This uncertainty is estimated by rerunning the analysis with a JVF cut on the jet selection of 0.47 and 0.53 according to the official ATLAS recommendation.

6.4.4 Lepton Uncertainties

Just as with the jets, lepton measurements are also subject to uncertainties on their scale and resolution. By comparing the lepton energy on measured and simulated data, corrections can be derived to improve the detector modelling. Each of these corrections will carry an uncertainty, and together they model the uncertainty on lepton measurements.

Uncertainties on the muons can be divided in three categories. The first is the uncertainty on the scale correction, the second is the uncertainty on the resolution correction and the third is the uncertainty on the identification of the muon. For the electrons there is an additional correction applied for its reconstruction efficiency.

The uncertainty on the event acceptancy due to the lepton uncertainties are negligible in comparison to the jet uncertainties.

6.4.5 Trigger efficiency

The performance of the lepton triggers is modelled in the GEANT detector simulation of ATLAS and the differences between the data and the simulation is measured [130],[131]. A correction for these differences is applied by using a scale-factor, which is defined by equation 6.3.

$$SF = \frac{1 - \prod_{n=1}^{N}(1 - \epsilon_{Data,n})}{1 - \prod_{n=1}^{N}(1 - \epsilon_{MC,n})}. \tag{6.3}$$

The systematic errors for these scale factors are determined by varying input assumptions on its derivation, such as the momentum resolution, the bin-size, the matching requirement of the tag-and-probe method and the MC-simulation model. The total uncertainty on the triggering is 1.4 % for the electron trigger and 4% for the muon trigger. This difference is likely to originate from the high upper threshold of 18 GeV in the muon trigger which is close to the muon selection threshold of 20 GeV.

6.4.6 Pile-up Reweighting

Effects from pileup are modelled by adding simulated minimum bias events to the MC-event. After the simulation is performed, the average number of interactions per bunch crossing in MC-samples is compared to the actual distribution in the data and MC-events are re-weighted in such a way that the distributions will match afterwards. A systematic variation is derived by varying the average correction with 3%. The propagated error to the final event selection is in the order of 1% as is shown in tables 6.6 and 6.7.

6.4.7 Theoretical Uncertainty

Modelling Z boson production in proton-proton collisions depends on a number of parameters with non-negligible uncertainty. In chapter 3 it was already explained that there are various methods of modelling the production of a Z associated with two jets. In short, the uncertainty can be divided in five categories:

- The PDF uncertainty
- Uncertainties in the modelling of the hard scattering
- Uncertainties in modelling virtual corrections (the parton shower)

- Uncertainties in modelling non-perturbative corrections in the hadronisation process
- Uncertainties in the underlying event model

Ideally, all these uncertainties are addressed separately and most of these categories should even be broken down into several sub-sources of uncertainty. However, the necessary ATLAS samples to calculate these uncertainties are not available. Instead of evaluating these sources separately, the difference between the Alpgen+Pythia6 and the Sherpa generators will be used as an estimations of the theoretical uncertainty. The MPI partons cannot be traced in the samples from these generators and therefore the following assumption is made. The relative bin-by-bin uncertainty derived from the Alpgen+Pythia6 and the Sherpa generators is assumed to be independent of the DPI veto. Therefore the up and down variations obtained from comparing the Alpgen+Pythia6 and the Sherpa generators can directly be applied on the histograms obtained from the Alpgen+Herwig+Jimmy generator configuration in which the DPI events are vetoed. The up and down variations are calculated as;

$$\alpha_{+} = \frac{Alpgen - Sherpa}{Alpgen + Sherpa} \tag{6.4}$$

$$\alpha_{-} = \frac{Sherpa - Alpgen}{Alpgen + Sherpa}. \tag{6.5}$$

And they are applied as:

$$Theory_{+} = (1 + \alpha_{+}) \cdot AlpgenJimmy_{DPI-veto} \tag{6.6}$$

$$Theory_{-} = (1 + \alpha_{-}) \cdot AlpgenJimmy_{DPI-veto}. \tag{6.7}$$

6.4.8 Summarised Estimated Uncertainties

If the uncertainties are uncorrelated, they can be added square-wise to estimate the total uncertainty. Tables 6.6 and 6.7 show the estimated uncertainties on the total event selection for different jet selections It must be noted that the uncertainty on the total event selection might be very different from the propagated errors on the f_{DPI} extraction, as especially shape uncertainties are of influence on f_{DPI}. Since the jet selection is an open parameter in the analysis, in order to minimise the error on f_{DPI}, tables 6.6 and 6.7 show the uncertainties on the Z + 2 jets for three different p_T cuts and also for three different selection criteria w.r.t. the pseudorapidity and JVF. These errors are calculated with the Alpgen+Pythia6 MEPS samples.

	$p_T > 20$	$p_T > 25$	$p_T > 30$
JES:	10.9 %	10.6 %	10.8 %
JER:	8.49%	6.49%	5.94 %
JVF:	2.58%	1.51%	0.92%
Pileup distribution:	0.32%	0.19%	0.11%
Muon:	1.04%	1.05%	1.05%
Muon Trigger:	4.00%	4.00%	4.00%
Electron:	0.7%	0.7%	0.7%
Electron Trigger:	1.6%	1.6%	1.6%
Statistics:	0.15%	0.18%	0.21%
Total:	14.7 %	13.2 %	13.0%

TABLE 6.6: Uncertainties on the total Z + 2 jets selection as a function of the jet p_T, jets are only measured in the region $|\eta| < 2.4$ and a JVF cut of 0.5 is applied. It is striking that the JES is independent inside this region, while the JER increases for lower transverse jet momenta.

A general conclusion that can be drawn from these tables is that a restriction to the inner detector region and on top of that, applying a higher JVF cut reduces the uncertainty largely. Furthermore, when the most restricted region is used to measure jets, the p_T of the jets can be reduced from 30 GeV to 25 GeV without increasing the uncertainty much.

The uncertainties on the jet measurements in the 2 jet category are very similar to the uncertainties in the Z + 2 jets category. However, the spectrum of the p_T of the jets is declining more rapidly than the spectrum of the jet p_T in the Z + 2 jets category. Therefore the uncertainties in the 2 jet category will be somewhat larger. Figure 6.12 shows the spectrum of the subleading jet for the 2 jet category for the data and Powheg+Pythia MC sample that is used to estimate the uncertainties. The figure shows that the MC prediction describes the data correctly, except for the lowest transverse momenta where

	$\lvert\eta\rvert < 4.4$, $\lvert JVF\rvert > 0.25$	$\lvert\eta\rvert < 2.4$, $\lvert JVF\rvert > 0.25$	$\lvert\eta\rvert < 2.4$, $\lvert JVF\rvert > 0.5$
JES:	14.6 %	11.9 %	10.6 %
JER:	12.4%	9.89 %	6.49 %
JVF:	0.92%	1. 16%	1.51%
Pileup:	0.74%	0.27%	0.19%
Muon:	1.05%	1.05%	1.05%
Muon Trigger:	4.00%	4.00%	4.00%
Electron:	0.7%	0.7%	0.7%
Electron Trigger:	1.6%	1.6%	1.6%
Statistics:	0.15%	0.17%	0.18%
Total:	19.6 %	16.1 %	13.2%

TABLE 6.7: Uncertainties on the total Z + 2 jets selection for three different combinations of the pseudorapidity region and the JVF cut, the applied p_T threshold is 25 GeV. The table shows that by constraining the pseudorapidity of the jets, and applying a strict JVF cut, both the JES and the JER can be largely reduced.

the p_T of the jets in the MC sample drops more rapidly than the jets in the data. Consequently, the uncertainties will be somewhat overestimated.

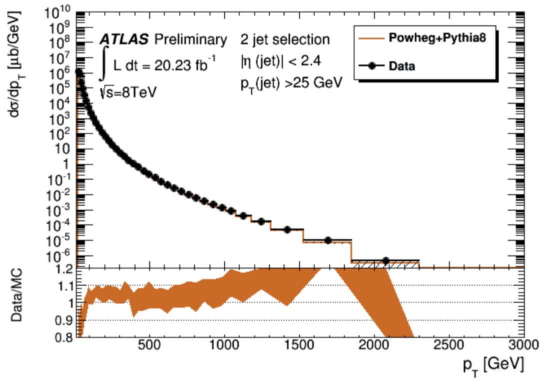

FIGURE 6.12: Comparison of the subleading jet momentum between the MC prediction and the data in the 2 jet category.

6.4.9 Summary

Finally, we summarise the estimations on the background event selections, the various signal samples and their uncertainties in table 6.8 for the 2 jets selection and in table 6.9 for the 0 jet selection. The conclusion that can be drawn from these tables, is that the $Z \rightarrow l^+l^-$ channel is very clean, with small background contributions. While statistical errors remain small for all samples, the systematic error is relatively large for the Z + 2 jets selection. For the Z + 0 jet selection, the systematic uncertainties are much smaller since there is only a cut on the hardest jet, which usually has a lower uncertainty than the second and third jets. In chapter 8 the uncertainties on the event selections will be propagated to the final results on f_{DPI} and σ_{eff}.

Background	Event estimation and uncertainty (syst+stat)	
	Muon channel	Electron channel
QCD	$650 \pm 54\%$	$2 \cdot 10^3 \pm 20\%$
$Z\tau\tau$	$56.1 \pm 47\%$	$36.0 \pm 138\%$
$t\bar{t}$	$3.35 \cdot 10^3 \pm 5.3\%$	$2.79 \cdot 10^3 \pm 5.0\%$
Di-Boson	$1.65 \cdot 10^3 \pm 7.6\%$	$1.3 \cdot 10^3 \pm 6.0\%$
Single Top	$237 \pm 8.2\%$	$238 \pm 8.6\%$
$Z \rightarrow l^+l^-$ (Alpgen+Pythia)	$2.83 \cdot 10^5 \pm 12\%$	$2.08 \cdot 10^5 \pm 12\%$
$Z \rightarrow l^+l^-$ (Sherpa)	$2.70 \cdot 10^5 \pm 15\%$	$2.16 \cdot 10^5 \pm 15\%$
$Z \rightarrow l^+l^-$ (Alpgen+Jimmy)	$2.72 \cdot 10^5 \pm 13.0\%$	$2.05 \cdot 10^5 \pm 13\%$
Data	$2.73 \cdot 10^5 \pm 0.2\%$	$2.16 \cdot 10^5 \pm 0.2\%$

TABLE 6.8: Summary of the background and signal event estimations and their errors for the 2-jet event selection.

Background	Event estimation and uncertainty (syst+stat)	
	Muon channel	Electron channel
QCD	$3.29 \cdot 10^4 \pm 69\%$	$5.84 \cdot 10^4 \pm 20\%$
$Z\tau\tau$	$1.66 \cdot 10^3 \pm 4.5\%$	$202.5 \pm 34\%$
$t\bar{t}$	$252 \pm 19\%$	$164 \pm 19\%$
Di-Boson	$2.4 \cdot 10^3 \pm 6.0\%$	$1756 \pm 5.3\%$
Single Top	$216 \pm 12\%$	$74.0 \pm 15\%$
$Z\mu\mu$ (Alpgen+Pythia)	$6.24 \cdot 10^6 \pm 4.6\%$	$4.50 \cdot 10^6 \pm 3.1\%$
$Z\mu\mu$ (Sherpa)	$7.36 \cdot 10^6 \pm 4.7\%$	$5.65 \cdot 10^6 \pm 3.2\%$
$Z\mu\mu$ (Alpgen+Jimmy)	$6.5 \cdot 10^6 \pm 4.7\%$	$4.60 \cdot 10^6 \pm 3.2\%$
Data	$6.88 \cdot 10^6 \pm 0.04\%$	$5.09 \cdot 10^6 \pm 0.04\%$

TABLE 6.9: Summary of the background and signal event estimations and their errors for the 0 jet event category.

Z+jets Monte Carlo Datasets

Introduction

In chapter 3 it was explained how proton-proton collisions can be simulated by using Monte Carlo techniques. In practice, these simulated datasets always suffer from limited statistics. Another restriction is that not for each generator there is an ATLAS detector-simulated dataset. In this chapter I will first give a summary of the available ATLAS Z+jets datasets. The second section of this chapter explains how DPI events are vetoed from one of these datasets to create a pure SPI Z + 2 jets background sample.

7.1 Z+jets Dataset Summary

It is illustrative to show a comparison of the number of jets and the p_T of the sub-leading jet for different samples of Z+jets events. There are four available ATLAS samples that are based on the following algorithms:

- A MEPS sample in which the matrix elements are calculated by Alpgen and Pythia6 for the parton shower. The merging is done by the MLM method.
- Alpgen+Herwig+Jimmy: A limited statistics sample, but with the advantage that MPI-partons can be traced in the event-record
- A MENLOPS sample with events calculated by the Sherpa1.4 computer program.

- A NLO+PS sample where the NLO Z+0jet matrix elements are calculated by the Powheg generator and further jet emissions are calculated by using the Pythia8 parton shower.

Figure 7.1 shows a comparison of the samples with Atlas data for the number of jets associated with the production of a Z boson. The upper plot shows all histograms, while the ratio plots show the comparisons with the individual samples with the data. These ratio plots include all experimental systematic uncertainties. While the Alpgen samples show a good resemblance for the jet-bins with 2-3 jets, the MENLOPS Sherpa agrees with the data where the number of jet is between 0 and 3 jets. The bottom ratio plot shows the comparison with the Powheg+Pythia8 sample. This sample does resemble the 0 and 1-jet cross sections very well, but heavily underestimates the jet rates for $Njets \geq 2$ (points not in the range of the ratio plot).

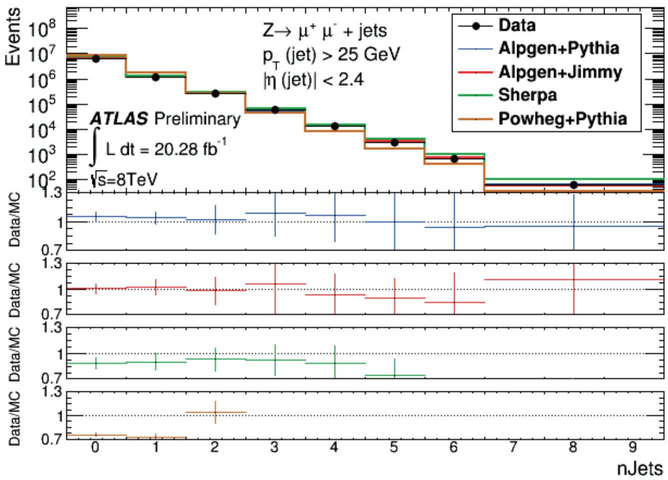

FIGURE 7.1: Comparison of the number of jets between a number of samples and the data. The plots show the performances of two MEPS samples, a MENLOPS sample and a NLOPS sample.

The same comparison can be made for the p_T of the leading jet and the sub-leading jets as in figures 7.2 and 7.3. Again it shows that the MEPS and the MENLOPS sample describe the momenta of the jets very well. This is in contrast to the Powheg+Pythia8 NLOPS sample which only performs moderately well in describing the leading jet distribution while the spectrum of the sub-leading jet is not well described. Since the Powheg program requires the leading jet to be matched to the ME-parton, the sub-leading jet is always modelled by the parton shower. Figures and 7.2 7.3 show that the transverse momenta of the jets in the Powheg+Pythia sample are not well modelled. Therefore it can be concluded that hard jet kinematics are not well modelled by a parton shower.

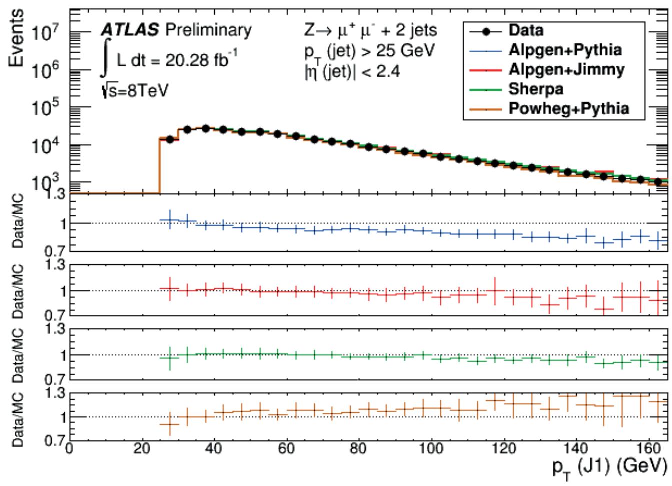

FIGURE 7.2: Comparison of the transverse momentum of the leading jet between the data and the MC samples.

7.2 MPI and SPI Topology

The following section evaluates a number of distributions that clearly separate DPI from SPI events. For this investigation both the SPI and DPI distributions are extracted from the MC sample. First I will present a list of variables that are especially sensitive to DPI effects. In section 7.3 I will explain how DPI events are vetoed from the Z+jets MC sample, in order to construct a clean SPI background sample of events. Finally, the separated

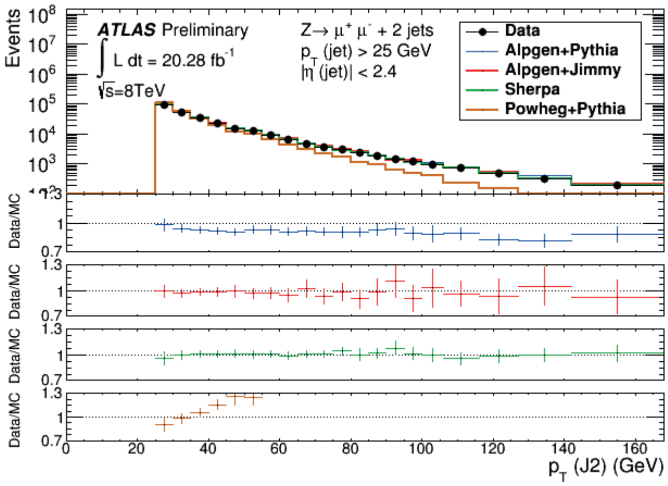

FIGURE 7.3: Comparison of the transverse momentum of the subleading jet between the data and the MC samples.

DPI and SPI samples are used to estimate signal over background ratios for the listed variables.

7.2.1 DPI Sensitive Variables

DPI jets can be modelled by regarding them as an independent QCD $2 \to 2$ interaction. As a consequence, the jets will typically have a lower p_T than jets in the SPI process, since they do not recoil against the heavy Z boson. The azimuthal angle between the jets will be close to π, because to first order there are no other particles balancing their momentum. The same reasoning holds for the Z boson system. The p_T of the Z will be lower for DPI events and the angle ϕ between the leptons from the Z decay will on average be larger. Finally, since the two systems should largely be independent, the azimuthal angle between the di-jet and the reconstructed Z should be flat for DPI events and peaking at π for SPI-events.

Summarising, there are the following variables that enable discrimination between DPI and SPI:

- Jet-balance:

$$\Delta_{jj} = \vec{p_{Tj1}} + \vec{p_{Tj2}}, \tag{7.1}$$

which is small for DPI events, as shown in figure 7.6.

- Normalised jet-balance:

$$\Delta^N_{jj} = \frac{\vec{p_{Tj1}} + \vec{p_{Tj2}}}{|\vec{p_{Tj1}}| + |\vec{p_{Tj2}}|}, \tag{7.2}$$

which peaks close to zero for DPI/back-to-back jets, as shown in figure 7.7.

- Angle between the jets in the transverse plane: $\Delta\phi(j, j)$, peaks near π for DPI and is more uniformly distributed for SPI.

- Normalised lepton-balance:

$$\Delta^N_{ll} = \frac{\vec{p_{Tl1}} + \vec{p_{Tl2}}}{|\vec{p_{Tl1}}| + |\vec{p_{Tl2}}|}, \tag{7.3}$$

which peaks towards zero for DPI/back-to-back leptons.

- Transverse momentum of the Z boson: $p_T(Z) = \vec{p_{Tl1}} + \vec{p_{Tl2}}$. Peaks towards small values for DPI.

- Azimuthal angle between the leptons: $\Delta\phi(l, l)$. Peaks near π for DPI, is more uniformly distributed for SPI.

- Azimuthal angle between the two systems: $\Delta\phi(Z, jj)$. Flat for DPI, while it peaks at π for SPI.

7.3 DPI Veto in Monte Carlo

In a search for DPI events, special care should be taken in defining the SPI background processes. We are using Z+jets MC samples that include both jets from the SPI process and from hard MPI. If we would like to use these Z+jets samples to model the SPI and soft MPI background of Z + 2 jets DPI events, we first need to strip the DPI events from them. To measure the DPI fraction in events with Z + 2 jets, it is important to have a clear idea on how DPI is modelled in event generators. In specific, the fraction of DPI events in Z + 2 jets events as modelled in MC-generators will be determined:

$$f_{DPI} = \frac{N_{DPI}}{N_{DPI} + N_{SPI}}. \tag{7.4}$$

In this section I will explain how this can be done, and use the results to show the event topology of DPI events.

The underlying event cannot be neglected as it significantly contributes to the energy of SPI jets. Instead, jets should be matched to MPI quarks and gluons. If it is determined that both jets in the event originate from MPI partons, the event is identified as a DPI event and it is vetoed. A simple algorithm will be set up that decides whether a jet originates from a MPI-parton, based on two kinematic variables:

$$\Delta R(jet, parton) < R_{cut} \tag{7.5}$$

$$p_T(parton) > p_T^{Max}, \tag{7.6}$$

where $\Delta R(i, j)$ is defined as:

$$\Delta R(i, j) = \sqrt{\Delta\eta(i, j)^2 + \Delta\phi(i, j)^2}, \tag{7.7}$$

$$\eta = -\ln\left(\tan\frac{\Theta}{2}\right). \tag{7.8}$$

η is called the pseudorapidity which approached the rapdity for low mass particles. The differences between rapidities and pseudorapidities are Lorentz invariant and are therefore preferred over the polar angles, Θ.

The challenge in this study is to optimize the two variables R_{cut} and p_T^{Max} to cut away DPI events as efficiently as possible, while not removing events with SPI jets from the sample. In this study jets are selected in the region $p_T > 25$ GeV, $|\eta| < 2.4$. very similar to how jets are to be defined in the analysis chapter 6.

Figure 7.4 shows a 2-dimensional histogram obtained from the Alpgen+Jimmy sample that contains both SPI and DPI events. The x-axis of the histogram gives the parton p_T and the y-axis gives the p_T of the jet that is matched with the parton in a cone with $R_{cut} = 1.0$. There are two main structures in this plot: the vertical line at parton $p_T \approx 5$ GeV and a diagonal line. From this histogram we learn that partons with a p_T lower than 15 GeV are largely uncorrelated with the jet p_T and the two selected jets likely comes from SPI. Cutting at $p_T^{Max} = 20$ GeV would leave all events with jets from SPI, but will also leave a fraction of the DPI events in the sample. p_T^{Max} and R_{cut} can however be further optimized by examining f_{DPI} for a range of values between 10 GeV $< p_T^{Max} <$ 20 GeV and $0.6 < R_{cut} < 1.2$.

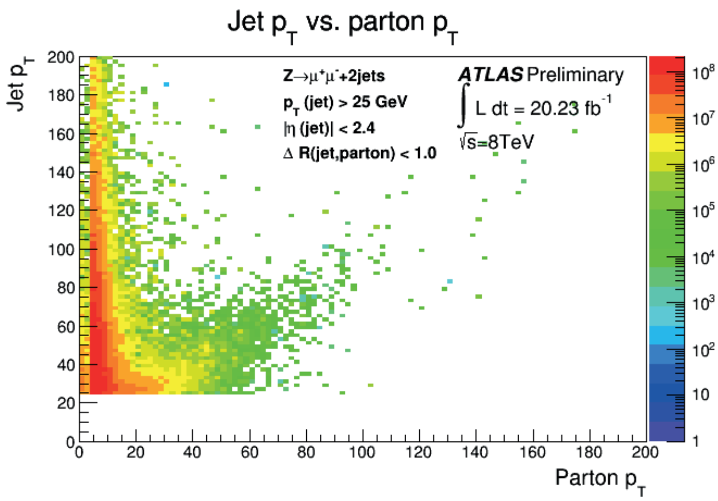

FIGURE 7.4: 2-dimensional histogram of the MPI particle p_T and the jet p_T that were matched in a cone with $R_{cut} = 1.0$. The vertical band of low p_T partons are uncorrelated to the reconstructed jets.

To determine the optimal values for p_T^{Max} and R_{cut}, the fraction of DPI events (f_{DPI}) is measured in the MC samples as a function of these two variables. f_{DPI} can be measured by performing a Maximum Likelihood (ML) fit with the SPI and DPI templates to the full MC sample.

The variable that is used to perform the fit is the normalised jet balance (eq. 7.2), which is shown in figure 7.7. A template for the DPI events can be extracted by assuming that the two hard parton-parton interactions are independent of each other and the two jets from the secondary scattering can very well be modelled by $2 \to 2$ QCD interactions. The shape of the DPI template can then be created by measuring it in 2-jet events. The fraction of DPI events in the Alpgen+Jimmy MC sample ($f_{DPI}(MC)$) can now be determined by fitting the DPI template, together with the SPI template (on which a DPI veto was applied) to the full Alpgen+Jmmy sample.

The exact statistical procedure for the fitting is explained in section 8.2 For now I will only show the results for the value of $f_{DPI}(MC)$. Figure 7.5 shows the result for a range of values for the R_{cut} and p_T^{Max} variables.

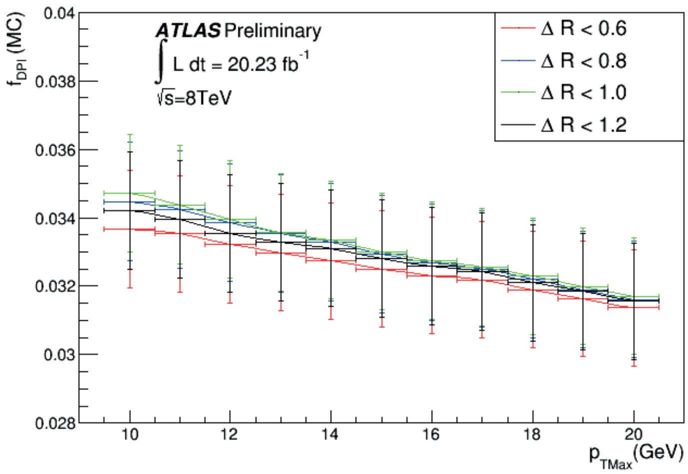

FIGURE 7.5: Fraction of DPI in the Alpgen+Jimmy sample, obtained by fitting a di-jet distribution together with the SPI-template corresponding to the given p_T^{Max} cut to the origininal distribution. The distribution that was used for this purpose is the normalised jet balance $\Delta_{jj}^N = \frac{\vec{p_T}_{j1}+\vec{p_T}_{j2}}{|\vec{p_T}_{j1}|+|\vec{p_T}_{j2}|}$.

The figure shows that the largest DPI-fraction is obtained by using a R_{cut} of 1.0. Moreover, increasing or decreasing R_{cut} hardly has any influence on the result. It is not only important to maximize f_{DPI}, but also to obtain a DPI sample that is not polluted by SPI events. If we would increase R_{cut}, more jets will be matched to partons and therefore more events will be marked as DPI and be vetoed from the SPI template. However, if the value for R_{cut} is increased, the fraction of DPI events drops. This phenomenon can be explained by the fact that events were falsely marked as DPI, i.e. they did not have a DPI topology and could not be explained by increasing $f_{DPI}(MC)$ in the fit. On the other hand, by decreasing the value of R_{cut}, less events are removed from the SPI that could otherwise have been compensated by a larger $f_{DPI}(MC)$. In other words, lower values than 1.0 result in a loss of efficiency in the DPI veto. The templates for R_{cut} values of 0.8 and 1.2 are used as a systematic uncertainty, even while this uncertainty is much smaller than the statistical uncertainty.

It is however somewhat more difficult to choose an appropriate value for p_T^{Max} as the DPI fraction is monotonically declining for increasing values of p_T^{Max}. Therefore it is not immediately clear which value should be chosen to create the SPI-template. To solve this issue, an interpolation is created between histograms with different p_T^{Max} values with an interpolation parameter α. α is then fitted to the Δ_{jj}^{N} distribution in the data to determine which shape of the SPI-template optimally describes the background. This study results in a p_T^{Max}-cut of 17 GeV, while an up- and down-variation of 2 GeV is used as a systematic uncertainty on this parameter.

7.3.1 DPI Distributions

Figures 7.6-7.9 show the DPI-over-SPI ratios for the suggested DPI sensitive variables listed above. In general, the DPI templates show sharper peaks in the distributions of the lepton variables than in the distributions of the jet variables. The first reason for this is that leptons loose less energy from final state radiation than jets. The second reason is that the invariant mass of the system is larger, which forces a large opening angle between the two leptons. Figure 7.9 shows that the DPI-over-SPI ratio for the azimuthal angle between the two systems is relatively large over a long range of $\Delta\phi(Z, jj)$. This might be a beneficial property to extract f_{DPI} in a ML-fit. A disadvantage of this distribution is that it is difficult to construct an independent data-driven template for the DPI events in this distribution and one will have to rely on the extracted DPI template from the DPI veto. The reason that a DPI template cannot be extracted from the data is that this variables relies on the connection between two processes, which is exactly what we are trying to measure. The lepton and jet variables can be extracted from measuring them in a "standalone" jet/Z production and vetoeing the other. This cannot be done for $\Delta\phi(Z, jj)$. In chapter 8 I will provide another assessment of these variables, taking into account all detector effects and uncertainties.

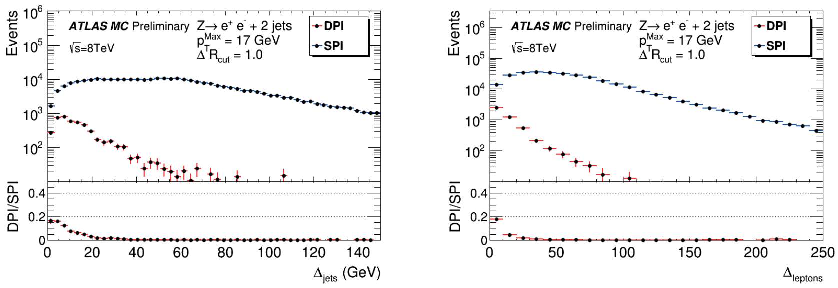

(A) Jet-balance (B) p_T of the Z boson

FIGURE 7.6: The balanced p_T of the jet and the Z boson systems. The balanced p_T declines more rapidly for DPI events and this is even more the case for the Z-system in comparison to the jet-system.

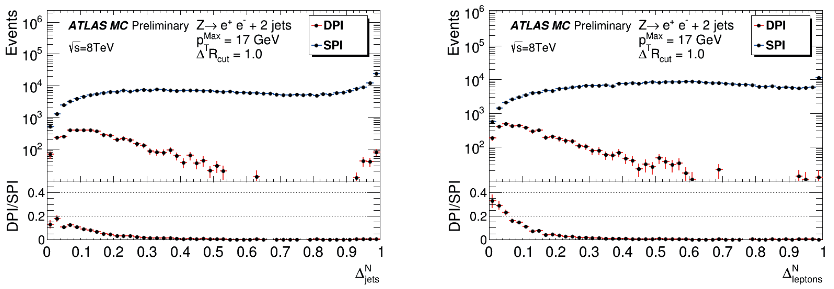

(A) Normalised jet-balance (B) Normalised lepton-balance

FIGURE 7.7: $\Delta^N_{jj/ll}$ for DPI and SPI events. The ratio for the lepton variables peaks much sharper than the jet variables.

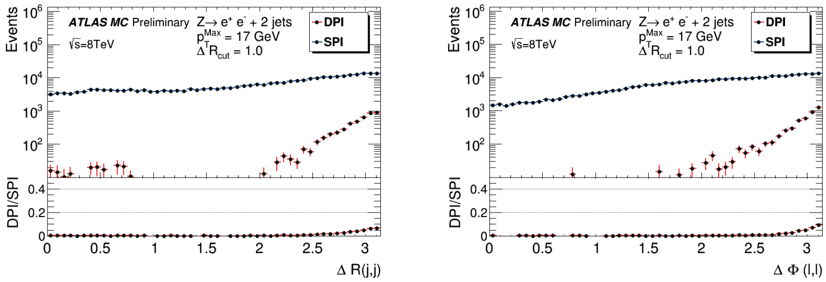

(A) Azimuthal angle between the jets. (B) Azimuthal angle between the leptons.

FIGURE 7.8: The azimuthal angles between the jets and between the leptons peaks towards π for DPI events. The ratios for the most sensitive bins are in the order of a factor 2 smaller than for the $\vec{p_T}$ dependent variables.

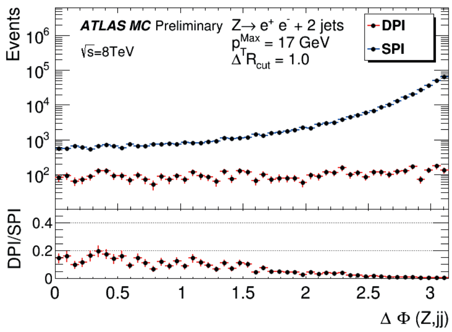

FIGURE 7.9: Azimuthal angle between the jet-system and the Z-system. Although the distribution shows a large DPI-over-SPI ratio for a large number of bins, the exact shape of the DPI distribution cannot be extracted from the data.

Extracting σ_{eff}

Introduction

The DPI measurements in the past until present were performed with 4 jets [6],[7],[8] W+2jets [9] and photon+3jets [78] in the final state. Their results were already summarised in figure 1.8. These channels were chosen mainly because of restrictions on the integrated luminosity. Since σ_{eff} is a large number in comparison to hard-scattering cross-sections, one can only probe DPI-processes of which the individual cross-sections are also large. At higher integrated luminosities, processes with somewhat smaller cross sections such as electroweak bosons production also become within reach.

One of the advantages of the large integrated luminosity of the ATLAS 2012 dataset for DPI measurement is that the Z + 2 jets final state becomes available for a σ_{eff} measurement. This channel is cleaner than previous measurements since it does not require the measurement of missing energy to reconstruct a W-boson, while there are only 2 jets in the final state. A disadvantage of the high luminosity of the current dataset is that effects from pile-up become more important and soft jets become unavailable for measurements.

The calculation of σ_{eff} needs three cross sections as an input. First, the calculation requires a measurement of the cross section of the Z + 2 jets events that come from DPI. This cross section is especially difficult to measure, since it suffers from very high background from ISR jets. The other inputs to the calculation are the separate cross sections for the exclusive Z+0jet production and the exclusive 2jets production, of which the first process does not suffer from any background and the second process only has a very small background as was summarised in chapter 6.

The general formula for a cross section is the following:

$$\sigma = \frac{N}{\epsilon A \mathcal{L}}. \tag{8.1}$$

Where N is the number of measured events, ϵ is the total efficiency of the measurement and A is the acceptancy of the measurement that extrapolates a fiducial measurement to the total theoretical cross section. Since we are interested in a ratio of cross sections, the efficiencies and acceptancies for measuring jets and leptons cancel in the ratio:

$$\begin{aligned}\sigma_{eff} &= \frac{\sigma_{Z+0j} \times \sigma_{2j}}{\sigma_{Z+2j(DPI)}} \\ &= \frac{N_{Z+0j}}{\epsilon_{2l} A_{2l} \mathcal{L}} \times \frac{N_{2j}}{\epsilon_{2j} A_{2j} \mathcal{L}_{2j}} / \frac{N_{Z+2jDPI}}{\epsilon_{2j}\epsilon_{2l} A_{2j} A_{2l} \mathcal{L}} \\ &= \frac{1}{f_{DPI}} \frac{N_{Z+0j}}{N_{Z+2j}} \frac{N_{2j}}{\mathcal{L}_{2j}}.\end{aligned} \tag{8.2}$$

Because the dijet measurement relies on highly prescaled triggers, the integrated luminosity used for the measurement of dijets is different from the full luminosity and the two do not cancel.

The total event yields for the Z + 2 jets and the Z+0jet selections were already summarised in chapter 6 and the uncertainties on these measurements will be assumed to be Gaussian distributed. This chapter therefore mainly focuses on measuring Z + 2 jets events from DPI through a profile likelihood fit. The channel of the Z boson decaying into muons already provides more than enough statistics for the fitting. However, the electron channel will be used as a parallel cross-check.

In section 8.1 I will discuss the discriminating variables as proposed in chapter 1 and this time also include experimental uncertainties in the discussion. In section 8.2 I will explain the statistical framework behind a profile likelihood fit and in section 8.3 the results from the fit will be discussed.

8.1 Fitting Variables

In chapter 3, the signal over background ratios at truth-level were already investigated for a set of seven variables. In this section I will first discuss the five distributions that were found to be the most sensitive to the DPI-signal, but this time the detector effects are included in the discussion. All sources of uncertainty as described in section 6.4 are included in the results discussed in this chapter. From the five selected variables, at least one should be chosen to be used for the f_{DPI} extraction. The following criteria can be listed that should be satisfied:

- The distribution of this variable in the data should be well described by the MC, both in the signal and background region
- A good shape distinction between the signal and background should be provided
- The uncertainties in the signal region should be small
- The extracted f_{DPI} should not depend on the fitting region

Figures 8.1-8.3 show all the SPI backgrounds compared to the data. DPI events are vetoed from the Alpgen+Jimmy sample by using the procedure that was explained in chapter 7.

The information that can be extracted from these plots is how large the uncertainty is in the DPI regions and whether the data is well described in the SPI region. In addition, we can already estimate the shape of the DPI events from the deficiency between the data and the background.

The two variables that depend on the lepton-variables ($p_T(Z)$ and Δ_{ll}^N) have the undesired property that the largest part of the systematic uncertainty is in the bins where we expect the DPI to be prominent (small p_T of the Z, low values for Δ_{ll}^N). Given the fact that the uncertainties are dominated on the jet measurement, these high uncertainties for events with low $p_T(Z)$ can be explained by the fact that the two jets in these events will also have a low p_T. Additionally, non-perturbative processes are of relative large influence to

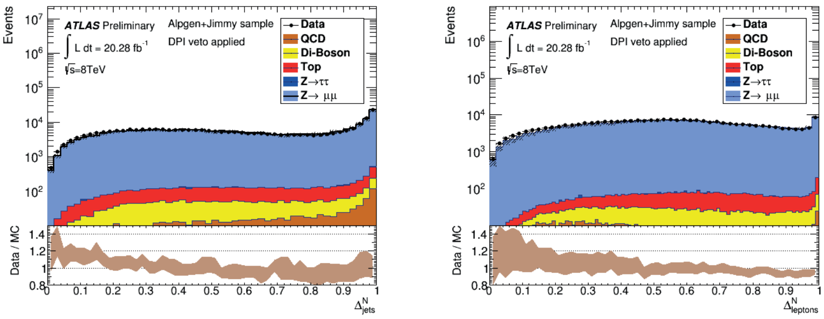

(A) Normalised jet-balance

(B) Normalised lepton-balance

FIGURE 8.1: Data/MC comparison for $\Delta^N_{jj/ll}$. Whereas the uncertainty for the normalised jet-balance is mainly in the higher bins, where the jets are collinear, the uncertainty is large for the lower bins in the normalised lepton balance.

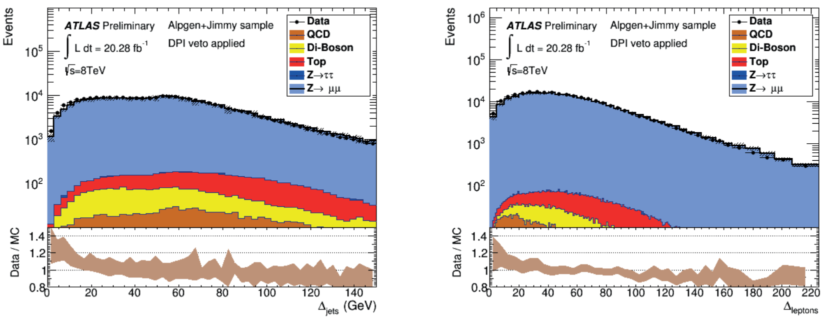

(A) Jet-balance

(B) Lepton-balance

FIGURE 8.2: Data/MC comparison for $\Delta_{jj/ll}$. Whereas the uncertainty for the normalised jet-balance is mainly in the higher bins, where the jets are collinear, the uncertainty is large for the lower bins in the lepton balance.

the shape of the distribution for low Z-p_T and therefore there is also a large theoretical uncertaincty in the (DPI) low Z-p_T region.

The problem that the systematic uncertainty is higher in the DPI-sensitive bins is to a lesser extent also true for the angle between the two systems $\Delta\Phi(Z, jj)$. Two additional shortcomings of this variable are that the data is

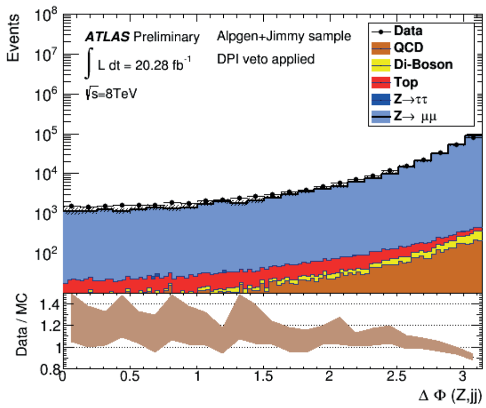

FIGURE 8.3: Data/MC comparison for $\Delta\phi(Z, jj)$. The uncertainties are somewhat larger in the DPI-sensitive area (the lower half of the histogram)

not well described in the SPI region (values close to *pi*) and that a data-driven DPI template cannot be extracted from the data.

The two jet dependent variables (Δ_{jj} and Δ^N_{jj}) are however more suitable. For these variables, the data distributions are reasonably well described by the MC model and the uncertainties are evenly distributed among the bins. However, since there is a small slope in the ratio between the data and MC for the jet-balance (Δ^N_{jj}), the fit region will influence the f_{DPI} extraction when using this distribution. Specifically, a larger fit range will increase the normalization on the SPI template in order to fit the data and by doing so, it decreases the DPI fraction.

From the given arguments, it is concluded that the best distribution for this purpose is the normalised jet-balance (Δ^N_{jj})).

8.2 Statistical Model

To determine the optimal number of DPI events in the dataset, a template fit with two templates will be applied. The first one is the DPI template and the second is the total SPI background. In general each of those templates should be normalised in such a way that they optimally match the data. For this purpose a test statistic $t(f_{DPI}, N_{evt}|\vec{x})$ is defined, where N_{evt} is the total number of estimated events in the measured data set and $\vec{x}$ is the actual binned space. This test statistic is a scalar number that measures how well the model fits the data, given the fitting parameters.

In addition to f_{DPI} and N_{evt}, there are also nuisance parameters (θ_i). These nuisance parameters are not of specific interest to the result, but are used to introduce the systematic uncertainties into the statistical model. The systematic uncertainies for each distributions are calculated by varying various uncertainty sources with a $\pm 1\sigma$ prescription and re-running the event selection. For each source of uncertainty, this procedure will result in three separate histograms: the nominal and the up/down variations. However, by interpolating (or extrapolating) these three histograms a continuous function of the expectation model and the test statistic can be constructed: $t(f_{DPI}, N_{evt}, \theta_i|x)$ In this thesis, a linear interpolation and a quadratic extrapolation are used, the nuisance parameters are used as an interpolation variable. The values ± 1 coincide with the $\pm\sigma$ variations and 0 coincides with the nominal distribution. This technique of incorporating the systematic uncertainties into statistical model is called profiling.

The variables will be optimized to fit the data by using a likelihood fit. The likelihood gives the chance that the model is true given a certain dataset and is a function of the model parameters. Each bin of the data histogram is Poissonian distributed and is independent of the uncertainty in other bins. Therefore the likelihood can be computed as the product of Poissonian distributed chances of all separate bins, multiplied by additional constraints on the likelihood. These additional constraints reflect prior knowledge of the likelihood.

For each systematic uncertainty source, an additional Gaussian constraint is added to the likelihood. The mean value of these Gaussian constraints are set to zero to reflect that the model is expected to be at the nominal value. The standard deviations of the systematic uncertainty constraints are set to unity to reflect that the prior uncertainties are $\pm 1\sigma$.

The statistical uncertainty in the MC background histogram is modelled by implying additional gaussian constraints on the likelihood. For these constraints, the mean of the Gaussian is set to the bin value and the standard deviation is set to the bin uncertainty. By doing this, an additional parameter Γ_i for each bin is introduced in the model. This way of modelling the statistical uncertainty in the model is called the Beeston-Barlow method [132].

For a Poissonian dataset with bin contents x_i, a model PDF M(f_{DPI},θ) and signal and background PDFs $S(\theta)$ and $B(\theta)$, the likelihood can be written as the following function:

$$\begin{aligned}\mathcal{L}(Nevt, f_{DPI}, \theta|x) = &\prod_{i=1}^{nbins} \frac{N_{evt} \cdot M_i^{x_i}}{x_i!} e^{-(M_i)} \\ &\cdot \frac{1}{2\sqrt{\pi}} e^{\frac{(\Gamma_i - M_i)^2}{2\Delta M_i}} \\ &\cdot \prod_{j=1}^{N_{NP}} \frac{1}{2\sqrt{\pi}} e^{\frac{\Theta_j^2}{2}}\end{aligned} \tag{8.3}$$

$$M(f_{DPI}, \theta) = f_{DPI} \cdot S(\theta) + (1 - f_{DPI}) \cdot B(\theta). \tag{8.4}$$

According the Neyman-Pearson lemma [133], the most powerful test statistic between two hypotheses is given by a ratio of the two likelihood. For the purpose of fitting, the denominator of this ratio is defined as the likelihood of the estimators, i.e. the optimal value of the variable. An estimator is denoted by adding a circumflex to the symbol: $\hat{f_{DPI}}$. The estimator denotes the value for f_{DPI} that maximizes the likelihood. Since the likelihood is a multidimensional function, the addition of a second circumflex denotes that the variable is estimated while assuming an arbitrary value for the other variables. The test statistic that will be used is the Profile Log-Likelihood (PLL) ratio and is written as:

$$t(\mu, \theta|x) = -2 \ln \frac{\mathcal{L}(x|\mu, \hat{\hat{\theta}})}{\mathcal{L}(x|\hat{\mu}, \hat{\theta})}. \tag{8.5}$$

According to Wilk's theorem [134], the uncertanties on the estimated variables can be extracted from this test statistic. The theorem states that minus two times the logarithm of the likilihood is asymptotically distributed as a χ^2 and therefore certainty limits can be derived from the following equation:

$$\chi^2 = \sqrt{2} \cdot Erf^{-1}(CL). \tag{8.6}$$

For example, for the 68.3% certainty limit (a 1σ deviation) on f_{DPI} can be found at the point where $t(f_{DPI}|x) = \sqrt{2} \cdot Erf^{-1}(0.683) = 1.0$.

8.2.1 Profile Likelihood

In the statistical formulation as provided above, the systematic uncertainties are incorporated in the statistical model. In this formulation one can define two states of knowledge for each systematic uncertainty, the prefit and the postfit uncertainty. The prefit uncertainty is calculated by evaluating the fit for the nominal distribution and for the input distributions for the $\pm 1\sigma$ prescriptions for that uncertainty. However, in a profile likelihood fit the nuisance parameters are fitted to the data and it can be that the uncertainties as a result of the fit are different from 1 for these uncertainties. As a consequence, the uncertainty on the parameter of interest (PoI) will also be proportionally different from the prior uncertainty. If there is indeed a significant difference between the prefit and postfit uncertainties, there should be a good physical explanation for this shift. The implementation of the model is done through the RooFit [135] package, which provides an interface to a large class of statistical tools. In the next section, the resuls will be presented and both the prior and posterior uncertainties will be calculated.

8.3 Results

8.3.1 Extracting f_{DPI}

f_{DPI} is extracted by optimising the model formulated in 8.3. The optimisation, including the error propagation is implemented in the RooFit package. The results are visualised in figure 8.4 and equation 8.7.

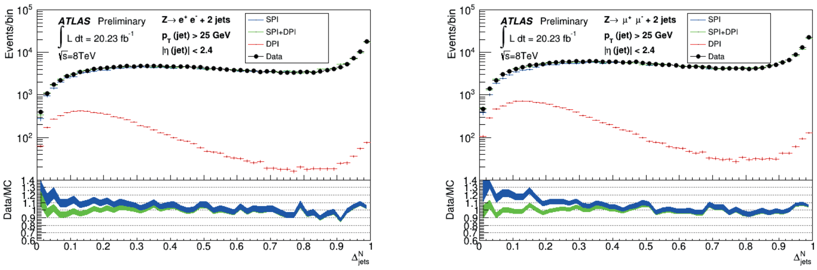

(A) Electron channel

(B) Muon channel

FIGURE 8.4: Result of the f_{DPI} fit for both the muon and electron channel. The green histograms show the total model, the blue histograms are the total SPI template, while the red histogram shows the DPI contribution in the Δ^N_{jj}. The ratio-plot shows the ratio of the measured data histogram over the total model in green and the ratio of the data over the SPI-only template in blue.

f_{DPI} measured from both the muon and electron channel, with total errors computed by using the profiling method are:

$$\boxed{\begin{aligned} f_{DPI}(\text{muon channel}) &= 4.15^{+.3}_{-.3}\% \qquad (8.7)\\ f_{DPI}(\text{electron channel}) &= 3.04^{+.3}_{-.3}.\% \qquad (8.8)\end{aligned}}$$

These values can be compared to the fraction of DPI events as determined in the Monte Carlo distributions, given in figure 7.5. The fraction of DPI events as measured in the muon channel is approximately 20 % larger than in the MC, while the fraction measured in the electron channel is approximately 10% smaller. Earlier measurements [9, 10] predict that the fraction of DPI events in Monte Carlo generators is underestimated. The result as obtained in the muon channel fulfills this expectation, whereas the electron channel does not.

The errors and the mean value of f_{DPI} are obtained from minimising the negative log-likelihood as shown in figure 8.5. The curves in this figure show the profile likelihoods (eq. 8.5) for the two channels. For each point on these graphs, all nuisance paramaters are optimised for a given value of f_{DPI}. The fact that they intersect at $-2 \cdot \frac{L}{L_0} \approx 2.5$ means that both values are shifted more than 2σ from the mean value of the two.

Although a small difference might be expected due to different efficiencies and acceptancies in both channels, 25% is not expected. σ_{eff} should however be independent of efficiencies and acceptancies and therefore be equal for the two channels. In section 8.3.2, it is explained how the effective cross section is calculated and shown that even for this variable, there is a difference between the channels.

At the end of this chapter, a section will be dedicated to discuss the origin of this difference.

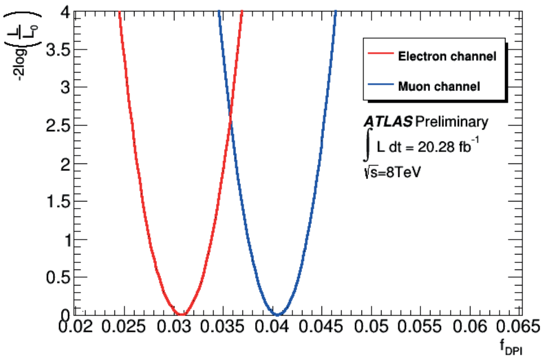

FIGURE 8.5: The profile likelihood as a function of f_{DPI} for the electron channel and the muon channel. For each point on the graphs, all the nuisance parameters are optimized to obtain the minimum profile likelihood.

Since the profile likelihood is a continuous function of all the nuisance parameters, it is not straightforward to break down the total error in different components. The influence of a single nuisance parameter on the total error can be computed as follows:

- Calculate the total error by incorporating all nuisance parameters in the fit
- Perform the fit again, but now setting one nuisance parameter as constant at the value obtained in the previous fit

- The influence of this parameter on the total error can be calculated by subracting the error obtained in the second step quadratically from the total error obtained in the first step

Each nuisance parameter has three properties that are of interest to the measurement:

- Its estimated mean value and uncertainty
- The prefit impact on f_{DPI}
- The postfit impact on f_{DPI}

Figure 8.6 shows a summary of these four properties for each nuisance parameter. The figure has two axes. The upper axis show the impact on f_{DPI} and the lower axis shows the mean value and error of the nuisance parameter in units of 1σ. For each axis, there are also two error bars plotted. The solid green error bar shows the prefit impact and the dashed blue error bar shows the postfit impact. For the lower axis, the red error bars have a value of zero, with a 1σ uncertainty. These red error bars therefore show the prefit estimators on the nuisance parameters. The black error bars show the postfit estimators, or the "pulls", of the nuisance parameters.

From figure 8.6 a number of interesting facts can be extracted. The first important point is that all nuisance parameters are largely overconstrained by factor of approximately 14. This phenomenon will be discussed in the next subsection.

Second, it is striking that the uncertainty on the jet energy resolution has by far the largest impact on the measurement. Third, the impact of quite a few parameters is asymmetric and of a large number of low-impact parameters the impact is even one-sided. Fourth, the mean value of the estimators of all the nuisance parameters are very close to zero. This phenomenon is explained by the fact that the statistical uncertainty on the background template is large. Therefore the discrepancy between the model and the data are corrected by shifting the Beeston-Barlow parameters in such a way that the total model coincides with the data histogram. The estimators on the Beeston-Barlow parameters are shown in figure 8.7. The figure shows that quite a few bin

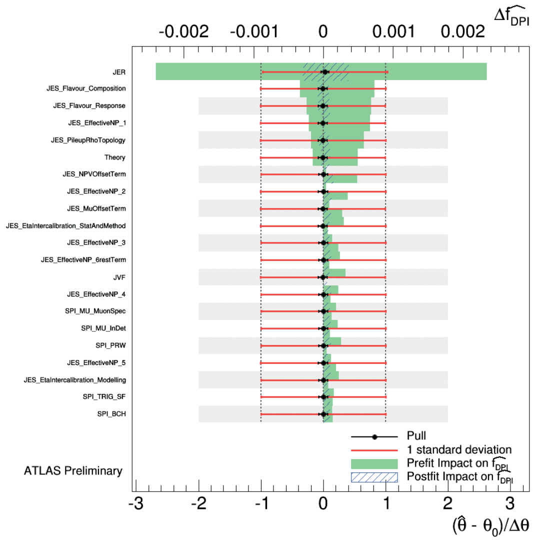

FIGURE 8.6: A summary of the properties for all nuisance parameters in the model.

values are pulled beyond a 1σ certainty limit, which indicates that the values of the Beeston-Barlow parameters compensate for deficiencies in the background model.

The correlation matrix also gives an important visualisation of the statistical model, which is split in figures 8.8 and 8.9. The first figure (fig. 8.8) shows the correlations of the parameters of interest with the Beeston-Barlow nuisance parameters and the second (fig. 8.9) show the correlation of the parameters of interest with the nuisance parameters corresponding to the systematic uncertainties. These figures show that the largest anticorrelation of f_{DPI} is with the Beeston-Barlow parameters belonging to the second bin until approximately the eleventh bin. This is expected since an increase in the expected number of background events in these bins would decrease the estimated number of DPI events. On the other hand f_{DPI} correlates with the expected number of background events in bins 24-34. This correlation is caused by the fact that a higher expected value in these bins are compensated by a lower normalisation on the SPI-template to fit the data. The

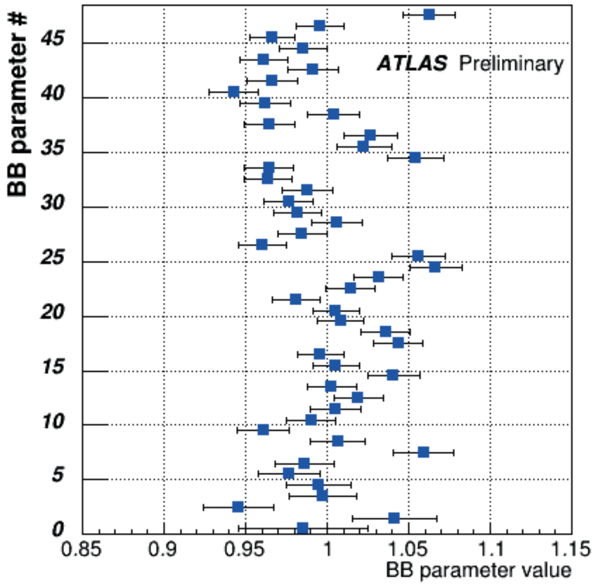

FIGURE 8.7: A summary of the Beeston-Barlow parameters. These parameters the statistical uncertainty for each background template bin and their corresponding fitted shift from their nominal value.

SPI template is normalised by $(1 - f_{DPI})$, which means higher values for the Beeston-Barlow parameters in bins 24-34 cause a higher f_{DPI}. It should also be noticed that the correlation between f_{DPI} and the nuisance parameters for the systematic uncertainties are close to zero. This means the nuisance parameters only have a minor influence on $\hat{f_{DPI}}$.

8.3.1.1 Overconstraining of the NPs

Overconstraining can be caused by either an incorrect formulation of the input uncertainties or by an underlying physics-driven constraint in the measurement. All prescribed experimental uncertainties have been supplied as an input to this fit. The theoretical uncertainty has been simplified by taking it as the difference between the Alpgen & Pythia generators on the one hand and the Sherpa generator on the other hand. However, since the theoretical uncertainty is known to be a minor uncertainty in this topology [9, 10], it

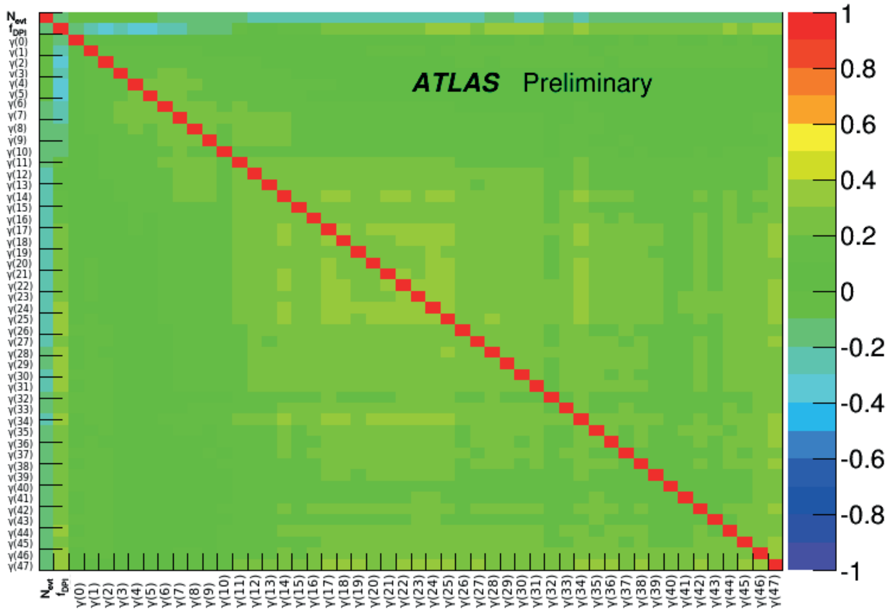

FIGURE 8.8: Correlation histogram of the fitting model, f_{DPI} and N_{evt} are the free parameters in the model and the $\gamma(*)$ are the Beeston-Barlow nuisance parameters of the SPI template.

is not expected that this simplification is the cause of overconstraining the nuisance parameters. From the kinematics in the measurement there is an additional constraint. The normalised balance of the two jets is measured and the main reason of an imbalance between the two jets is the p_T of the Z boson. The momentum of the leptons is however measured very precisely and therefore a strong constraint is forced on the uncertainty of the normalised jet balance. The argument of the physical constraint may explain the large reduction in the postfit uncertainty. Table 8.1 shows the uncertainties as computed with three different methods. The first column shows the uncertainties as computed in the classical method, i.e. all up and down variations are fitted separately and their differences w.r.t. the nominal fit are added quadratically. The second column shows the uncertainties as computed with a profile likelihood, but with the prefit uncertainties on the nuisance parameters applied. In the quoted uncertainties in the third column full use of the profiling method

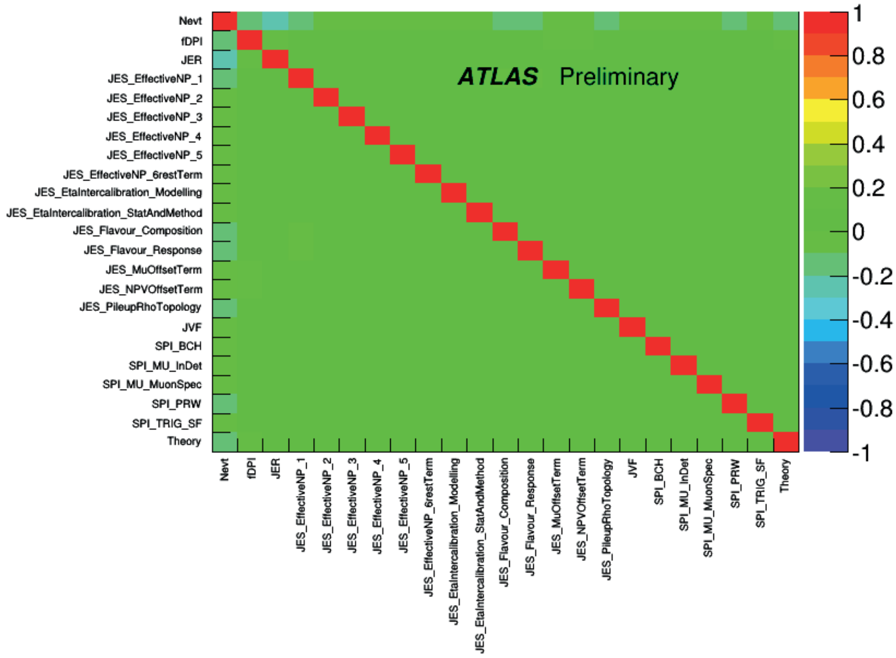

FIGURE 8.9: Correlation histogram of the fitting model, f_{DPI} and N_{evt} are the free parameters in the model and the other parameters are the nuisance parameters coming from the systematic uncertainties.

has been made and the postfit, or constrained, uncertainties on the nuisance parameters were applied. From the comparison of the prefit and postfit uncertainties, it can be concluded that the effect of the overconstraing largely reduces the systematic uncertainties. Since the statistical uncertainty in the MC is of equivalent size, the influence of the overconstraing on the total uncertainty is only 2.5%. However, compared to the case in which no profiling is applied, a large reduction in the uncertainty is achieved.

8.3.2 Calculating σ_{eff}

The measurement of f_{DPI} is the last unknown variable in calculation of σ_{eff} as calculated with equation 8.2. A summary of the results for both channels and the resulting σ_{eff} is shown in table 8.2.

	No profiling	Prefit	Postfit
JES	11 %	2.5 %	0.6 %
JER	15 %	5.8 %	1.5 %
JVF	1 %	< 0.1 %	< 0.1%
Muon	0.2 %	0.19 %	0.15 %
Trigger	0.2 %	< 0.1 %	< 0.1 %
BCH	< 0.1	< 0.1 %	< 0.1 %
PRW	< 0.1 %	< 0.1 %	
Total systematics	19 %	6.6 %	1.2 %
MC statistics	6.1	6.1 %	6.1 %
Data statistics	3.6 %	3.6 %	3.6 %
Total	20.2 %	9.7 %	7.2 %

TABLE 8.1: categorised prefit and postfit errors on f_{DPI}

.

	Electron channel	Muon channel
N_{Z+2jet}	$2.13 \cdot 10^5$	$2.73 \cdot 10^5$
N_{Z+0jet}	$5.13 \cdot 10^6$	$6.88 \cdot 10^6$
σ_{2j}	$2.49 \cdot \mu b$	$2.49 \cdot \mu b$
f_{DPI}	0.030	0.041
σ_{eff}	19.9 ± 2.0 mb	15.6 ± 1.3 mb

TABLE 8.2: Summary of the calculation of σ_{eff}

Whereas the result of the muon channel is very similar to the result previously measured by the ATLAS, D0 and CDF collaborations as shown in figure 2.3, the electron channel gives a somewhat higher value and is closer to the value as extracted by the CMS collaboration in the W+2jet channel. The uncertainty on the previous measurements of σ_{eff} are however considerably larger as these measurements did not apply a profile likelihood method. In the next section this discrepancy will be further investigated.

The quoted uncertainty on σ_{eff} in table 8.2 is the postfit uncertainty. In equation 8.2, all the variables depend on a subset of the nuisance parameters used in the extraction of f_{DPI}. As a consequence, the postfit systematic uncertainty on σ_{eff} is again largely reduced and can be neglected. The dominating postfit uncertainties are the data statistics and the MC statistics. These uncertainties are propagated through the likelihood by the RooFit package.

The uncertainties on the separate variables were already computed in chapter 6. However, since the input variables N_{Z+0jet},N_{Z+2jet},σ_{2jet} and f_{DPI} depend on the same systematic uncertainties, the uncertainty on σ_{eff} is much smaller than when assuming an uncorrelated hypothesis.

A breakdown of the uncertainty on σ_{eff} was performed and found to be nearly equal to the breakdown of the uncertainties on f_{DPI} as shown in table 8.1.

8.3.3 Electron-muon Discrepancy

Both the results on f_{DPI} and σ_{eff} suffer from a large difference between the electron and the muon channel. Due to small differences in the acceptance and efficiency between electrons and muons, a small difference in f_{DPI} is expected between the two channels. However, σ_{eff} is independent of efficiency and acceptance of the detector as is shown in equation 8.2.

To determine the cause of this difference, a number of cross-checks was performed:

- Several control plots are produced for both channels and shown below.
- The cut on lepton momentum was varied and the discrepancy was shown to be insensitive to this cut.
- The cut on $\Delta(l, j)$ was varied and the discrepancy was shown to be insensitive to this cut.
- The jet-threshold was increased and the discrepancy was shown to be sensitive to this threshold.
- It was verified that the W+jets and photon-induced processes are a negligible background to the signal process.
- A cutflow comparison was performed for the electron channel and no differences between analyses were found.
- Unfolded distributions are compared, this is shown in detail in chapter 9.

8.3.3.1 Control Plots

As a first cross-check, data-MC comparisons for three distributions are presented for both channels. The p_T of the leading lepton is shown in figure 8.10, the mass spectrum of the Z boson is shown in figure 8.11 and the normalised jet balance is shown in figure 8.12. By investigating how well these distributions are described by the MC, it can be established whether both electron and muon channel gives a good description of the Z + 2 jets phase space. The leading lepton distribution shows that although the data are overestimated for small p_T in the muon channel, the peak region (25-60 GeV) of the distribution is very well described. This is not true for the electron case, where the the data over MC ratio clearly shows a shape difference in the peak region.

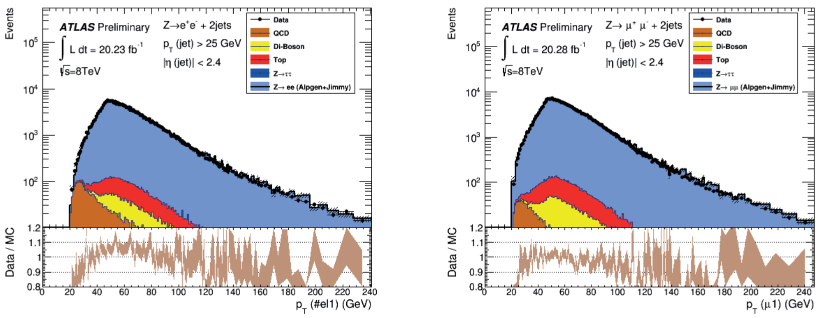

(A) Electron channel (B) Muon channel

FIGURE 8.10: Data-MC comparison for the p_T of the leading electron (left) and leading muon (right). The description of the peak region (25-60 GeV) is better for muon channel than for electron channel.

The Z boson mass spectrum is again much better described in the muon channel. For electrons, there is a large underestimation of the data in the regions 75-85 GeV and 100-110 GeV.

The next pair of plots show the normalised jet balance. These plots show that the data-MC ratio is larger over the full range of the distribution, except for the region where DPI has the largest contribution (0-0.2). Although this is only a difference of a few percent, it causes a 25% difference in the fraction of estimated DPI events in the selection. The control plots demonstrate that the

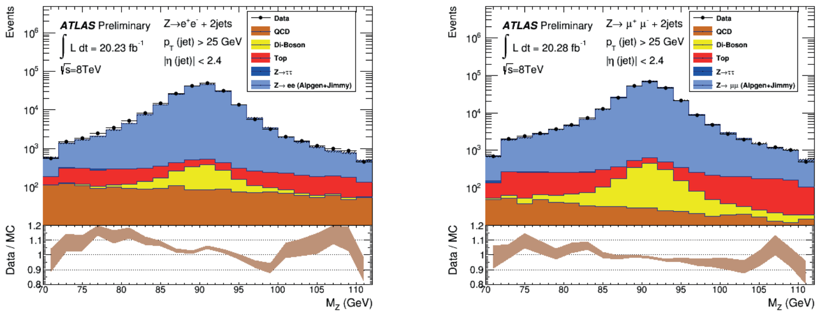

(A) Electron channel (B) Muon channel

FIGURE 8.11: Data-MC comparison for the Z boson mass spectrum for the electron channel and muon channel. The electron channel suffers from a faulty GEANT desription of the ATLAS detector and the MC has large deviations from the data in the regions 75-95 GeV and 100-110 GeV.

difference in the result between the electron channel and the muon channel is very likely to be due to a wrong description of the data in the electron channel. After completion of the analyses, it was demonstrated that the GEANT description for electrons in the ATLAS detector was not correctly implemented. For this reason, only the result obtained in the muon channel will be trusted and quoted as the official result of this thesis.

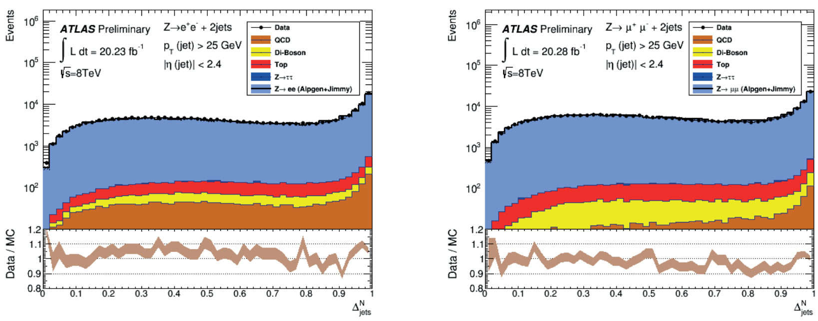

(A) Electron channel (B) Muon channel

FIGURE 8.12: Data-MC comparison for the normalised jet balance for the electron channel and muon channel. The ratio between the data and MC is larger everywhere in the electron channel compared to the muon channel, except for the DPI-sensitive region below 0.2.

8.4 Conclusions

By measuring DPI events in the Z + 2 jets channel a new process is added to the list of effective cross section measurements. The fraction of DPI events in Z + 2 jets events is measured to be $f_{DPI}(\text{muon channel}) = 4.15^{+.3}_{-.3}\%$ in the muon channel, while in the electron channel a different result is obtained: $f_{DPI}(\text{electron channel}) = 3.04^{+.3}_{-.3}\%$. A small difference between the result on f_{DPI} could be explained by differences in efficiency and acceptance between muon and electron detection. The cross section should however not be affected by these factors. Nevertheless, it yields a similar discrepancy: $\sigma_{eff}(\text{muon}) = 15.6 \pm 1.3$ mb, against $\sigma_{eff}(\text{electron}) = 19.9 \pm 2$ mb.

By comparing control plots in the two channels, it can safely be acknowledged that the difference is likely to originate from a fault in the electron channel. The version of the detector simulation that was used to simulate the electron events is today known to produce a deficiency in the shape of the Z boson mass, which is reproduced in this analysis. Since there was no Z + 2 jets MC dataset available at the time of this analysis, no definite prove can be given. Nonetheless, the conclusion is that the result in the muon channel is more solid than the result in the electron channel and is therefore established as the official result of this analysis.

Another important conclusion from this analysis is that the systematic uncertainties can be greatly reduced by applying a profile likelihood w.r.t. using the classical method of propagating by adding all errors quadratically.

Further improvement can be achievend by using a larger Z+jets background MC dataset. The systematic uncertainty is dominated by the statistical uncertainty on the background template. In addition, there are no supporting datasets available with which the theoretical uncertainty on the Alpgen+Herwig+Jimmy MC dataset can be estimated. Although this latter uncertainty is not expected to be large, a thorough evaluation of the theoretical uncertainties should improve the error estimation.

A larger MC dataset background events will open up the possibility of slicing the dataset in different bins of (for example) $p_T(j1)$ or $\eta(jj)$ and the effective cross section can then be derived for each slice. With such a method, the dependence of the effective cross section on various kinematic variables can be tested. Measuring such a dependence will be a precursor for the next step: testing correlations between the two partonic interactions.

Unfolding

Introduction

As a last step in the analysis, I will explain how the data is "unfolded" and how the analysis is repeated with the unfolded data. Unfolding is a technique with which measured data can be transformed to a distribution at truth level. In other words: unfolding is a transformation that attempts at inverting the detector effects. An advantage of unfolding is that it makes the measurement independent of the detector and can therefore be compared to distributions measured by other collaborations and phenomenologists can use the results to test new models. In this chapter I will first explain the Bayesian unfolding method, then in the next section show the details of the efficiencies and fake events in the two reference samples, and finally in the last section I will explain how the analysis is performed on the unfolded data.

9.1 Iterative Bayesian Unfolding

In a simplified model, unfolding can be regarded as a deterministic problem. A detector simulation can be modelled as a matrix multiplication: $\mathbf{R} = \mathbf{DT}$. Where the $\mathbf{R}$ and $\mathbf{T}$ represent vectors of the bin contents of the detector reconstructed (reco) and truth histograms and $\mathbf{D}$ is the matrix that represents the detector. The obvious way of obtaining a truth histogram as a function of the reco histogram would be inverting the D-matrix and multiplying it by the reco histogram. This method however fails and results in heavily varying bin contents as is showed and explained in [136] and [137]. The fundamental reason that the method fails is that finding $\mathbf{T}$ should be treated as a statistical problem instead of a deterministic. From a statistical perspective the problem can be stated as estimating the chances $P(\mu_i|\nu_j)$: the chance of a entry in a truth histogram bin i, given a entry in a reco histogram bin j. The detector simulation can be used to derive the relation in the other direction: $P(\nu_j|\mu_i)$: the chance of a entry in a reco histogram bin j, given a entry in a truth histogram bin i. The relation between $P(\mu_i|\nu_j)$ and $P(\nu_j|\mu_i)$ is given by the Bayes' theorem [138]:

$$P(\mu_i|\nu_j) = \frac{P(\nu_j|\mu_i) \cdot P(\mu_i)}{\sum_i P(\nu_j|\mu_i) \cdot P(\mu_i)}. \tag{9.1}$$

The formula introduces a prior estimation on the truth $P(\mu_i)$ and a normalisation that represents $P(\nu_j)$, the total chance of an event in the reco histogram bin j. In a simplified detector model the chances $P(\nu_j|\mu_i)$ represent the resolution function or the smearing matrix, the chances are written as λ_{ji}. $P(\mu_i|\nu_j)$, which is *not* the inverted smearing matrix, is written as θ_{ji}. λ_{ji} can be taken from detector simulated data by filling a 2-dimensional histogram with truth values on the one axis and the reco values on the other. It should be noted that this matrix holds rows and columns for all histogram bins, and additionally holds another row and column for all fake events (events that passed the selection on reco level while failing it at truth level), and misreconstructed events (events passing the truth selection, while failing the reco selection). θij can be calculated from equation 9.1. The only missing variable that is needed is the prior, which is chosen to be flat (all bins equally likely). This spectrum will almost never resemble a real physical spectrum and it will bias the final result. However, this is the case for all spectra and the influence of the prior can largely be reduced by iterating the procedure a few times. In this iteration, the output unfolded spectrum is used as an input prior to the next iteration. Usually, the distribution already converges after two or three iterations. Iterating much more often results in large irregularities as the output will approach the result from the deterministic approach.

The bin contents of the unfolded histogram can now be obtained by using the θ_{ij} matrix:

$$x(C_i) \approx \frac{1}{\epsilon_i}\theta_{ij} \cdot x(E_j). \tag{9.2}$$

$x(C_i)$ denotes the content of the cause bin i, where cause is a more general term that in this case is the MC truth histogram. $x(E_j)$ denotes the content of the effect bin j, where effect is a more general term for the detector simulation histogram. The efficiencies can be calculated by normalising the histogram of events that were matched to a reco event with the total truth distribution. Remember that the mis-reconstructed events are already stored in an extra column of the λ-matrix. The efficiencies can be calculated from the additional column by: $\epsilon_i = 1 - \lambda_{n_E+1,i}$, which gives the last ingredient to calculated an unfolded distribution.

9.2 Unfolding Z + 2 jets Distributions

9.2.1 1-Dimensional Case

The response matrix for the Z + 2 jets selection is derived by requiring that the event passes the selection at truth and at reco level, and additionally, the two jets should also be matched by requiring both jets at reco level to be within a range of $\Delta R < 0.4$ within the truth jets. By using this additional requirement, the influence of pileup jets at reco level can be further reduced. The fiducial phase space for the truth selection is very close to the selection at reco level:

- Leptons are dressed by photons not coming from the GEANT simulation in a cone of $\Delta R < 0.2$
- $p_T(Lepton) > 20GeV$
- $|\eta(Lepton)| < 2.5$
- Jets are reconstructed by a anti-k_T algorithm with R = 0.4, jets in the vicinity of a lepton ($\Delta R(j,l) < 0.4$) are removed.

- $p_T(Jet) > 25GeV$
- $|\eta(Jet)| < 2.4$
- Exactly 2 jets and 2 leptons are required in the event

Since the resolution of the transverse momentum of the jet is the dominant uncertainty in the measurement, it is interesting to look at the fake fraction and the efficiency in figure 9.1 close to the jet p_T threshold.

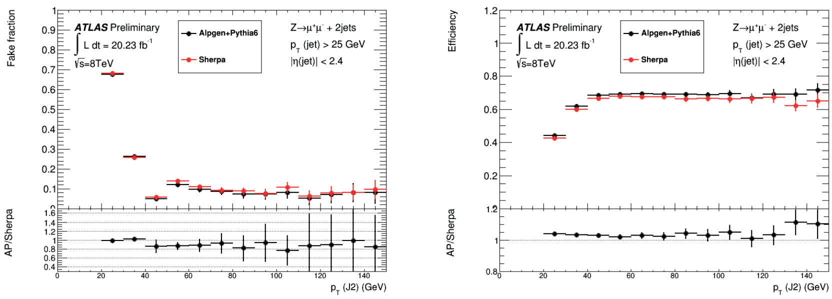

(A) Subleading jet fake fraction

(B) Subleading jet efficiency

FIGURE 9.1: Fake fraction and efficiencies for the subleading jet. The bins below 50 GeV show a higher fake fraction and lower efficiency, due to the JVF cut applied. The figures show very high fakes and low efficiencies for events with a subleading jet near the p_T threshold. This problem can partly be fixed by employing a 3-dimensional unfolding method.

The figures especially shows that the fake fraction is indeed very high near the jet p_T threshold. Part of the problem is that there are many events where the jets are just above the threshold at reco level, but the truth jets are just below the threshold. Even if the jets in the reco event can be matched to the events in the truth event, the match will not be included in the response matrix due to the fact that the truth event does not pass the selection criteria. A solution that can be proposed to this problem is to lower the threshold of the jets and include the p_T of subleading and subsubleading jets (2nd and 3rd jets) on two additional Y- and Z-axes of the histogram: $(\Delta^N_{jj}, p_T(J2), p_T(J3))$. If that 3-dimensional histogram is then unfolded, the bins in which the subleading jet is above the required threshold and the third jet is below the threshold can be selected and the low p_T jets will have a smaller fake fraction. The improvement of the efficiency and fake fraction can be tested by lowering the jet threshold to 20 GeV and project the bins that select events with a jet threshold of 25 GeV. These histograms are shown in 9.2.

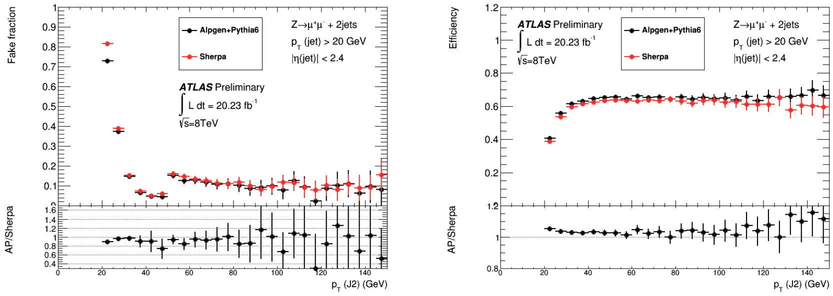

(A) Subleading jet fake fraction

(B) Subleading jet efficiency

FIGURE 9.2: Fake fraction and efficiencies for the subleading jet with a p_T threshold of 20 GeV. It shows that events with a subleading jet with a p_T above 25 GeV have lower fakes and higher efficiencies if the reco jets are allowed to be matched to truth jets below the jet threshold.

9.2.2 3-dimensional Case

The algorithm for 3-dimensional unfolding is in principle the same as for 1-dimensional unfolding, there are just more bins. Since Bayesion unfolding has a complexity of $\propto i \cdot N^3$ (with i, the number of iterations, and N the number of truth/reco bins), the number of bins should be restricted. Another issue that constrains the number of bins is the limited statistics in the MC sample. For these reasons, only 2 bins will be used for the y,z-axes: one bin above the jet threshold and one bin below the jet threshold. The x-axis will still have 50 bins, just as with the analysis at detector reconstruction level. By using 3-dimensional unfolding another complication is introduced. It can happen that the leading jet at truth level is reconstructed in de detector with a lower p_T than it actually has, or oppositely: a low p_T jet is reconstructed with a higher momentum. In these situations, the ordering of the jets could be swapped. For example, the response matrix could be filled in which the 3rd jet is above the jet threshold and the 2nd jet is below the threshold. This effect will also happen in the real detector, it is however not possible to measure how often this happens and in which events this was the case. To overcome this effect, MC events are required to have the same ordering at truth level as on reco level. Events that do not pass this requirement are added to the inefficiency bin of the response matrix.

The response matrix and the fake and efficiency rates for the normalised jet balance in the 3-dimensional case are presented below. Since the rates are represented in a 3-dimensional histogram, while the response matrix is now 6-dimensional (3 reco dimensions mapped to 3 truth dimensions), a transformation is applied to visualise the 3 dimensions as a single dimension:

$$Bin_{1D} = i + nx \times (j + ny \times k) + 1. \tag{9.3}$$

The equation maps bin number (i,j,k) with respectively (nx,ny,nz) number of bins to a single 1-dimensional bin number. For our histogram, this gives the following cases:

- bin number 1-50: projection on the x-axis for the (y,z)-bin in which $2^{nd}jet - p_T < 25, 3^{rd}jet - p_T < 25$
- bin number 51-100: projection on the x-axis for the (y,z)-bin in which $2^{nd}jet - p_T > 25, 3^{rd}jet - p_T < 25$
- bin number 101-150: projection on the x-axis for the (y,z)-bin in which $2^{nd}jet - p_T < 25, 3^{rd}jet - p_T > 25$ (never occurs)
- bin number 151-200: projection on the x-axis for the (y,z)-bin in which $2^{nd}jet - p_T > 25, 3^{rd}jet - p_T > 25$

The comparison between the Alpgen+Pythia6 and the Sherpa samples for the inefficiencies and the fake rates are show in figure 9.3. The response matrix is only shown as it was produced with the Alpgen+Pythia6 sample in figure 9.4

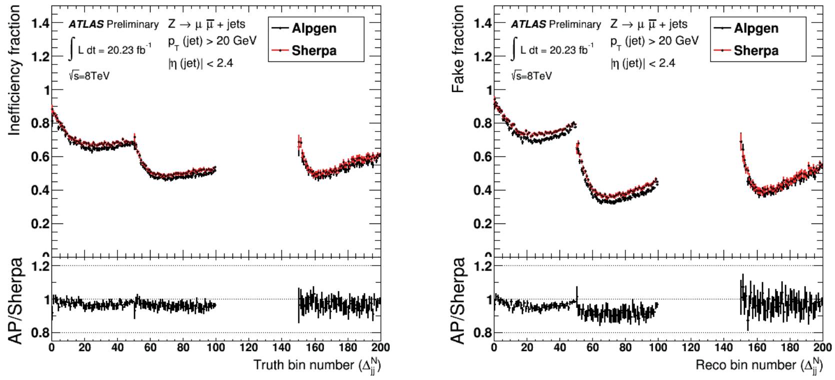

(A) Inefficiencies for the 3-dimensional Δ^N_{jj}-histogram

(B) Fake rate for the 3-dimensional Δ^N_{jj}-histogram

FIGURE 9.3: Comparisons between the two different reference sample for the inefficiencies and the fake rates of the Δ^N_{jj} histogram. The bins for the second and third dimension of the histogram are projected on additional bins on the x-axis. The histograms show that the Alpgen+Pythia6 sample gives a somewhat higher efficiency ($\approx$ 5%) than the Sherpa sample and also a slightly higher fake ratio (up to ($\approx$ 10%).

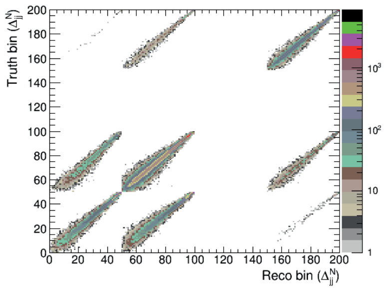

FIGURE 9.4: Response matrix for the 3-dimensional Δ^N_{jj} histogram as made with the Alpgen+Pythia6 sample. The bins for the second and third dimension of the histograms are projected on additional bins on the axis of the first dimension (x-axis in the original histogram). The matrix shows the possibility that a truth event on the y-axis migrates to a reco bin on the x-axis.

9.2.3 Unfolding Tests

A series of tests are be performed to examine the performance of the unfolding algorithm. In a first test the MC reco histogram is unfolded with the response matrix that was produced with the same MC sample. If this procedure results in exactly the MC truth histogram the test passes. Such a test is called a closure test and it was acknowledged that the applied unfolding procedure passes the test. Another type of closure test is to use half of the MC sample to train the response matrix, and use the other half of the MC sample as an input to the unfolding procedure. These tests are shown in figure 9.5. The next step is to check how the unfolding with Alpgen+Pythia6 sample differs from unfolding with the Sherpa sample, this is showed for the unfolding of the normalised jet balance in figure 9.6. A last check that is performed is the comparison between the results that is obtained by using the 3D unfolding procedure, with the results obtained by using the 1D unfolding procedure as shown in figure 9.7.

These tests and checks consistently show that the unfolding works well for the Δ^N_{jj} variable for a large range. However, there are significant shape variations between the several ways of unfolding for low values ($\Delta^N_{jj} < 0.05$) of this distribution and for large values ($\Delta^N_{jj} > 0.9$). In the next section, the results of the fitting procedure for the unfolded distributions is summarised. The problematic region will be excluded from the fit to minimize the uncertainty due to the unfolding procedure.

9.3 Results from the Unfolded Distributions

From the procedure as explained in the previous section, f_{DPI} and σ_{eff} can be extracted in a similar way as was done in chapter five. There are however a few differences:

- Instead of the reconstructed data, the unfolded data is used
- The truth MC distribution is used to model the Z + 2 jets SPI background instead of the detector simulated sample.
- A bin-by-bin unfolded distribution is used to model the truth level dijet signal template.

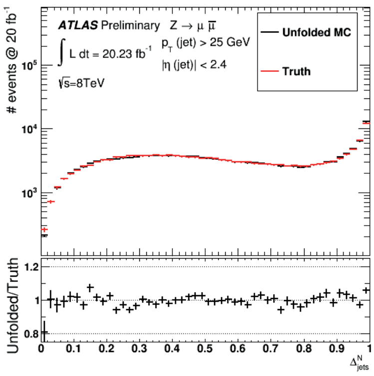

(A) Alpgen $\frac{1}{2}$-$\frac{1}{2}$ closure test

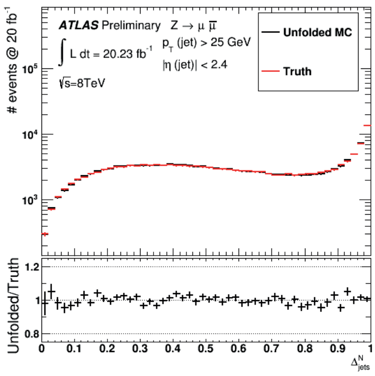

(B) Sherpa $\frac{1}{2}$-$\frac{1}{2}$ closure test

FIGURE 9.5: $\frac{1}{2}$-$\frac{1}{2}$ Closure tests for the unfolding of the normalised jet balance with the Alpgen+Pythia6 sample and for the Sherpa sample. In these test, the closure test is mimicked, but now the response matrix and the input data histogram are statistically independent. These figures show that the unfolding works well, except for low Δ^N_{jj} values.

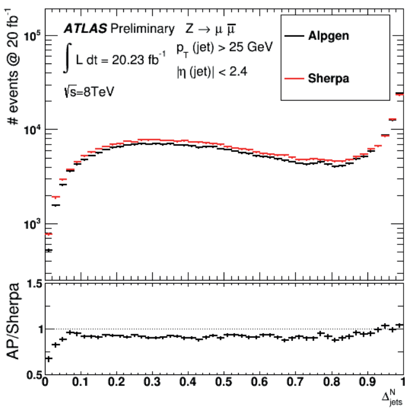

FIGURE 9.6: Comparison of the unfolding between the Alpgen+Pythia6 sample and the Sherpa sample. There are significant differences for the lowest bin (back-to-back jets) and the upper few bins (collinear jets).

- The systematic uncertainties are modelled by variations on the data distribution instead of variations on the two templates in the model.

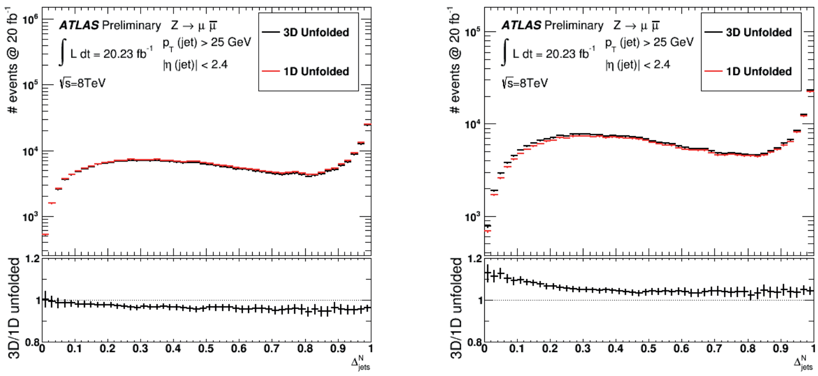

(A) Alpgen 3D unfolded/1D unfolded (B) Sherpa 3D unfolded/1D unfolded

FIGURE 9.7: Comparison between the unfolded data as performed with the 3 dimensional procedure and the unfolded data as performed with the 1-dimensional procedure. The response matrix used for the unfolding was made with the Alpgen+Pythia6 sample for the left plot and with the Sherpa sample in the right plot.

The systematic uncertainties are propagated to the unfolded data by setting up a different response matrix for each variation and unfolding the data for each of these response matrices. A disadvantage is that a profile likelihood method cannot be applied since the test statistic for the configuration where the systematic uncertanties are in the data instead of in the model is currently not implemented in the RooFit package. As a consequence, the total systematic uncertainty can only be calculated by adding all variations quadratically.

The fact that only a simple bin-by-bin unfolding method is used to model the dijet truth signal is a shortcoming of this part of the analysis. However, the full 3-dimensional bayesian unfolding could not be finished in time to be incorporated in the analysis described in this thesis.

For the three different categories that are an input to the calculation of σ_{eff} three different control plots are shown. Figure 9.8 shows a comparison of the Z + 2 jets unfolded data, including all uncertainties, and the truth Alpgen+Herwig+Jimmy MC for the Δ^N_{jj} distribution for both the muon and the electron channels. Figure 9.9 shows a comparison of the Z+0jets unfolded

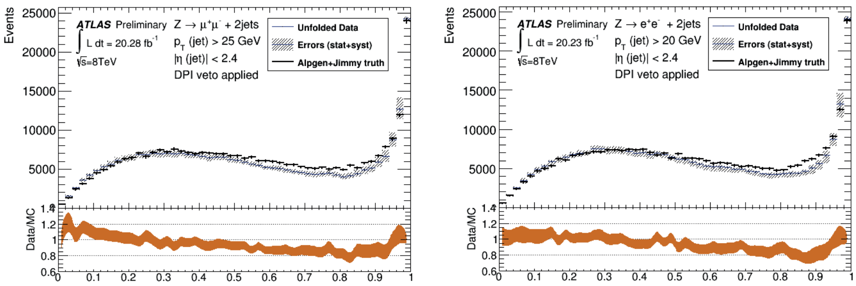

(A) Muon channel prefit data/SPI (B) Electron channel prefit data/SPI

FIGURE 9.8: Comparison of the unfolded data with the truth distribution of the Alpgen+Herwig+Jimmy sample in which the DPI events are vetoed for the normalised jet balance in the Z + 2 jets event selection.

data with the Powheg+Pythia NLO MC sample for the mass spectrum of the Z boson for both the muon and electron channels. Figure 9.10 shows a comparison of the unfolded dijet data and the Powheg+Pythia truth MC for the Δ_{jj}^{N} distribution.

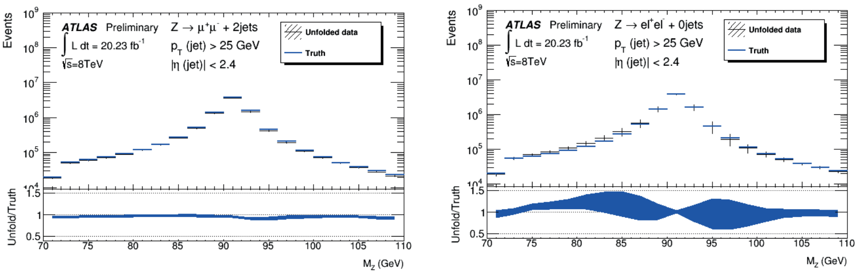

(A) Muon channel (B) Electron channel

FIGURE 9.9: Comparison of the unfolded data with the Powheg+Pythia NLO truth level MC for the mass distribution of the Z boson in the Z+0jet event selection.

From these three distributions, again the f_{DPI} and subsequently σ_{eff} can be extracted. f_{DPI} is determined from fitting a SPI and a DPI template to the unfolded data. In the case of fitting to the unfolded data, the SPI template is the Alpgen+Jimmy truth histogram and the DPI template is taken from the unfolded di-jet data. Since it is not possible to apply a profile-likelihood

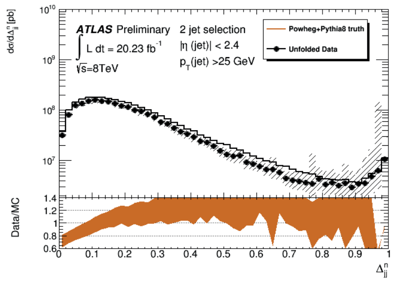

FIGURE 9.10: Comparison of the unfolded data with the Powheg+Pythia NLO truth level MC for the normalised jet balance in the 2jet event selection.

method, the uncertainties of f_{DPI} are determined by applying the fit for each systematic variation of the DPI template and for each variation of the unfolded data. The total uncertainty is then calculated by adding all differences with the nominal value quadratically. The results on f_{DPI} and σ_{eff} are shown below:

$$f_{DPI}(\text{muon channel}) = 4.03^{+1.0}_{-1.1}\% \tag{9.4}$$

$$f_{DPI}(\text{electron channel}) = 2.65^{+1.5}_{-0.70}\%. \tag{9.5}$$

$$\sigma_{eff}(\text{muon channel}) = 16.5^{+5.0}_{-8.1}\ \text{mb} \tag{9.6}$$

$$\sigma_{eff}(\text{electron channel}) = 26.0^{+13}_{-9.5}\ \text{mb}. \tag{9.7}$$

The results for the muon channel are comparable to the results obtained at detector level, while the result in the electron channel deviates even more from the muon channel than was the case at detector level. This provides additional arguments why the result in the muon channel is indeed correct and the electron channel is less reliable.

The uncertainties on f_{DPI} and especially on σ_{eff} are siginificantly larger. This is even the case when comparing them to the uncertainties computed by adding all the uncertainties from the separate nuisance parameters quadratically. The reason for this is the different way of unfolding the data in the Z +

	f_{DPI}	σ_{eff}
JES	18 %	23 %
JER	19 %	31 %
Generator-dependence	8 %	10 %
JVF	3.5 %	6 %
Muon	1 %	2 %
Trigger	0.2 %	$<$ 0.1 %
BCH	$<$ 0.1	$<$ 0.1 %
PRW	$<$ 0.1 %	$<$ 0.1 %
Total systematics	26 %	39 %
MC statistics	6.0	6.0 %
Data statistics	4.0 %	4.0 %
Total	28 %	41 %

TABLE 9.1: Categorised uncertainties on f_{DPI} and σ_{eff}, the errors have been symmetrised as (up+down)/2.

2 jets and the 2jet event categories. In the Z + 2 jets selection, the distributions are unfolded by using a 3-dimensional unfolding in which the migrations across the jet threshold are included in the efficiency calculation. This is not the case for the 2jet event selection. Here simple bin-by-bin correction factors are applied. As a consequence, for many systematic variations the efficiency estimation is shifted upwards in comparison to the nominal for the Z + 2 jets selection. The same variation results in a downward shift for the efficiency estimation in the 2jet selection. Especially for the calculation of σ_{eff} this anticorrelation results in a much larger propagated uncertainty than was the case at detector level. An overview of the systematic breakdown is given in table 9.1.

9.4 Conclusions

This chapter describes how the efficiency and acceptancy of the ATLAS detector are reversed to retrieve the "truth"-histogram. Unfolded distributions obtained by 1-dimensional and 3-dimensional unfolding methods are compared. The 3-dimensional method shows a significant improvement. The unfolded distributions obtained by using the Sherpa and the Alpgen+Pythia generators to fill the response matrix are compared and shown a small difference. The generator dependence is included in the calculation of the total uncertainty.

The result on σ_{eff} in the muon channel is very similar to the result extracted at detector level and is therefore very similar to the result of earlier measurements presented in figure 2.3. However, the result in the electron channel shifted even further away from the result in the muon channel as compared to the extraction at detector level. The large difference in the electron channel between the extracted σ_{eff} at unfolded level and at detector level supports the conclusion that the applied version of the detector simulation cannot be correct. At the same time, the comparable results in the muon channel give confidence that these are solid.

The values of f_{DPI} and especially σ_{eff} have large uncertainties. This is due to a combination of the facts that a profile-likelihood method cannot be applied and that the di-jet data and the Z + 2 jets data are unfolded using different methods. It is fair to conclude that these uncertainties are overestimated and the uncertainties obtained in chapter 8 are derived in a more comprehensive and statistically correct procedure.

Summary
Samenvatting
Acknowledgements
Bibliography

Summary

With the discovery of the Higgs boson [1, 2], the only unmeasured property of the Standard Model is the scalar potential. Even after the discovery of the Higgs, there are still many open question and theories that predict the existence of very rare particles. For the measurement of the scalar potential and the search for future rare beyond the standard model processes, a very detailed understanding of proton-proton collisions is required.

The chance that not one, but two pairs of partons within the same proton-proton collision form a hard interaction increases with the centre-of-mass collision energy of the protons. The phenomenon is referred to as Double Parton Interaction (DPI). In a crude model, the two interactions are considered to be independent and its cross sections can be calculated by factorising the two separate cross section with a certain normalisation factor. This normalisation factor is called the effective cross section (σ_{eff}) and has been studied in eight different analyses [6–10, 75–78]. This analysis adds an independent, clean, measurement.

More sophisticated models incorporate flavour, longitudinal momentum and spin correlations. An overview of these models is presented, but the conclusion is that a measurement of these correlation effects is very difficult with the current dataset.

DPI has not yet been studied in the Z + 2 jets channel until now. While its event topology is very similar to the topology of W+2jet events, it does not depend on the reconstruction of missing energy. Even when the cross section of Z boson production is approximately ten times smaller than that of W boson production, the 2012 dataset holds sufficient statistics. In the muon channel, the event yield is $\approx$ 270,000 events, while the electron channel still holds $\approx$ 200,000 events.

The number of DPI events is estimated by fitting a SPI and a DPI template to the data. The SPI template is taken from a MC Alpgen+Herwig+Jimmy dataset of Z+jets events, from which the DPI events are vetoed. By assuming that the two partonic interactions are independent, a DPI template can be taken from the set of 2jet events in the data. The variable that is used for the fitting is the normalised jet balance $\left(\Delta_{jj}^{N} = \frac{|\vec{p_T}(j1)+\vec{p_T}(j2)|}{|\vec{p_T}(j1)|+|\vec{p_T}(j2)|}\right)$. This variable is found to be very well described by the Alpgen+Herwig+Jimmy sample and is very sensitive to DPI.

The systematic uncertainties on the measured values f_{DPI} and σ_{eff} are estimated by applying a profile-likelihood method. A multi-dimensional likelihood in constructed is created in this method. Each source of systematic uncertainty forms a nuisance parameter in the likelihood and the maximisation of the likelihood gives the estimator on the final result. In this analysis, the total uncertainty is reduced drastically w.r.t. the classical method of adding all systematic uncertainties quadratically. The uncertainties on the nuisance parameters are however overconstrained to less than 10 % of their "prefit" values. It is shown that using the prefit values for the nuisance parameters does not greatly increase the total systematic uncertainty and the largest reduction of the uncertainty is due to the profiling itself.

The fraction of DPI events in the data is measured to be $f_{DPI}(\text{muon channel}) = 4.15^{+.3}_{-.3}\%$ in the muon channel, while in the electron channel a different result is obtained: $f_{DPI}(\text{electron channel}) = 3.04^{+.3}_{-.3}\%$. Event generator programs already include an estimation of DPI in the high transverse momentum region of the underlying event model. These estimations are considered to be too small, in the MC dataset Alpgen+Herwig+Jimmy the fraction of DPI is determined to be $f_{DPI}(MC) = 3.3^{+.15}_{-.15}\%$.

The fraction of DPI events is not expected to be equal in the two channels, although a difference of more than 25 % is surprising. The effective cross section should however be independent of the efficiency and acceptance of the lepton measurements and should therefore be equal in both channels. This is not the case, as in the muon channel the result is $\sigma_{eff}(\text{muon channel}) = 15.6 \pm 1.3 mb$ whereas in the electron channel the result is $\sigma_{eff}(\text{electron channel}) = 19.9 \pm 2$ mb.

It is not possible to directly compare distributions that are measured by different detectors, since they have different efficiencies, acceptances and resolutions. To overcome this, it is necessary to apply a transformation that reverses detector effects. The resulting "unfolded" distribution can be compared directly to the output of event generator programs. Unfolded distributions are especially useful to phenomenologists in comparing their theoretical model with experimental results. The last chapter of this thesis focuses on the unfolding of the measured distributions and repeats the analysis with the unfolded distributions. The "unfolded" effective cross sections are $\sigma_{eff}(\text{muon channel}) = 16.5^{+5.0}_{-8.1}$ and $\sigma_{eff}(\text{electron channel}) = 26.0^{+13}_{-9.5}$. While the result in the muon channel is very similar to the result obtained at detector level, the result in the electron channel shifted even further from the muon value.

A series of cross-checks is performed that point at a problem in the electron channel. The transverse momentum and the mass spectrum of the Z boson are not as well described in the electron channel as they are in the muon channel. The bad agreement between data and MC in the mass spectrum of the Z boson is a by now known issue for the version of the detector simulation that is applied on the Z+jets MC dataset used in this analysis. Unfortunately, there are no relevant ATLAS datasets available yet in which the updated version of the detector simulation is applied.

The result obtained in the muon channel is nonetheless considered as the outcome of this study and is very close to earlier results obtained in the studies mentioned earlier. A shortcoming of this study is that there is only one MC dataset available for the largest background: Z + 2 jets from single parton interactions. This Alpgen+Herwig+Jimmy dataset describes the data very well, but the number of events is low and there are no additional samples available that model the theoretical uncertainties. With a larger MC background dataset, there would be more opportunities to test correlations in the data. By slicing up the dataset and fit the normalised jet balance for each slice, the dependence of the effective cross section on various variables could be tested.

With the measurement of DPI in Z + 2 jets, a new channel is added to the list of DPI measurements. Ultimately, it would be interesting to measure DPI in final states with two electroweak bosons such as same-sign W-pairs, $W^{\pm}Z$ or ZZ final states. This would require at least hundreds of inverse femtobarns at $\sqrt{s} = 13$ TeV, but it is only a matter of time when such a dataset is available.

Samenvatting

Met de ontdekking van het Higgs boson [1, 2] is de laatste onbekende eigenschap van het Standaard Model de scalar potentiaal. Zelfs na de ontdekking van Higgs zijn er nog vele open vragen en theorieën die het bestaan van zeldzame deeltjes voorspellen. Om de scalar potentiaal te meten en voor toekomstige zoektochten naar natuurkundige processen buiten het Standaard Model, is het essentieel om proton-proton botsingen tot in detail te begrijpen.

De kans dat er niet één, maar twee parton paren in dezelfde proton-proton botsingen een energetische interactie aangaan neemt toe met de zwaartepunts energie van de proton botsingen. Dit fenomeen wordt een *Double Parton Interaction genoemd* (DPI), terwijl een normale botsing een *Single Parton Interaction* (SPI) wordt genoemd. De twee interacties kunnen grofweg gemodelleerd worden als onafhankelijk van elkaar en de werkzame doorsnede kan worden berekend door de twee individuele werkzame doorsneden te vermenigvuldigen en te normaliseren. Deze constante wordt de effectieve werkzame doorsnede genoemd (σ_{eff}) en is al in acht eerdere analyses onderzocht [6–10, 75–78]. De analyse beschreven in dit proefschrift voegt een extra onafhankelijke meting toe.

Geavanceerdere DPI modellen gebruiken smaak, impuls en spin correlaties. Deze modellen zijn besproken, maar de conclusie is dat een meting van deze correlaties erg ingewikkeld is met de huidige ATLAS dataset.

DPI was tot nu toe nog niet bestudeerd in het Z + 2 jets kanaal. Terwijl de topologie van de events erg lijkt op die van W+2jet, is er geen missende energie in Z + 2 jets. Zelfs met een tien keer keer kleinere werkzame doorsnede van de Z boson ten opzichte van die van een W boson, bevat de 2012 dataset voldoende statistiek. In het muon kanaal zijn er na het toepassen van alle selectiecriteria nog $\approx$ 270.000 events en in het electron kanaal nog $\approx$ 200.000 events.

Het aantal DPI events wordt geschat door een SPI sjabloon met een DPI sjabloon aan de data te fitten. Het SPI sjabloon wordt geëxtraheerd uit een

Alpgen+Herwig+Jimmy Monte Carlo (MC) dataset, waaruit de DPI events zijn weggefilterd. Door aan te nemen dat de twee parton interacties onafhankelijk zijn kan een DPI sjabloon worden opgesteld uit 2 jet events in de gemeten data. De genormaliseerde jet balans $\left(\Delta_{jj}^{N} = \frac{|\vec{p_T}(j1)+\vec{p_T}(j2)|}{|\vec{p_T}(j1)|+|\vec{p_T}(j2)|}\right)$ wordt gebruikt als fit-variabele. Deze variabele wordt goed beschreven door de MC dataset en is erg onderscheidend voor het DPI signaal.

De systematische onzekerheden op de gemeten waarden van f_{DPI} and σ_{eff} worden geschat door een profile-likelihood methode toe te passen. In deze methode wordt een multi-dimensionale aannemelijkheidsfunctie opgesteld. Elke bron van onzekerheid vormt een storingsparameter in de aannemelijkheidsfunctie en de maximalisering daarvan ten opzichte van elk van die parameters geeft een schatter van het eindresultaat. In deze analyse wordt de totale onzekerheid drastisch gereduceerd ten opzichte van de klassieke manier om onzekerheden af te schatten, namelijk door elke onzekerheid kwadratisch op te tellen. De onzekerheid op de meeste storingsparameters wordt in deze analyse echter tot minder dan tien procent van hun originele waardes ingeperkt, het model is overbepaald. Het is aangetoond dat de reductie op de totale onzekerheid op f_{DPI} and σ_{eff} niet komt doordat het model is overbepaald, maar door het profileren van de aannemelijkheidsfunctie zelf. Dit is gedaan door de oorspronkelijke fouten op de storingsparameters te gebruiken als input in de berekening van de totale onzekerheid op f_{DPI} and σ_{eff}.

De fractie van DPI events in de data is gemeten op $f_{DPI}(\text{muon channel}) = 4.15^{+.3}_{-.3}\%$ in het muon kanaal, terwijl in het electron kanaal een afwijkend resultaat is gemeten: $f_{DPI}(\text{electron channel}) = 3.04^{+.3}_{-.3}\%$. De theoretische computermodellen die gebruikt worden om proton-proton botsingen te simuleren bevatten al een schatting van het aantal DPI events in het hoge impuls gebied van het onderliggende event model. Het wordt breed gedragen dat deze schattingen te laag uitvallen ten opzichte van de werkelijkheid. De gevonden fractie in de MC Alpgen+Herwig+Jimmy dataset is vastgesteld op $f_{DPI}(MC) = 3.3^{+.15}_{-.15}\%$.

Hoewel de fractie van DPI events niet verondersteld wordt gelijk te zijn in de twee kanalen, is een verschil van 25 % erg verrassend. De effectieve werkzame doorsnede zou echter onafhankelijk moeten zijn van de efficiëntie and acceptatie op de lepton metingen en daarom gelijk moeten zijn in beide kanalen. Dit is niet het geval, in het muon kanaal is een waarde σ_{eff}(muon channel) $= 15.6 \pm 1.3$ mb gemeten, terwijl in het electron kanaal de uiteindelijke waarde σ_{eff}(electron channel) $= 19.9 \pm 2$ mb is.

Het is niet mogelijk om distributies afkomstig van verschillende detectoren direct met elkaar te vergelijken, doordat ze beide andere efficiënties, acceptaties en resoluties hebben. Om dit toch te kunnen doen, moet er eerst een statistische techniek worden gebruikt die *unfolden* wordt genoemd. Met deze techniek worden de detector effecten zo goed als mogelijk ongedaan gemaakt en kunnen de verkregen distributies direct vergeleken worden met de voorspellingen van simulaties. Deze techniek is in het bijzonder nuttig voor phenomenologen die hun theoretische modellen willen toetsen aan experimentele data. Het laatste hoofdstuk van dit proefschrift richt zich op het *unfolden* van de gemeten distributies en de effectieve werkzame doorsnede wordt hieruit geëxtraheerd. Het resultaat in het muon kanaal is: σ_{eff}(muon channel) $= 16.5^{+5.0}_{-8.1}$ en in het electron kanaal: σ_{eff}(electron channel) $= 26.0^{+13}_{-9.5}$. Terwijl het resultaat in het muon kanaal erg dicht zit bij het eerder verkregen resulaat op detector-niveau, ligt het resultaat in het electron kanaal zelfs nog verder af van het eerdere resultaat.

Er is nog een aantal andere controles uitgevoerd die erop wijzen dat er een probleem zit in het electron kanaal. De transversale impuls en het massa spectrum van het Z boson komen niet zo precies overeen met de voorspelling als dit het geval is in het muon kanaal. Het feit dat de experimentele data en de voorspelden waarden niet goed overeenkomen voor het massa spectrum van het Z boson is heden een bekend probleem en is veroorzaakt door een onzorgvuldigheid in de detector simulatie. Helaas zijn er geen relevante MC datasets beschikbaar die gesimuleerd zijn met de nieuwste versie van de detector simulatie.

Het resultaat in het muon kanaal wordt beschouwd als de uitkomst van deze studie en komt zeer goed overeen met de uitkomsten van eerdere studies. Een tekortkoming van deze studie is dat er slechts één MC dataset beschikbaar is voor de grootste achtergrond: Z + 2 jets afkomstig van SPI. Deze dataset is produceerd met de combinatie van de Alpgen+Herwig+Jimmy simulatie paketten. De dataset beschijft de experimentele data erg nauwkeurig, maar het bevat slechts een beperkt aantal events en er zijn geen schattingen van de theoretische onzekerheid beschikbaar. Met een grotere dataset zouden er meer mogelijkheden zijn om correlaties tussen de twee partonische interacties te testen. Om correlaties te testen moet de effectieve werkzame doorsnede worden gemeten als functie van een variabele die gevoelig is voor een correlatie. Dit kan bijvoorbeeld de totale transversale impuls van de jets zijn of de azimut hoek tussen het Z boson en de twee jets. Om dit te doen moet de dataset worden opgedeeld in meerdere gebieden van deze gevoelige variabele en voor elk gebied moet de effectieve werkzame doorsnede bepaald worden.

Met deze DPI meting in Z + 2 jets events is er een nieuw proces toegevoegd aan de lijst van DPI metingen. Uiteindelijk zou het fascinerend zijn om DPI te meten in processen waarin twee electrozwakke bosons worden gecreëerd, zoals gelijkgeladen W-paren of Z boson paren. Om zo een soort meting mogelijk te maken zouden op zijn minst honderden inverse femtobarns op $\sqrt{s} = 13$ TeV verzameld moeten worden, maar het is slechts een kwestie van tijd voordat deze statistiek verzameld is.

Acknowledgements

The four/five years in which I have been working on my dissertation have been very interesting, instructive, difficult and not seldom frustrating. Looking back at the process, I can say that it couldn't have been fun if it wasn't a challenge, but two years ago I cursed myself for accepting it. When things get difficult, you learn to trust people who believe in you and eventually you will start to believe in yourself. Someone who was especially important in this process and whom I should thank in the first place is my Promotor Bob van Eijk. Perhaps the best lesson my promotor Bob van Eijk could give me, was to make me believe I could do it myself. Many times I thought of the song "A boy named Sue" as an analogy of his way of supervising, especially the following verse:

And he said: "Son, this world is rough
And if a man's gonna make it, he's gotta be tough
And I knew I wouldn't be there to help ya along.
So I give ya that name and I said goodbye
I knew you'd have to get tough or die
And it's the name that helped to make you strong."

The text of this thesis could never have reached its current quality without Bob's enourmous effort in reviewing it continuously, for which I owe him a tremendous thanks.

In the first part of the programme, I needed to do my service tasks at the Trigger and Data Acquisition groep of ATLAS. Olya Igonkina and Jos Vermeulen were very helpful in this process. I also greatly enjoyed my time at CERN with the Pennsylvania State University group. Doug Schafer, who was still a Ph.D. student himself took the responsibility of guiding me through the software structure of the cost monitoring group.

Halfway my third year, Magdalena Slawinska started to work at Nikhef and started to supervise me on a more regular basis. Even though her native field is theoretical physics instead of experimental physics, and my research was already progressing towards an advanced stadium, she put a lot of effort in trying to understand my research and helped me in every way she could. This way of conscious and conductive supervising is quite special in HEP in my opinion and I am very thankful for it.

The last supervisor to whom I am very much indebted is Ulrike Blumenschein. We happened to have the same interest for Double Parton Interactions and she gracefully accepted to take Miroslav Myska and myself in her Z + jets analysis group and help us with this research. Ulrike's sharp insights, knowledge of the ATLAS detector and Z+jets physics were unmissable in writing this thesis. I have also been very lucky to have met Miroslav Myska. It was a great relieve to discover that there was someone else in ATLAS who was trying to do the same research and was willing to take up this struggle together. I thank him for our discussions on DPI, ATLAS and many other topics. It has been a pleasure to work with Rodger Mantifel and cooperate with him on solving all kinds of common topics.

My first analysis project in ATLAS started with the group that studies same sign W-pair production in vector boson scattering processes. At first I was quite overwhelmed by the complexity of such an analysis. Especially Simone Pagan Griso was very supportive in that period and helped me by explaining many difficult topics and pointing me at the right direction for the continuation of my research.

Many people at Nikhef have been very supportive over the last four years. Tomas Kasemets with his efforts to bring theorists and experimentalists together and explaining various theoretical topics in the field of DPI. Wouter Verkerke was a great help in understanding the statistical aspects of my analysis and I thank Ronald Starink for being patient with my mistakes on the Stoomboot cluster.

There are two persons at Nikhef who I didn't mention yet, but were especially important during the last few years. Lars Beemster and Hartger Weits felt like 'partners in crime'. Perhaps all three of us did not completely fit in

the world of physics, but therefore enjoyed our time at Nikhef even more. I am curious how we will think about our "zero-sum game" philosophy in thirty years.

Last, but by far not the least, I would like to thank all my family and friends. I often felt quite selfish when I needed to cancel appointments, or perhaps even worse: when I could only think of my research while spending time with you. Especially my wife has been very supportive. An important moment for me was that she told me she thought I would finish my Ph.D. successfully. Even though she does not know much about physics, it somehow gave me a lot of confidence. All my sisters and my brother are equally important to me, as are my parents. My family consists of the funniest, most insightful and sweetest people I know. I am grateful to my in laws for untiringly taking an interest in my exotic field of research and being very supportive in the most difficult periods.

I am blessed with so many friends who have supported me and were patient enough to endure my whining. I couldn't even thank them all individually for their support over the last years. Nonetheless I would like to name a few VIPs. The many evening of playing Age of Mythology with Rob and Willem were an awesome reminder that one shouldn't grow up too swiftly. I am especially grateful to Rob for reviewing my thesis and spotting some important issues on the break of printing the manuscript. Willem and Albert have always been keeping me on the right moral (philosophical) path, and I hope they will continue doing this. I could never have endured academical life without once in a while drinking beers with Frank, while watching matches of FC Twente and Champion's league. Finally, I would like to name Corniël and Mirjam, who are simply special for me and my wife.

So long, so long, and thanks for all the fish!

Bibliography

[1] S. Chatrchyan et al. Observation of a new boson at a mass of 125 GeV with the CMS experiment at the LHC. *Physics Letters B*, 716(1):30 – 61, 2012.

[2] G. Aad et al. Observation of a new particle in the search for the standard model higgs boson with the atlas detector at the lhc. *Physics Letters B*, 716(1):1 – 29, 2012.

[3] G. Aad et al. Combined Measurement of the Higgs Boson Mass in pp Collisions at $\sqrt{s} = 7$ and 8 TeV with the ATLAS and CMS Experiments. *Phys. Rev. Lett.*, 114:191803, May 2015.

[4] M. Slawinska, W. van den Wollenberg, B. van Eijk, and S. Bentvelsen. Phenomenology of the trilinear Higgs coupling at proton-proton colliders. *ArXiv:1408.5010*, August 2014.

[5] J. Baglio, A. Djouadi, R. Gröber, M.M. Mühlleitner, J. Quevillon, et al. The measurement of the Higgs self-coupling at the LHC: theoretical status. *Journal of High Energy Physics*, 1304:151, 2013.

[6] T. Akesson et al. Double Parton Scattering in pp Collisions at $\sqrt{s} = 63$-GeV. *Z.Phys.*, C34:163, 1987.

[7] J. Alitti et al. A Study of multi-jet events at the CERN anti-p p collider and a search for double parton scattering. *Phys.Lett.*, B268:145–154, 1991.

[8] F. Abe et al. Study of four jet events and evidence for double parton interactions in $p\bar{p}$ collisions at $\sqrt{s} = 1.8$ TeV. *Phys.Rev.*, D47:4857–4871, 1993.

[9] CMS collaboration. Study of double parton scattering using W + 2-jet events in proton-proton collisions at $\sqrt{s} = 7$ TeV. *Journal of High Energy Physics*, 2014(3), 2014.

[10] ATLAS collaboration. Measurement of hard double-parton interactions in W ($\rightarrow l\nu$) + 2-jet events at $\sqrt{s} = 7$ TeV with the ATLAS detector. *New Journal of Physics*, 15(3):033038, 2013.

[11] M. Planck. Über das Gesetz der Energieverteilung im Normalspectrum. *Annalen der Physik*, 309:553–563, 1901.

[12] A. Einstein. Über einen die Erzeugung und Verwandlung des Lichtes betreffenden heuristischen Gesichtspunkt. *Annalen der Physik*, 322:132–148, 1905.

[13] A. Einstein. Über die von der molekularkinetischen Theorie der Wärme geforderte Bewegung von in ruhenden Flüssigkeiten suspendierten Teilchen. *Annalen der Physik*, 322:549–560, 1905.

[14] A. Einstein. Zur Elektrodynamik bewegter Körper. *Annalen der Physik*, 322:891–921, 1905.

[15] A. Einstein. Ist die Trägheit eines Körpers von seinem Energieinhalt abhängig? *Annalen der Physik*, 323:639–641, 1905.

[16] A. Einstein. Die Grundlage der allgemeinen Relativitätstheorie. *Annalen der Physik*, 354:769,822, 1916.

[17] L. De Broglie. Recherches sur la théorie des quanta. *Annales de Physique*, 3:22,128, 1925.

[18] S.H. Neddermeyer and C. D. Anderson. Note on the nature of cosmic-ray particles. *Phys. Rev.*, 51:884–886, May 1937.

[19] C. D. Anderson and S. H. Neddermeyer. Cloud chamber observations of cosmic rays at 4300 meters elevation and near sea-level. *Phys. Rev.*, 50:263–271, Aug 1936.

[20] C.M.G. Lattes, H. Muirhead, G.P.S. Occhialini, and C.F. Powell. Processes Involving Charged Mesons. *Nature*, 159:694–697, 1947.

[21] M. Gell-Mann. The Eightfold Way: A Theory of strong interaction symmetry. 1961.

[22] S. Weinberg. A Model of Leptons. *Physical Review Letters*, 19:1264–1266, November 1967.

[23] S.L. Glashow. Partial Symmetries of Weak Interactions. *Nucl.Phys.*, 22:579–588, 1961.

[24] A. Salam and J. C. Ward. Electromagnetic and weak interactions. *Phys. Lett.*, 13:168–171, 1964.

[25] W. Pauli. Über den Zusammenhang des Abschlusses der Elektronengruppen im Atom mit der Komplexstruktur der Spektren. (German) [On the relation of the completion of groups of electrons in the atom with the complex structure of spectra]. *j-Z-PHYSIK*, 31(1):765–783, February 1925.

[26] E. Noether. Invariante variationsprobleme. *Nachrichten von der Gesellschaft der Wissenschaften zu Göttingen, Mathematisch-Physikalische Klasse*, 1918:235–257, 1918.

[27] A. Tresse. Sur les invariants différentiels des groupes continus de transformations. *Acta Mathematica*, 18(1):1–88, 1894.

[28] C. N. Yang and R. L. Mills. Conservation of Isotopic Spin and Isotopic Gauge Invariance. *Physical Review*, 96:191–195, October 1954.

[29] W.R. Hamilton. On a general method in dynamics. *Philosophical Transaction of the Royal Society*, 2:247–308, 1834.

[30] P. A. M. Dirac. A Theory of Electrons and Protons. *Royal Society of London Proceedings Series A*, 126:360–365, January 1930.

[31] C. S. Wu, E. Ambler, R. W. Hayward, D. D. Hoppes, and R. P. Hudson. Experimental Test of Parity Conservation in Beta Decay. *Physical Review*, 105:1413–1415, February 1957.

[32] J. Beringer et al. Review of Particle Physics (RPP). *Phys.Rev.*, D86:010001, 2012.

[33] J. Goldstone, A. Salam, and S. Weinberg. Broken symmetries. *Phys. Rev.*, 127:965–970, Aug 1962.

[34] J. Schwinger. On the Green's Functions of Quantized Fields. I. *Proceedings of the National Academy of Science*, 37:452–455, July 1951.

[35] F. J. Dyson. The S Matrix in Quantum Electrodynamics. *Physical Review*, 75:1736–1755, June 1949.

[36] R. P. Feynman. Space-time approach to non-relativistic quantum mechanics. *Rev. Mod. Phys.*, 20:367–387, Apr 1948.

[37] Planck Collaboration, P.A.R. Ade, et al. Planck 2013 results. I. Overview of products and scientific results. *Astronomy and Astrophysics*, 571:A1, November 2014.

[38] V.C. Rubin and Jr. Ford, W. Kent. Rotation of the Andromeda Nebula from a Spectroscopic Survey of Emission Regions. *Astrophys.J.*, 159:379–403, 1970.

[39] A. Harvey. How Einstein Discovered Dark Energy. *ArXiv e-prints*, November 2012.

[40] S. Perlmutter, G. Aldering, G. Goldhaber, R. A. Knop, P. Nugent, P. G. Castro, S. Deustua, S. Fabbro, A. Goobar, D. E. Groom, I. M. Hook, A. G. Kim, M. Y. Kim, J. C. Lee, N. J. Nunes, R. Pain, C. R. Pennypacker, R. Quimby, C. Lidman, R. S. Ellis, M. Irwin, R. G. McMahon,

P. Ruiz-Lapuente, N. Walton, B. Schaefer, B. J. Boyle, A. V. Filippenko, T. Matheson, A. S. Fruchter, N. Panagia, H. J. M. Newberg, W. J. Couch, and T. S. C. Project. Measurements of Ω and Λ from 42 High-Redshift Supernovae. *Astrophysical Journal*, 517:565–586, June 1999.

[41] A.G. Riess, A.V. Filippenko, P. Challis, A. Clocchiatti, A. Diercks, P.M. Garnavich, R.L. Gilliland, C.J. Hogan, S. Jha, R.P. Kirshner, B. Leibundgut, M.M. Phillips, D. Reiss, B.P. Schmidt, R.A. Schommer, R.C. Smith, J. Spyromilio, C. Stubbs, N.B. Suntzeff, and J. Tonry. Observational Evidence from Supernovae for an Accelerating Universe and a Cosmological Constant. *Astronomical Journal*, 116:1009–1038, September 1998.

[42] H. Miyazawa. Baryon Number Changing Currents. *Progress of Theoretical Physics*, 36:1266–1276, December 1966.

[43] H. Miyazawa. Spinor Currents and Symmetries of Baryons and Mesons. *Physical Review*, 170:1586–1590, June 1968.

[44] J.-L. Gervais and B. Sakita. Field theory interpretation of supergauges in dual models. *Nuclear Physics B*, 34:632–639, November 1971.

[45] P. Ramond. Dual Theory for Free Fermions. *Physical Review D*, 3:2415–2418, May 1971.

[46] L. Randall and R. Sundrum. Large Mass Hierarchy from a Small Extra Dimension. *Physical Review Letters*, 83:3370–3373, October 1999.

[47] E. D. Bloom, D. H. Coward, H. DeStaebler, J. Drees, G. Miller, L. W. Mo, R. E. Taylor, M. Breidenbach, J. I. Friedman, G. C. Hartmann, and H. W. Kendall. High-energy inelastic ep scattering at $6°$ and $10°$. *Phys. Rev. Lett.*, 23:930–934, Oct 1969.

[48] H. Abramowicz et al. Combination of measurements of inclusive deep inelastic $e^{\pm}p$ scattering cross sections and QCD analysis of HERA data. *Eur. Phys. J.*, C75(12):580, 2015.

[49] J. D. Bjorken and E. A. Paschos. Inelastic electron-proton and γ-proton scattering and the structure of the nucleon. *Phys. Rev.*, 185:1975–1982, Sep 1969.

[50] V.N. Gribov and L.N. Lipatov. Deep inelastic e p scattering in perturbation theory. *Sov.J.Nucl.Phys.*, 15:438–450, 1972.

[51] Y. L. Dokshitzer. Calculation of the Structure Functions for Deep Inelastic Scattering and e+ e- Annihilation by Perturbation Theory in Quantum Chromodynamics. *Sov.Phys.JETP*, 46:641–653, 1977.

[52] G. Altarelli and G. Parisi. Asymptotic Freedom in Parton Language. *Nucl.Phys.*, B126:298, 1977.

[53] D. J. Gross and F. Wilczek. Asymptotically Free Gauge Theories. I. *Physical Review D*, 8:3633–3652, nov 1973.

[54] H. D. Politzer. Reliable Perturbative Results for Strong Interactions? *Physical Review Letters*, 30:1346–1349, jun 1973.

[55] W. Verkerke. *Measurement of Charm Production in Deep Inelastic Scattering*. PhD thesis, Amsterdam University, 1998.

[56] C. Adloff et al. Deep-inelastic inclusive ep scattering at low x and a determination of α_s. *The European Physical Journal C - Particles and Fields*, 21(1):33–61, 2001.

[57] H. Abramowicz et al. Measurement and QCD analysis of neutral and charged current cross sections at HERA. *The European Physical Journal C - Particles and Fields*, 30(1):1–32, 2003.

[58] S. Chekanov et al. Zeus next-to-leading-order qcd analysis of data on deep inelastic scattering. *Phys. Rev. D*, 67:012007, Jan 2003.

[59] Benvenuti, A.C. and others. A High Statistics Measurement of the Proton Structure Functions F(2) (x, Q^2) and R from Deep Inelastic Muon Scattering at High Q^2. *Phys.Lett.*, B223:485, 1989.

[60] M. Arneodo et al. Measurement of the proton and deuteron structure functions, F2(p) and F2(d), and of the ratio sigma-L / sigma-T. *Nucl.Phys.*, B483:3–43, 1997.

[61] S. Glazov. Measurement of DIS cross section at HERA. *Brazilian Journal of Physics*, 37:793 – 797, 06 2007.

[62] A.D. Martin, W.J. Stirling, R.S. Thorne, and G. Watt. Parton distributions for the LHC. *The European Physical Journal C*, 63(2):189–285, 2009.

[63] H. Bruns. Das eikonal. *Abhandlungen der Mathematisch-Physischen Classe der Königlich Söchsischen Gesellschaft der Wissenschaften*, 11:323–436, 1895.

[64] G. Antchev et al. Luminosity-Independent Measurement of the Proton-Proton Total Cross Section at $\sqrt{s} = 8$ TeV. *Phys. Rev. Lett.*, 111:012001, Jul 2013.

[65] Sjöstrand, T. and Skands, P.Z. Multiple interactions and the structure of beam remnants. *Journal of High Energy Physics*, 2004(03):053, 2004.

[66] T. Sjöstrand and M. van Zijl. A Multiple Interaction Model for the Event Structure in Hadron Collisions. *Phys.Rev.*, D36:2019, 1987.

[67] E.M. Levin L.V. Gribov and M.G. Ryskin. Semihard processes in qcd. *Phys. Rept.*, 100:1, 1983.

[68] R. Corke and T. Sjostrand. Multiparton Interactions with an x-dependent Proton Size. *Journal of High Energy Physics*, 1105:009, 2011.

[69] B. Blok, Yu. Dokshitzer, L. Frankfurt, and M. Strikman. The Four jet production at LHC and Tevatron in QCD. *Phys.Rev.*, D83:071501, 2011.

[70] J.R. Gaunt and W. J. S. Double parton distributions incorporating perturbative qcd evolution and momentum and quark number sum rules. *Journal of High Energy Physics*, 2010(3):1–40, 2010.

[71] G. Calucci and D. Treleani. Double parton scatterings in high energy hadronic collisions. *Nuclear Physics B - Proceedings Supplements*, 71(1–3):392 – 399, 1999. Multiparticle dynamics 1997.

[72] M. Bahr, S. Gieseke, M.A. Gigg, D. Grellscheid, K. Hamilton, et al. Herwig++ Physics and Manual. *Eur.Phys.J.*, C58:639–707, 2008.

[73] G. Calucci and D. Treleani. Minijets and the two-body parton correlation. *Phys. Rev. D*, 57:503–511, Jan 1998.

[74] L. Frankfurt, M. Strikman, and C. Weiss. Dijet production as a centrality trigger for pp collisions at CERN LHC. *Phys.Rev.*, D69:114010, 2004.

[75] F. Abe et al. Double parton scattering in $p\bar{p}$ collisions at $\sqrt{s} = 1.8$ TeV. *Phys. Rev. D*, 56:3811–3832, Oct 1997.

[76] V. M. Abazov et al. Azimuthal decorrelations and multiple parton interactions in $\gamma + 2$ jet and $\gamma + 3$ jet events in $p\bar{p}$ collisions at $\sqrt{s} = 1.96$ TeV. *Phys. Rev. D*, 83:052008, Mar 2011.

[77] V. M. Abazov et al. Double parton interactions in $\gamma + 3$ jet events in $p\bar{p}$ collisions at $\sqrt{s} = 1.96$ TeV. *Phys. Rev. D*, 81:052012, Mar 2010.

[78] V. M. Abazov et al. Double parton interactions n $\gamma + 3$ jet events in $p\overline{p}$ collisions at $\sqrt{s} = 1.96$ TeV. *Phys. Rev. D*, 81:052012, Mar 2010.

[79] R. Aaij et al. Observation of double charm production involving open charm in pp collisions at $\sqrt{s} = 7$ TeV. *Journal of High Energy Physics*, 1206:141, 2012.

[80] A. Del Fabbro and D. Treleani. Scale factor in double parton collisions and parton densities in transverse space. *Phys. Rev. D*, 63:057901, Jan 2001.

[81] A.M. Snigirev. Double parton distributions in the leading logarithm approximation of perturbative QCD. *Phys.Rev.*, D68:114012, 2003.

[82] V.P. Shelest, A.M. Snigirev, and G.M. Zinovjev. Gazing into the multiparton distribution equations in qcd. *Physics Letters B*, 113(4):325 – 328, 1982.

[83] R. Kirschner. Generalized Lipatov-Altarelli-Parisi Equations and Jet Calculus Rules. *Phys.Lett.*, B84:266, 1979.

[84] J. R. Gaunt, C. Kom, A. Kulesza, and W. J. Stirling. Same-sign W pair production as a probe of double parton scattering at the LHC. *Eur.Phys.J.*, C69:53–65, 2010.

[85] E. Maina. Multiple Parton Interactions in Z+jets production at the LHC. A comparison of factorized and non-factorized double parton distribution functions. *Journal of High Energy Physics*, 1101:061, 2011.

[86] Diehl, M. and Schäfer,M. Theoretical considerations on multiparton interactions in qcd. *Physics Letters B*, 698(5):389 – 402, 2011.

[87] J.R. Gaunt and W.J. Stirling. Double parton scattering singularity in one-loop integrals. *Journal of High Energy Physics*, 2011(6):1–29, 2011.

[88] M. Mekhfi. Correlations in color and spin in multiparton processes. *Phys. Rev. D*, 32:2380–2384, Nov 1985.

[89] Diehl, M. and Ostermeier, D. and Schäfer, A. Elements of a theory for multiparton interactions in QCD. *Journal of High Energy Physics*, 1203:089, 2012.

[90] M. Diehl and T. Kasemets. Positivity bounds on double parton distributions. *Journal of High Energy Physics*, 1305:150, 2013.

[91] J. Soffer. Positivity constraints for spin-dependent parton distributions. *Phys. Rev. Lett.*, 74:1292–1294, Feb 1995.

[92] T. Kasemets and M. Diehl. Angular correlations in the double Drell-Yan process. *Journal of High Energy Physics*, 1301:121, 2013.

[93] H. Chang, A.V. Manohar, and W. J. Waalewijn. Double Parton Correlations in the Bag Model. *Phys.Rev.*, D87(3):034009, 2013.

[94] A. van Hameren, R. Maciula, and A. Szczurek. Single-parton scattering versus double-parton scattering in the production of two $c\bar{c}$ pairs and charmed meson correlations at the LHC. *Phys. Rev.*, D89(9):094019, 2014.

[95] M. G. Echevarria, T. Kasemets, P. J. Mulders, and Cristian P. Polarization effects in double open-charm production at LHCb. *Journal of High Energy Physics*, 04:034, 2015.

[96] S. Frixione and B.R. Webber. Matching nlo qcd computations and parton shower simulations. *Journal of High Energy Physics*, 2002(06):029, 2002.

[97] Paolo Nason. A new method for combining nlo qcd with shower monte carlo algorithms. *Journal of High Energy Physics*, 2004(11):040, 2004.

[98] M.L. Mangano, M. Moretti, F. Piccinini, and M. Treccani. Matching matrix elements and shower evolution for top-quark production in hadronic collisions. *Journal of High Energy Physics*, 0701:013, 2007.

[99] M. L. Mangano, M. Moretti, and R. Pittau. Multijet matrix elements and shower evolution in hadronic collisions: $Wb\bar{b} + n$ jets as a case study. *Nucl.Phys.*, B632:343–362, 2002.

[100] S. Catani, F. Krauss, R. Kuhn, and B.R. Webber. QCD matrix elements + parton showers. *Journal of High Energy Physics*, 0111:063, 2001.

[101] F. Krauss. Matrix elements and parton showers in hadronic interactions. *Journal of High Energy Physics*, 0208:015, 2002.

[102] C.W. Bauer, F.J. Tackmann, and J. Thaler. Geneva (i): a new framework for event generation. *Journal of High Energy Physics*, 2008(12):010, 2008.

[103] K. Hamilton and P. Nason. Improving NLO-parton shower matched simulations with higher order matrix elements. *Journal of High Energy Physics*, 1006:039, 2010.

[104] S. Hoeche, F. Krauss, M. Schonherr, and F. Siegert. QCD matrix elements + parton showers: The NLO case. *Journal of High Energy Physics*, 1304:027, 2013.

[105] S. Höche. Merging matrix elements with parton showers, 2012.

[106] L.M. Mangano, F. Piccinini, A.D. Polosa, M. Moretti, and R. Pittau. Alpgen, a generator for hard multiparton processes in hadronic collisions. *Journal of High Energy Physics*, 2003(07):001, 2003.

[107] A. Belyaev, N. D. Christensen, and A. Pukhov. CalcHEP 3.4 for collider physics within and beyond the Standard Model. *Comput.Phys.Commun.*, 184:1729–1769, 2013.

[108] J. Alwall, M. Herquet, F. Maltoni, O. Mattelaer, and T. Stelzer. MadGraph 5 : Going Beyond. *Journal of High Energy Physics*, 1106:128, 2011.

[109] T. Sjöstrand et al. Pythia 6.4 physics and manual. *Journal of High Energy Physics*, 2006.

[110] A. Aktas et al. Elastic J/psi production at HERA. *Eur.Phys.J.*, C46:585–603, 2006.

[111] S. Chekanov et al. Exclusive photoproduction of J / psi mesons at HERA. *Eur.Phys.J.*, C24:345–360, 2002.

[112] G. Aad et al. The ATLAS Experiment at the CERN Large Hadron Collider. *JINST*, 3:S08003, 2008.

[113] A. Augusto Alves et al. The LHCb Detector at the LHC. *JINST*, 3:S08005, 2008.

[114] K. Aamodt et al. The alice experiment at the cern lhc. *JINST*, 0803:S08002, 2008.

[115] Dowler. B. et al. Performance of the atlas hadronic end-cap calorimeter in beam tests. *Nuclear Instruments and Methods in Physics Research*

Section A: Accelerators, Spectrometers, Detectors and Associated Equipment, 482(1–2):94 – 124, 2002.

[116] G. Aad et al. Jet energy resolution in proton-proton collisions at $\sqrt{s} = 7$ TeV recorded in 2010 with the ATLAS detector. *The European Physical Journal C*, 73(3):1–27, 2013.

[117] G. Aad et al. Measurement of the inclusive jet cross section in pp collisions at sqrt(s)=2.76 TeV and comparison to the inclusive jet cross section at sqrt(s)=7 TeV using the ATLAS detector. *Eur. Phys. J.*, C73(8):2509, 2013.

[118] Atlas e-news, 28 june 2010. `http://atlas-service-enews.web.cern.ch/atlas-service-enews/2010/news_10/news_ReadyRejection.php`. Accessed: 2015-07-01.

[119] R. Ospanov. Resource utilization by the atlas high level trigger during 2010 and 2011 lhc running. *Physics Procedia*, 37(0):1900 – 1907, 2012. Proceedings of the 2nd International Conference on Technology and Instrumentation in Particle Physics (TIPP 2011).

[120] G. Aad et al. Electron reconstruction and identification efficiency measurements with the atlas detector using the 2011 lhc proton–proton collision data. *The European Physical Journal C*, 74(7), 2014.

[121] N. Eldik A. Poppleton, P. Kluit. Performance of the new muon chain improving decay in flight rejection, 2012.

[122] M. Cacciari, G. P. Salam, and G. Soyez. The Anti-k(t) jet clustering algorithm. *Journal of High Energy Physics*, 0804:063, 2008.

[123] M. Cacciari, G. P. Salam, and G. Soyez. The Catchment Area of Jets. *Journal of High Energy Physics*, 0804:005, 2008.

[124] G. Aad et al. Jet energy measurement and its systematic uncertainty in proton-proton collisions at $\sqrt{s} = 7$ TeV with the ATLAS detector. 2014.

[125] M. Limper. *Track and vertex reconstruction in the ATLAS inner detector*. PhD thesis, Universiteit van Amsterdam, 10 1999.

[126] K. Grimm, E. Guido, F. Meloni, S. Pagan Griso, K. Prokofiev, M. Rudolph, and A. Wildauer. Methods to quantify the performance of the primary vertex reconstruction in the atlas experiment under high luminosity conditions. *Journal of Physics: Conference Series*, 396(2):022041, 2012.

[127] A. Airapetian et al. ATLAS: Detector and physics performance technical design report. Volume 1. 1999.

[128] G. Aad et al. Jet energy resolution in proton-proton collisions at $\sqrt{\mathrm{s}} = 7$ TeV recorded in 2010 with the ATLAS detector. *The European Physical Journal C*, 73(3), 2013.

[129] G. Aad et al. Pile-up subtraction and suppression for jets in ATLAS. Technical Report ATLAS-CONF-2013-083, CERN, Geneva, 2013.

[130] G. Aad et al. Performance of the ATLAS Electron and Photon Trigger in p-p Collisions at $\sqrt{s} = 7$ TeV in 2011. Technical Report ATLAS-CONF-2012-048, CERN, Geneva, May 2012.

[131] G. Aad et al. Performance of the ATLAS muon trigger in 2011. Technical Report ATLAS-CONF-2012-099, CERN, Geneva, Jul 2012.

[132] R. Barlow and C. Beeston. Fitting using finite monte carlo samples. *Computer Physics Communications*, 77(2):219 – 228, 1993.

[133] J. Neyman and E. S. Pearson. On the problem of the most efficient tests of statistical hypotheses. *Philosophical Transactions of the Royal Society of London A: Mathematical, Physical and Engineering Sciences*, 231(694-706):289–337, 1933.

[134] S. S. Wilks. The large-sample distribution of the likelihood ratio for testing composite hypotheses. *Ann. Math. Statist.*, 9(1):60–62, 03 1938.

[135] W. Verkerke and D. P. Kirkby. The RooFit toolkit for data modeling. *eConf*, C0303241:MOLT007, 2003.

[136] G. Cowan. *Statistical Data Analysis*. Oxford University Press, Oxford, 1998.

[137] V. Blobel. Data unfolding, 2010.

[138] T. Bayes. An essay towards solving a problem in the doctrine of chances. *Philosophical Transactions of the Royal Society*, 35:370–418, 1763.